This is to certify that the
dissertation entitled

IMPACT OF THE INTERACTION BETWEEN STRUCTURAL, ENVIRONMENTAL, AND LOADING FACTORS ON RIGID PAVEMENT RESPONSES

presented by

KAENVIT VONGCHUSIRI

has been accepted towards fulfillment
of the requirements for the

Ph.D. degree in Civil Engineering

Major Professor's Signature

8/9/05

Date

IMPACT OF THE INTERACTION BETWEEN STRUCTURAL, ENVIRONMENTAL, AND LOADING FACTORS ON RIGID PAVEMENT RESPONSES

By

Kaenvit Vongchusiri

A DISSERTATION

Submitted to
Michigan State University
in partial fulfillment of the requirements
for the degree of

DOCTORAL OF PHILOSOPHY

Department of Civil and Environmental Engineering

2005

ABSTRACT

IMPACT OF THE INTERACTION BETWEEN STRUCTURAL, ENVIRONMENTAL, AND LOADING FACTORS ON RIGID PAVEMENT RESPONSES

By

Kaenvit Vongchusiri

This dissertation focused on the impact of the interaction between structural, environmental, and loading factors on mechanistic responses of rigid pavements. Computed through the mechanistic analysis approach, the pavement responses could be linked to rigid pavement performance. Therefore, this study established the understanding of the impact of the interaction between such factors on mechanistic responses, captured through an extensive parametric study. Without sacrificing the quality of the final results, this study employed several strategies to reduce the size of the experimental matrix to a practical number of 43,092 finite element runs.

Based on the parametric study results, the insight into the impact of the interaction between various parameters on pavement stresses was established. Understanding the mechanistic behavior of the pavement provides an indirect connection to a better comprehension of pavement performance. The increase in base/subbase thickness resulted in a reduction in stress magnitude with diminishing effect as the slab thickness increases. While lateral support condition had a significant effect on loading stress magnitude, its effect on thermal stress magnitude appeared to be insignificant as shown in the figure. An increase in the magnitude of modulus of subgrade reaction resulted in a reduction in stress magnitude with diminishing effect as the slab thickness increased. An increase in the magnitude of modulus of subgrade reaction resulted in an increase in the

magnitude of thermal stress as the combined stress magnitudes were compared to the loading stress magnitudes. When combined with thermal stress, an interactive effect between thermal strain gradient and joint spacing on combined loading and thermal stress was observed. The results suggested that a more complex axle group should result in a lower pavement stress magnitude. However, the results did not account for the interaction between axle spacing and joint spacing.

This study also included a development of interpolation schemes to predict stresses in jointed concrete pavements subjected to traffic and environmental loads. The interpolation schemes were developed based on the various design scenarios that reflect the current design practice. The interpolation schemes were found to be highly efficient in generating stresses for an unlimited number of scenarios, based on a limited number of finite element runs. Validation of the interpolation schemes was conducted by comparing the interpolated stresses to finite element analysis results.

Also, this study demonstrated that influence surfaces for rigid pavements could be successfully developed via a numerical procedure based on a series of finite element analyses and a multi-dimensional interpolation process. The extensive verification process used herein suggested that influence surfaces could precisely and accurately quantify pavement stresses under various loading conditions. Versatility of the influence surface technique for rigid pavements includes, but is not limited to, rapid pavement stress calculation, determination of critical load location, pavement stress history, and investigation of the interaction between load configuration and structural feature. The use of this technique is clearly more effective and practical than the direct application of the finite element method.

ACKNOWLEDGEMENTS

I would like to express my most sincere gratitude to Dr. Neeraj Buch, the chairman of my dissertation committee, whom I am profoundly indebted to, for his encouragement and his support both technically and personally throughout the course of my graduate studies. He also served as a role model without whose guidance it would not have been possible to complete this research. My sincere appreciation also goes to the committee members, Dr. Gilbert Baladi, Dr. Karim Chatti, and Dr. Dennis Gilliland, for their perseverance and assistance.

The financial supports of the Royal Thai Government, the Department of Civil and Environmental Engineering at Michigan State University, and the Michigan Department of Transportation throughout my studies are greatly appreciated.

Special thanks are extended to Mr. Michael Sherry of the Writing Center for his expertise in peer reviewing, to Dr. Rigoberto Burgueño for his guidance on the influence surface theorem, and also to my fellow colleagues, including Mr. Praveen Desaraju, Mr. Hassan Salama, and Dr. Syed Waqar Haider for supporting this research and for truly sharing their experience with me.

Finally, I would also like to thank my mother Lalida for always providing guidance throughout my life and my girlfriend Sonali for being there and persevering while I pursued this undertaking.

TABLE OF CONTENTS

LIST OF TABLES vii

LIST OF FIGURES viii

CHAPTER I
INTRODUCTION 1
1.1 Background 1
1.2 Problem identification 2
1.3 Research objectives 3
1.4 Chapter overview 4

CHAPTER II
LITERATURE REVIEW 7
2.1 Finite element analysis of rigid pavements 7
2.2 Factors affecting mechanistic responses 14
2.3 Application of influence surfaces 25

CHAPTER III
PARAMETRIC STUDY 28
3.1 Data collection 28
3.2 Experimental matrix 30
3.3 Analysis process 47
3.4 Documentation of analysis results 58

CHAPTER IV
INTERPOLATION SCHEME 88
4.1 Least-squares criteria 88
4.2 Development of interpolation schemes 90
4.3 Validation of interpolation schemes 96
4.4 Sample of calculation 111

CHAPTER V
INFLUENCE SURFACE TECHNIQUE 115
5.1 Construction of influence surfaces 116
5.2 Interpretation of influence surfaces 129
5.3 Verification of the proposed technique 131
5.4 Potential applications 136

CHAPTER VI
CONCLUSIONS, RESEARCH SIGNIFICANCE AND RECOMMENDATIONS ... 160
6.1 Conclusions 160
6.2 Research significance 165

6.3 Recommendations for future research 168

BIBLIOGRAPHY 170

LIST OF TABLES

Table 1: Summary of design parameters from the 14 MDOT designs 29

Table 2: Ranges of input parameters obtained from other sources 29

Table 3: Final experimental matrix 47

Table 4: Validation matrix 53

Table 5: Summary of critical load locations 57

Table 6: Summary of interaction between parameters on stresses 83

Table 7: Example prediction matrices 95

Table 8: Summary of goodness of fit – stage 1 99

Table 9: Summary of goodness of fit – stage 2 99

Table 10: Comparison of scheme 15 and scheme 16 – stage 3 110

Table 11: Inventory properties of the sections used in the demonstration 142

LIST OF FIGURES

Figure 1: Kirchhoff plate element with typical d.o.f. shown at node 3 10

Figure 2: Effects of temperature gradient on slab curling 16

Figure 3: Deflection profile due to change in the temperature differential 17

Figure 4: Daily and seasonal variation in pavement temperature gradient 19

Figure 5: Effect of shrinkage gradient on slab curling 20

Figure 6: Shrinkage modeled using equivalent temperature gradient 21

Figure 7: Stress distribution due to drying shrinkage 21

Figure 8: Effect of moisture gradient on slab warping 23

Figure 9: Critical loading conditions 24

Figure 10: Critical loading condition for top-down stresses 24

Figure 11: Symbolic expression of reference point and general point 27

Figure 12: An overview of the development of experimental matrix 30

Figure 13: Combining base and subbase layers 33

Figure 14: Comparison of variation in results for combined base/subbase and no subbase approaches 34

Figure 15: Combining CTE and thermal gradient 35

Figure 16: Load configurations considered in the study 37

Figure 17: Sensitivity trend due to the variation in base/subbase thickness 45

Figure 18: Sensitivity trend due to the variation in modulus of subgrade reaction ...45

Figure 19: Sensitivity trend due to the variation in thermal strain gradient 46

Figure 20: Overview of structural model 49

Figure 21: Required components for the analytical tool 50

Figure 22: Procedure of determining critical load location 51

Figure 23: Validation and determination of critical load location 54

Figure 24: Example validation and determination (bottom stresses, MI-9, 177-in. joint spacing) 56

Figure 25: Example validation and determination (bottom stresses, MI-20, 177-in. joint spacing) 56

Figure 26: Example sensitivity plots of bottom-up stresses 61

Figure 27: Example sensitivity plots of top-down stresses 66

Figure 28: Impact of lateral support condition 71

Figure 29: Slab curling due to different types of thermal gradients 73

Figure 30: Effect of longitudinal joint AGG factor on stress magnitude 80

Figure 31: Interpolation process 93

Figure 32: Validation procedure 96

Figure 33: Overview of validation process 97

Figure 34: Validation results – stage 1 100

Figure 35: Validation results – stage 2 104

Figure 36: Validation results – stage 3 108

Figure 37: Overall process of the proposed approach to influence surface 117

Figure 38: Typical loading grids, reference point, and unit load 120

Figure 39: Impact of tire contact pressure and aspect ratio on pavement stress 122

Figure 40: Typical influence surfaces (in psi) 130

Figure 41: Multi-axle truck configuration used in the verification process 131

Figure 42: Verification results 133

Figure 43: Typical determination of critical load location for bottom-up stress 139

Figure 44: Typical determination of critical load location for top-down stress ... 140

Figure 45: Impact of variations in slab and base elastic moduli 144

Figure 46: Typical truck configuration extracted from the WIM database 145

Figure 47: Pavement stress history plots for the DGAB sections 146

Figure 48: Stress ratio history plots for the DGAB sections 147

Figure 49: Fatigue damage based on peak stresses from influence surfaces 148

Figure 50: Time-series transverse cracking on the DGAB sections 149

Figure 51: Single unit truck configuration used in the demonstration study 150

Figure 52: Interaction between axle spacing and slab length on bottom-up stress 152

Figure 53: Interaction between axle spacing and slab length on top-down stress 155

Figure 54: Impact of slab length on thermal stress 157

Figure 55: Combined loading and thermal stresses 158

CHAPTER I

INTRODUCTION

This dissertation focused on the impact of the interaction between structural, environmental, and loading factors on mechanistic responses of rigid pavements. Computed through the mechanistic analysis approach, the pavement responses could be linked to rigid pavement performance, which in this study refers to load related performance such as transverse cracking. This introductive chapter is comprised of four parts: background, problem identification, research objectives, and chapter overview.

1.1 Background

The ability to simulate numerous pavement conditions in an economically feasible fashion makes the mechanistic analysis approach an attractive tool in the study of rigid pavements. Mechanistic responses, the results obtained from the mechanistic analysis, e.g. pavement stresses, are directly influenced by the interaction between structural, environmental, and loading factors. Then, through appropriate transfer functions, the computed mechanistic responses could be linked to rigid pavement performance. Therefore, the understanding of the impact of the interaction between such factors on mechanistic responses would also lead to the understanding of pavement performance.

Realizing the importance of such a connection, researchers in the area of rigid pavement engineering have been devoting much of their effort to develop and enhance the mechanistic approach to become more realistic; over the decades, the mechanistic analysis of rigid pavements was substantially improved from overly simplified closed-

form solutions to sophisticated finite element models. In the 1920's, the closed-form solutions were only capable of dealing with a rigid pavement system of a single slab, infinite dimensions, a single layer, and a full contact interface. Recently developed finite element models have the ability to cope with several issues related to a realistic model of pavement conditions, including, but not limited to, multi-slab system, finite slab dimensions, multi-layer system, load transfer devices, aggregate interlock, the existence of a gap between layers, the application of thermal gradients, and the simulation of complex load configurations. The improved analysis method has raised many more issues; as a result, the finite element method of rigid pavements is continuously being developed. Several issues relating the finite element models have been well emphasized; however, the study on the effect of the interaction between the various factors on mechanistic responses through the use of the developed finite element models still remains relatively unestablished.

1.2 Problem identification

Fundamentally, it is crucial to establish a thorough understanding of the impact of the interaction between structural, environmental, and loading factors on mechanistic responses. However, studying mechanistic responses of rigid pavements under a limited number of scenarios could yield valuable information only to a certain level as the findings obtained from such a study only remain valid for the limited variable combinations addressed in the study. On the other hand, to capture the interactive responses between the variables, a parametric study must contain the entire possible variable combinations, which requires an impractically massive experimental matrix and

is virtually unachievable under limitations of time and fund. Evidently, the success in conducting such a parametric study can only be achieved through strategically reducing the size of the experimental matrix without compromising the validity of the findings.

Also, for the analysis with the consideration of traffic loading, issues related to the mechanistic analysis of rigid pavements are further complicated by the variety in characteristics of axle spacing lengths and axle weights throughout the design life. In addition to the configurations of the traffic loading, the locations of traffic configurations applied in the mechanistic analysis process are as important. With respect to the design of rigid pavements, highway pavements generally have a maximum stress value significantly lower than the concrete modulus of rupture. Unlike the design of bridge decks or airport pavements, where the design criteria is usually based on the worst case loading scenario, the design of highway rigid pavements for cracking prevention is based on load repetitions, which influence fatigue behavior. Already subjected to a massive experimental matrix, a parametric study needs to extend the covered area to even more combinations of load locations to effectively address the impact of loading factors on mechanistic responses. Therefore, it is necessary to develop an analysis technique to simultaneously account for the variations of load configurations, both axle spacing lengths and axle weights, and load locations in a practical time frame.

1.3 Research objectives

This research investigated the impact of various parameters, and their interrelationship, on mechanistic responses of rigid pavements obtained from finite element method. There are four primary objectives achieved in this dissertation. The first objective was to

perform a parametric study on current and anticipated rigid pavements, with considerations of loading, climatic, material, subgrade support, and construction parameters. It was also essential to establish a protocol for the development of a comprehensive interpolation scheme that addressed the condition changes (e.g., traffic spectra distribution, thermal gradient distribution, material property variation, etc.) in the calculation of mechanistic responses. Another objective was to develop influence surfaces for rigid pavements to address the impact of complex load configurations on pavement responses and also the impact of lateral wander. Investigating the impact of the interaction between structural, environmental, and loading factors on mechanistic responses was the last objective.

1.4 Chapter overview

This dissertation – the study of the impact of the interaction between structural, environmental, and loading factors on mechanistic responses of rigid pavements – is outlined as follows:

Chapter 2 contains a synopsis of historic milestones of several topics involved with this study. Numerous related published articles are categorized into three groups: finite element analysis of rigid pavements, factors affecting mechanistic responses, and application of influence surfaces.

Chapter 3 explores the sensitivity of mechanistic responses with the variation of structural, loading and environmental variables through the finite element method. An extensive parametric study was conducted on a complete factorial experimental matrix that contains 43,092 combinations of concrete slab thickness, base/subbase thickness,

modulus of subgrade reaction, joint spacing, lateral support condition, axle configurations, and truck configurations within the practical range for the state of Michigan. Strategies used to reduce the size of the experimental matrix are discussed. The analysis processes and assumptions in relation to the parametric study are also briefly discussed.

Based on the finite element results from Chapter 3, Chapter 4 presents the potential use of an interpolation scheme as a means to predict stresses in rigid pavements. Developed based on least-squares criteria, the interpolation scheme only requires a limited number of finite element results as anchor results at nodal points to calculate a least-squares coefficient vector. An unlimited number of design scenarios, then, can be analyzed with the use of the interpolation scheme in short time. This chapter also presents the validation process of the results obtained from the interpolation scheme. This chapter also briefly discusses the potential implementation of the interpolation scheme for developing a full catalog of mechanistic responses that may cover over a million possible design scenarios in the case of the damage calculation process. Furthermore, an example calculation using the interpolation scheme is presented in this chapter.

In Chapter 5, the development of influence surfaces for rigid pavements is presented as a means to address the impact of complex loading configurations, load locations, and structural features on mechanistic responses. An influence surface is developed by analyzing for mechanistic responses at the midslab under the wheel path. This midslab corresponds to a unit point load at various locations all over the pavement surface. This chapter also elaborates the potential applications of the proposed technique. The following four tasks in the field of rigid pavement study were performed using the

influence surface technique: rapid pavement stress calculation, determination of critical load location, pavement stress history, and investigation of the interaction between load configuration and structural feature.

Chapter 6 presents the conclusions of the research. This chapter also suggests future subsequent research.

CHAPTER II

LITERATURE REVIEW

This chapter reviews numerous related literature to determine what previous research have been conducted on mechanistic analysis of rigid pavements, especially with regard to the impact of the interaction between structural, environmental, and loading factors on mechanistic responses. Three main areas of the reviewed articles are: finite element analysis of rigid pavements, factors affecting mechanistic responses, and application of influence surfaces.

2.1 Finite element analysis of rigid pavements

Finite element method is basically a numerical approach to estimate the solutions to the partial differential equations that govern the characteristics of rigid pavements. As matrix manipulation and a series of numerical integrations are unavoidable parts of the method, the finite element analysis of rigid pavements only became practical in the 1970's after the development of efficient computation. The finite element application for rigid pavements has been enhanced over the past decades to address numerous factors related to mechanistic responses into the analysis (Huang and Wang, 1973; Tabatabaie and Barenberg, 1978; Chou and Huang, 1981; Ozbeki et al., 1985; Davids and Mahoney, 1999). Three aspects of finite element analysis of rigid pavements are reviewed: plate theory, pavement foundation, and the mathematical process of the finite element analysis.

Plate theory

In this study, a two-dimensional finite element model idealized using the Kirchhoff theory, ISLAB2000, was employed to address the impact of the interaction between the multi-factors on mechanistic responses. The Kirchhoff theory is applicable to thin plates with an assumption of no shear deformation, while thick plates with an inclusion of shear deformation in the computation would require the Mindlin theory (Cook et al., 1989; Reddy, 1993). Since rigid pavement thickness is significantly less than the other two dimensions, with the exception of airport pavement slabs, transverse shear deformation is insignificant and can be neglected. With the consideration of the Kirchhoff theory, therefore, all stress-strain relation terms that involved shear deformation vanish and the reduced plane stress-strain relation matrices for an isotropic material can be shown below.

$$\begin{Bmatrix} \sigma_x \\ \sigma_y \\ \tau_{xy} \end{Bmatrix} = \begin{bmatrix} E' & E'' & 0 \\ E'' & E' & 0 \\ 0 & 0 & G \end{bmatrix} \cdot \left(\begin{Bmatrix} \varepsilon_x \\ \varepsilon_y \\ \gamma_{xy} \end{Bmatrix} - \begin{Bmatrix} \alpha \cdot T \\ \alpha \cdot T \\ 0 \end{Bmatrix} \right) \tag{1}$$

where σ_x *and* σ_y = normal stresses in x and y directions

τ_{xy} = shear stress

ε_x *and* ε_y = normal strains in x and y directions

γ_{xy} = shear strain

α = coefficient of thermal expansion of concrete

μ = Poisson's ratio of concrete

T = temperature differential between top and bottom of concrete

$$E' = \frac{E''}{\mu} = \frac{E}{1-\mu^2} \tag{2}$$

$$G = \frac{E}{2\cdot(1+\mu)} \tag{3}$$

Based on the stress-strain relation matrices, the stiffness matrix of concrete slab $[K_p]$ may be derived using the following formula.

$$[K_p] = \int_A [B]^T \cdot [D_k] \cdot [B]\, dA, \tag{4}$$

where

[B] = the strain-displacement matrix (will be discussed later).

A = area boundary of an element

$$[D_k] = \begin{bmatrix} D & \mu\cdot D & 0 \\ \mu\cdot D & D & 0 \\ 0 & 0 & \frac{(1-\mu)\cdot D}{2} \end{bmatrix} \tag{5}$$

D = flexural rigidity

$$D = \frac{E\cdot t^3}{12\cdot(1-\mu^2)}, \tag{6}$$

where t represents the slab thickness.

Pavement foundation

Theoretically, in the case of slab-on-grade, rigid pavement can be approximately considered as one elastic structure supported by a foundation model called the Winkler foundation. There are a great many other foundation models available for rigid pavement foundation idealization; however, the Winkler foundation is traditionally used and

considered as the most effective model. Details of characteristics, advantages, and disadvantages of the Winkler foundation will not be discussed at this time. Another name of the Winkler foundation is "Dense Liquid" foundation because this foundation simulates the behavior of the subgrade or original soil under concrete slab by providing a vertical resistant pressure equal to βw, when w is vertical deflection and β is the Winkler foundation modulus (modulus of subgrade reaction). The stiffness matrix of the foundation is written below in matrix form.

$$[K_f] = \int_A \beta \cdot [N]^T \cdot [N]\, dA, \tag{7}$$

where [N] = interpolation functions matrix (will be discussed later)

A = area boundary of an element.

Mathematical process of the finite element method

Since rigid pavement has rectangular geometry, it can be discretized using rectangular linear FE with three degrees of freedom at each node: one vertical displacement, and two horizontal rotations as shown in Figure 1. In other words, one FE contains twelve degrees of freedom, meaning each element has a 12x12 stiffness matrix, a 12x1 force vector, and a 12x1 displacement vector.

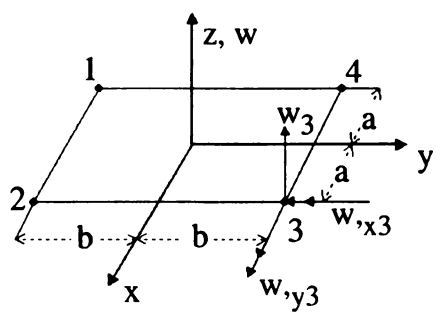

Figure 1: Kirchhoff plate element with typical d.o.f. shown at node 3

Since Kirchhoff plate elements provide interelement continuity of vertical displacements and rotations in the x- and y-directions, the elements can be considered C^1 elements; therefore, interpolation functions for C^0 elements, like Lagrange's interpolation formula, may not be applied. The Hermitian interpolation function, one of interpolation functions for C^1 elements, can be used for this situation (thin plate elements). For an element that has four nodes (1, 2, 3, and 4), Hermitian interpolation functions can be derived using the following formulae:

$$\begin{aligned} w = {} & N_1 \cdot w_1 + N_{x1} \cdot \theta_{x1} + N_{y1} \cdot \theta_{y1} + N_2 \cdot w_2 + N_{x2} \cdot \theta_{x2} + N_{y2} \cdot \theta_{y2} \\ & + N_3 \cdot w_3 + N_{x3} \cdot \theta_{x3} + N_{y3} \cdot \theta_{y3} + N_4 \cdot w_4 + N_{x4} \cdot \theta_{x4} + N_{y4} \cdot \theta_{y4} \end{aligned}, \tag{8}$$

where

$$[N_1 \; N_{x1} \; N_{y1}] = \frac{X_1 Y_1}{16} \cdot [X_1 Y_1 - X_2 Y_2 + 2X_1 Y_2 + 2Y_1 Y_2 \quad 2bY_1 Y_2 \quad -2aX_1 X_2], \tag{9}$$

$$[N_2 \; N_{x2} \; N_{y2}] = \frac{X_2 Y_1}{16} \cdot [X_2 Y_1 - X_1 Y_2 + 2X_1 Y_2 + 2Y_1 Y_2 \quad 2bY_1 Y_2 \quad 2aX_1 X_2], \tag{10}$$

$$[N_3 \; N_{x3} \; N_{y3}] = \frac{X_2 Y_2}{16} \cdot [X_2 Y_2 - X_1 Y_1 + 2X_1 Y_2 + 2Y_1 Y_2 \quad -2bY_1 Y_2 \quad 2aX_1 X_2], \tag{11}$$

$$[N_4 \; N_{x4} \; N_{y4}] = \frac{X_1 Y_2}{16} \cdot [X_1 Y_2 - X_2 Y_1 + 2X_1 Y_2 + 2Y_1 Y_2 \quad -2bY_1 Y_2 \quad -2aX_1 X_2], \tag{12}$$

$$X_1 = 1 - \frac{x}{a}, \tag{13}$$

$$X_2 = 1 + \frac{x}{a}, \tag{14}$$

$$Y_1 = 1 - \frac{y}{b}, \tag{15}$$

$$Y_2 = 1 + \frac{y}{b}. \tag{16}$$

Now the interpolation functions can be written in matrix form 1x12 as shown below.

$$[N] = [N_1 \quad N_{x1} \quad N_{y1} \quad N_2 \quad N_{x2} \quad N_{y2} \quad N_3 \quad N_{x3} \quad N_{y3} N_4 \quad N_{x4} \quad N_{y4}] \tag{17}$$

Strain-displacement matrix [B] can also be written in matrix form 3x12 as shown below.

$$[B] = -\begin{bmatrix} \frac{\partial^2 N_1}{\partial x^2} & \frac{\partial^2 N_{x1}}{\partial x^2} & \frac{\partial^2 N_{y1}}{\partial x^2} & \cdots & \frac{\partial^2 N_{y4}}{\partial x^2} \\ \frac{\partial^2 N_1}{\partial y^2} & \frac{\partial^2 N_{x1}}{\partial y^2} & \frac{\partial^2 N_{y1}}{\partial y^2} & \cdots & \frac{\partial^2 N_{y4}}{\partial y^2} \\ 2\cdot\frac{\partial^2 N_1}{\partial x \partial y} & 2\cdot\frac{\partial^2 N_{x1}}{\partial x \partial y} & 2\cdot\frac{\partial^2 N_{y1}}{\partial x \partial y} & \cdots & 2\cdot\frac{\partial^2 N_{y4}}{\partial x \partial y} \end{bmatrix} \tag{18}$$

From the previous section, the stiffness matrix of each element [K_e] (12x12) can be derived as follows:

$$[K_p]\cdot\{u_p\} + [K_f]\cdot\{u_f\} = \{r_e\} \quad , \tag{19}$$

$$\text{but} \quad \{u_p\} = \{u_f\} = \{u_e\}, \tag{20}$$

$$[K_e]\cdot\{u_e\} = \{r_e\}, \tag{21}$$

$$[K_e] = [K_p] + [K_f], \tag{22}$$

where $\{u_p\}$ = slab displacement vector,

$\{u_f\}$ = foundation displacement vector,

$\{u_e\}$ = element displacement vector (12x1),

$$\{u_e\} = \begin{Bmatrix} w_1 \\ \theta_{x1} \\ \theta_{y1} \\ w_2 \\ \theta_{x2} \\ \theta_{y2} \\ w_3 \\ \theta_{x3} \\ \theta_{y3} \\ w_4 \\ \theta_{x4} \\ \theta_{y4} \end{Bmatrix}, \tag{23}$$

$\{r_e\}$ = element force vector (12x1),

$$\{r_e\} = \int_A [B]^T \cdot [D_K] \cdot \{\kappa_O\}\, dA, \tag{24}$$

$$\text{where } \{\kappa_O\} = \begin{bmatrix} \frac{\alpha \cdot T}{t} & \frac{\alpha \cdot T}{t} & 0 \end{bmatrix}^T \tag{25}$$

The global stiffness matrix and force matrix can be computed based on the element stiffness matrix and element force matrix. The concept of generating the element stiffness matrix and the element force vector into the global stiffness matrix and global force vector is exactly the same as the concept of using the Boolean matrix that is applicable for C^0 elements; however the method is slightly different. This is because each node of a Kirchhoff element has 3 degrees of freedom. This means the element stiffness matrix, which is actually 12x12, can be considered 4x4 and the element force vector, which is actually 12x1, can be considered 4x1 in order to generate them into the global system as shown below.

$$[K_e] = \begin{bmatrix} K_{11(3x3)} & K_{12(3x3)} & K_{13(3x3)} & K_{14(3x3)} \\ K_{21(3x3)} & K_{22(3x3)} & K_{23(3x3)} & K_{24(3x3)} \\ K_{31(3x3)} & K_{32(3x3)} & K_{33(3x3)} & K_{34(3x3)} \\ K_{41(3x3)} & K_{42(3x3)} & K_{43(3x3)} & K_{44(3x3)} \end{bmatrix} \quad (26)$$

$$\{r_e\} = \begin{Bmatrix} r_{1(3x1)} \\ r_{2(3x1)} \\ r_{3(3x1)} \\ r_{4(3x1)} \end{Bmatrix} \quad (27)$$

Once the global stiffness matrix and global force vector are derived, the displacement vector of the global system can be computed.

$$\{U\}_{3N\times 1} = [KG]^{-1}_{3N\times 3N} \cdot \{F\}_{3N\times 1} \quad (28)$$

where {U} = global displacement vector,

[KG] = global stiffness matrix,

{F} = global force vector,

N = number of nodes in global system

2.2 Factors affecting mechanistic responses

The interaction between structural, environmental, and loading factors affects mechanistic responses of rigid pavements. The design of the rigid pavements mainly governs the structural feature inputs to the finite element analysis, including, but not limited to, layer thicknesses, slab dimensions, joint design, lateral support condition, layer properties, and modulus of subgrade reaction. Therefore, the details of structural inputs will not be further discussed. Without any controls over their conditions, the finite element analysis inputs, addressing environmental and loading factors, require further consideration.

Environmental factors

It has been well known that environmental effects on rigid pavements can be accounted for in term of temperature differential between the top and bottom layers of the slab. Positive temperature gradient in the daytime (the top layer is warmer than the bottom layer) contributes to downward curling. In the nighttime, the top layer of the slab is cooling down, but the bottom layer still remains warm; rigid pavements will have a negative temperature gradient (the bottom layer is warmer than the top layer), contributing to upward curling.

Slab curling shape (concave or convex) is very important to the analysis and design because it results in different types of stresses in pavements. For upward curling, the top layer of the slab contracts, while the bottom layer expands with respect to the neutral axis; however, the concrete slab weight will try to move the corners of the slab down. Negative moment due to the slab weight will cause a tension at the top of the slab layer and a compression at the bottom of the slab. In contrast to upward curling, the top of the slab expands, while the bottom of the slab contracts with respect to the neutral axis for downward curling; the corners of the slab will move down but the slab center will lift up. Consequently, the slab weight will try to move its center down, causing tension at the bottom and compression at the top of the slab. Figure 2 illustrates the concepts of curling due to temperature differentials (Armaghani et al., 1987).

Note that thermal gradients across the concrete slab depth may not be linear in reality. To effectively assess the impact of such a non-linear thermal gradient, the concept of temperature-moment could be used to normalize the effect of the non-linear thermal gradient to an equivalent linear thermal gradient (Janssen and Snyder, 2000).

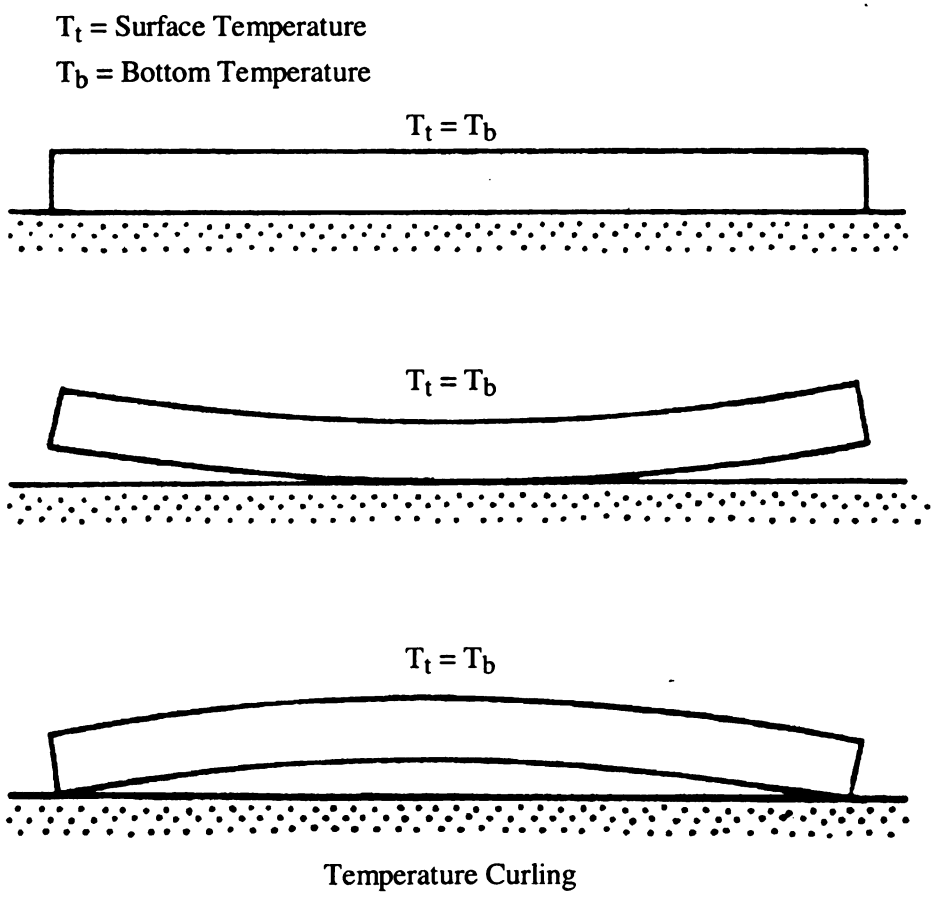

Figure 2: Effects of temperature gradient on slab curling

However, several researchers (Armaghani, 1987; Byrum, 2000; Eisenmann and Leykauf, 1990; Janssen, 1987; Poblete et al., 1988; Yu et al., 1998) observed that many rigid pavements maintained an upward curl even when they were subjected to zero temperature gradients (temperature at the top was the same as at the bottom of the slab). Moreover, even in low positive temperature gradients, some of rigid pavements still appeared to curl up as shown in Figure 3 (Armaghani et al., 1987).

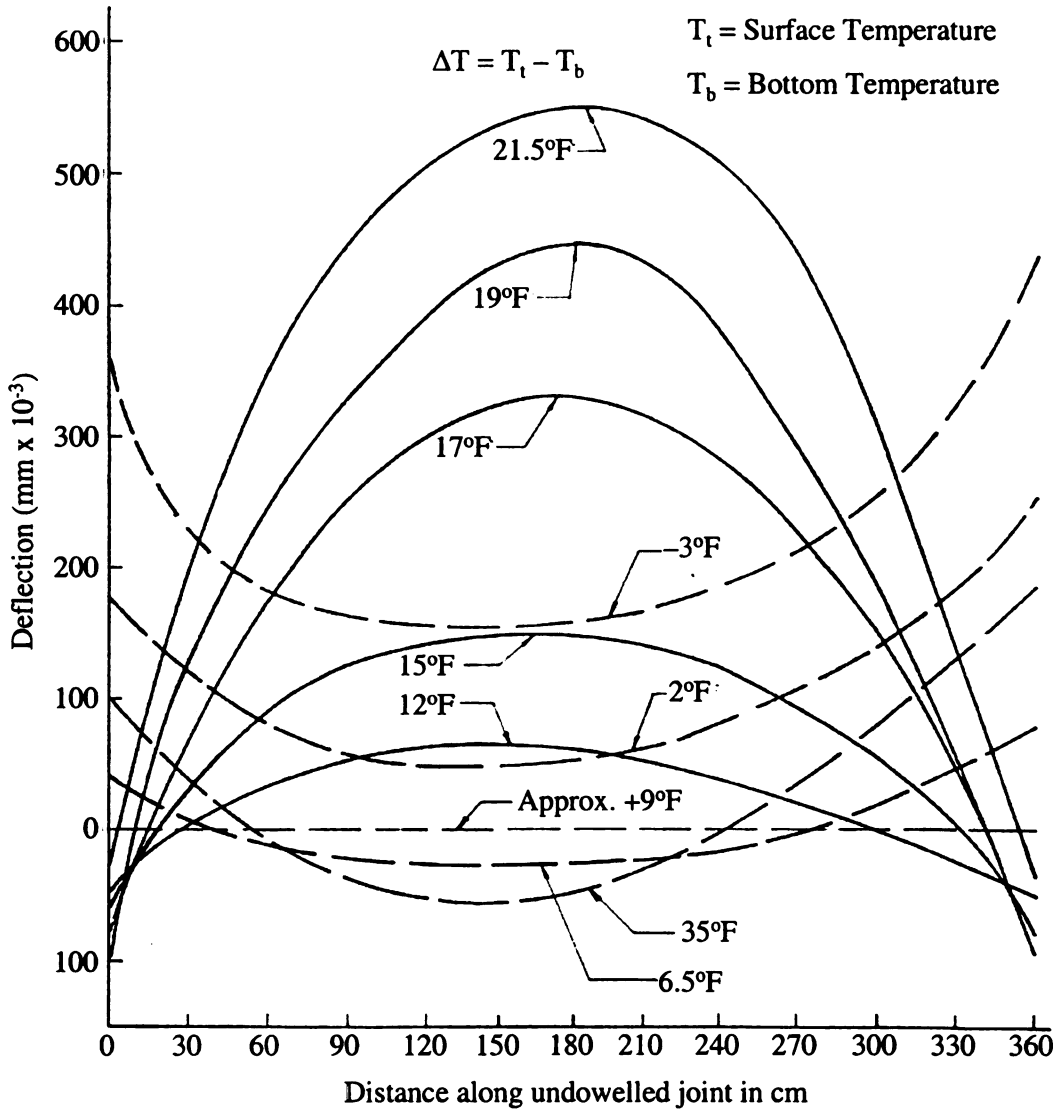

Figure 3: Deflection profile along a joint due to change in the temperature differential (Armaghani, 1987)

Permanent upward curl in rigid pavement can be explained by the interaction of the following causes: temperature gradient locked into the slab during the setting period

(construction curl), drying shrinkage at the slab surface, and moisture expansion at the slab bottom.

The basic concept of construction curl is that when the concrete material in rigid pavements is setting and hardening, the temperature gradient at that time will be locked into the slab without curling. This is because at an early age, concrete does not have a sufficient stiffness to curl its edges or corners. However, after hardening, the locked in temperature gradient will have a very important effect on the behavior of the slab in that it will become a temperature gradient of the opposite sign. For example, if the slab sets, when exposed to a +15 °F temperature gradient, the effect of the curling at a zero temperature differential after hardening will be the same as if it was exposed to a -15 °F temperature differential, and the slab will be flat again, when exposed to a +15 °F temperature differential. Technically, the slab has a locked-in temperature differential of -15 °F. Since the construction of pavements is usually done in the daytime, when the slab is subjected to a positive temperature gradient, most of rigid pavements may have a locked-in negative temperature gradient, and this can result in an upward curl of the slab, even when exposed to a zero temperature gradient.

The opposite sign of temperature gradient at hardening time can be simply quantified in order to consider the effect of construction curl and also can be rationally superimposed to the temperature gradient. However, due to the seasonal and daily variation in temperature gradient, it might not be easy to quantify locked in temperature gradients. It would be reasonable to consider several values of locked in temperature throughout a project as illustrated in the figure below (Yu et al., 2001).

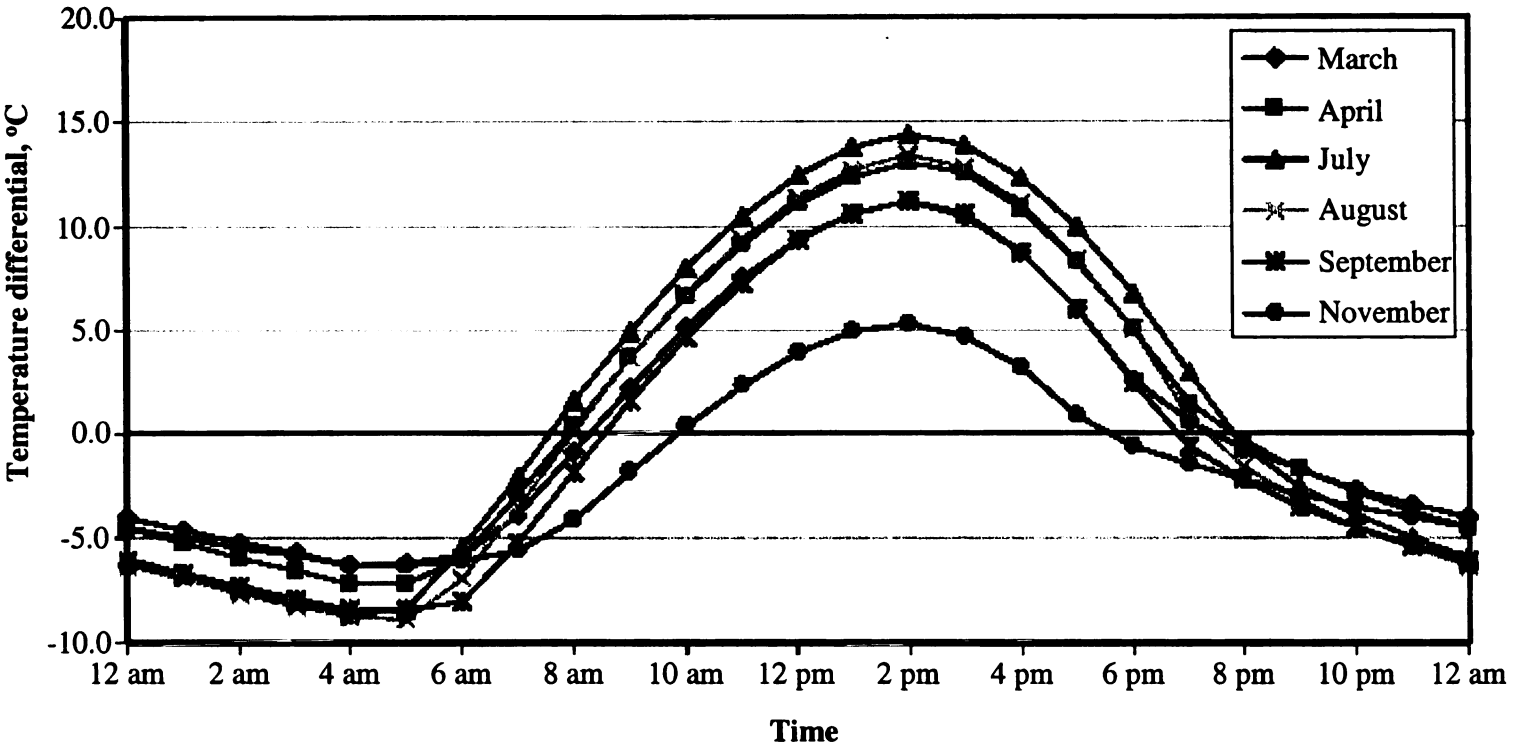

Figure 4: Daily and seasonal variation in pavement temperature gradient

When exposed to ambient humidity (lower than 100 % relative humidity), removal of water from concrete can cause strain associated with drying shrinkage. It was found that the loss of moisture in concrete slab was generally concentrated within the 2 in. below the surface (Eisenmann and Leykauf, 1990; Janssen, 1994). Therefore, the effect of drying shrinkage will be very high only for the top 2 in. of the slab. Contraction of the pavement surface due to the high level of drying shrinkage at the top layer of the slab can cause upward curling. Figure 5 shows upward curling due to shrinkage differential (Armaghani, 1987).

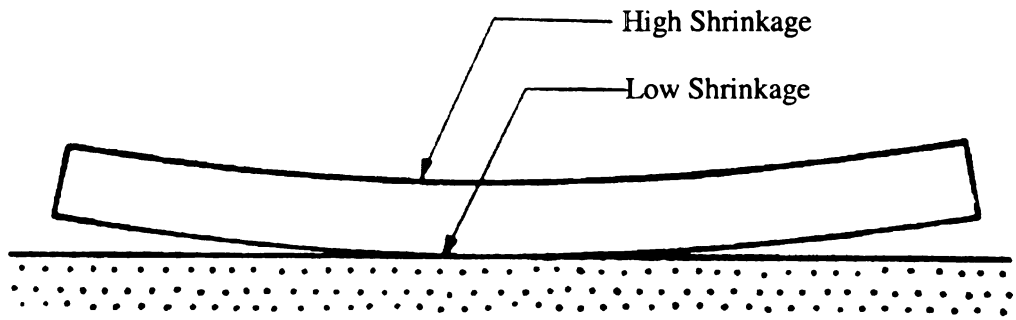

Figure 5: Effect of shrinkage gradient on slab curling

With finite element application, effect of drying shrinkage can be accounted for in terms of equivalent temperature gradient applying to only the top 2 inches of the slab as shown in Figure 6 (Heath et al., 2001).

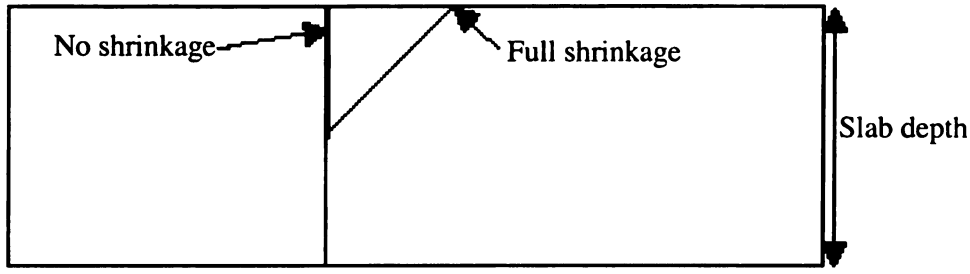

Figure 6: Shrinkage modeled using equivalent temperature gradient

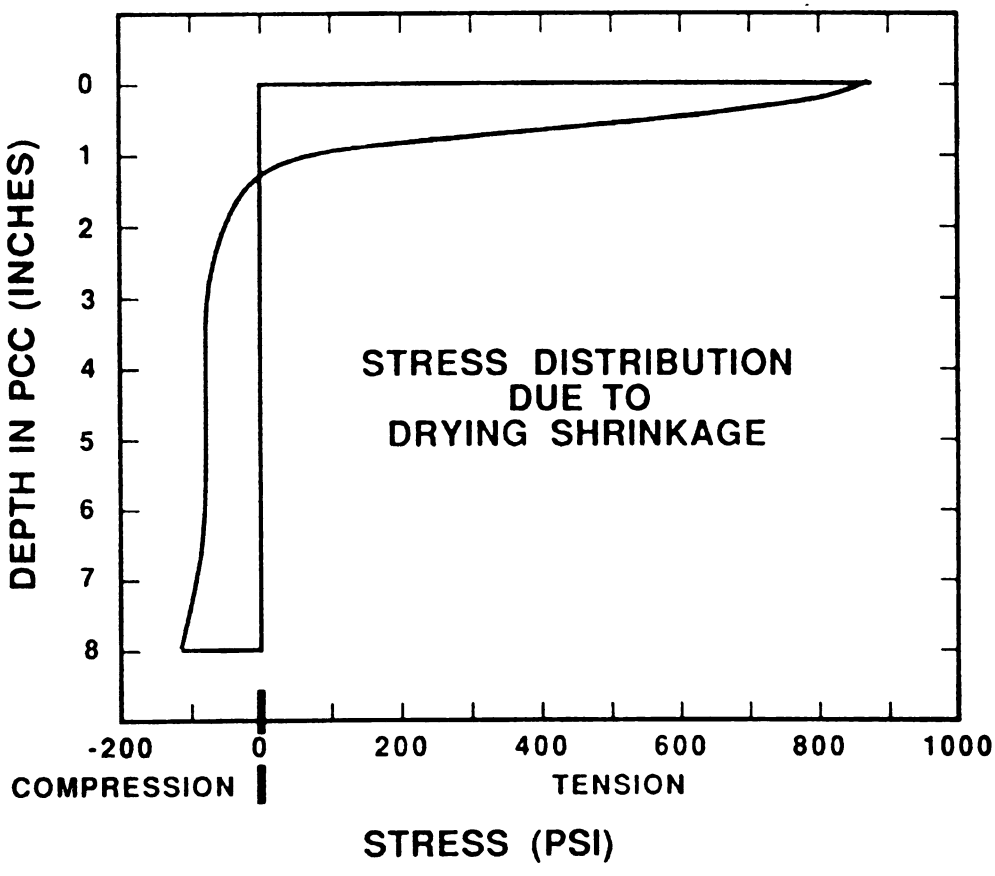

Figure 7: Stress distribution due to drying shrinkage (Janssen 1987)

Shrinkage strain can be considered as thermal strain; with known material property (coefficient of thermal expansion), equivalent temperature differential at the slab surface can be computed using the following formula.

$$\varepsilon_{sh} = T_{sh} \cdot \alpha \tag{29}$$

Where T_{sh} = Equivalent temperature differential due to shrinkage

α = Coefficient of thermal expansion of concrete

ε_{sh} = Shrinkage strain

However, the effect of drying shrinkage on the slab curling estimated using the above formula has to be adjusted with considerations of the shrinkage characteristic and the effect of creep in relaxing shrinkage strain. With rising elastic modulus and shrinkage strain, the upward deflection will be larger. This means the effect of drying shrinkage on upward curling in a new pavement (low elastic modulus and low shrinkage strain) is small and may be neglected (Eisenmann and Leykauf, 1990). For old pavements, however, sustained stress from the slab weight due to upward curling can result in creep relaxation that reduces stress due to shrinkage up to 50 % (Altoubat, 1999).

Capillary sorption can also cause expansion in concrete, when water is sufficiently supplied to the concrete. Most of the time, pavements have a positive moisture gradient (the top of the slab is drier than the bottom) and infrequently may have a negative moisture gradient for a short period after a rainfall. Therefore, the bottom of the slab will usually expand as compared to the neutral axis, and consequently this will result in a warping (an upward curling due to a moisture gradient) in rigid pavements as shown in Figure 8 (Armaghani, 1987).

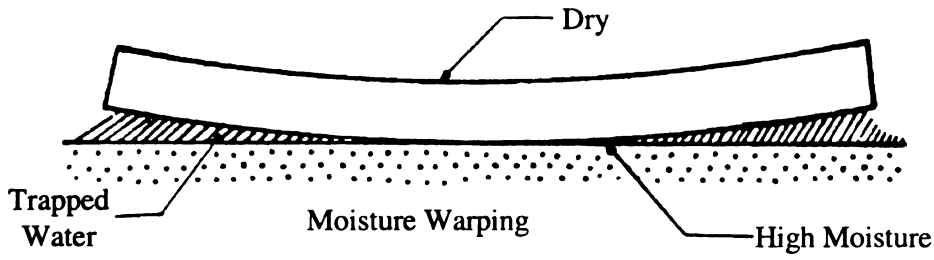

Figure 8: Effect of moisture gradient on slab warping

Basically, the existence of a moisture gradient causes an upward warping in rigid pavements. To analyze the effect of a moisture gradient on warping and its interaction with other causes using the finite element method, an equivalent negative temperature gradient can be estimated. Fang (2001) recommended that a factor of 0.5 can be multiplied to the daily peak positive temperature gradient in the summer and a factor of 2 for the winter to account for the effect of a moisture gradient.

Loading factors

The use of the finite element method allows the two aspects of loading factors, configuration and location, to be simultaneously addressed. Traditionally, rigid pavements are analyzed for the edge loading condition, since it produces maximum stress at the bottom of the slab. However, in the case of high locked-in negative temperature gradient, caused by construction curl, drying shrinkage gradient, and moisture gradient, the edge loading condition that had traditionally been considered as the critical loading condition is not the most critical loading case anymore. Instead, the corner loading condition is the critical loading condition because it magnifies the effect of the negative

moment over the upward curled pavement (Yu et al., 2001). Both the upward curling and corner loading condition cause tension at the top of the slab, causing top-down cracking in rigid pavements. As illustrated in Figure 10, with multi-axle trucks, top-down stress situation can be magnified more when axles are placed near transverse joints of a slab. Figures 9 and 10 illustrate the various loading conditions for jointed plain concrete pavements (Yu et al., 2001).

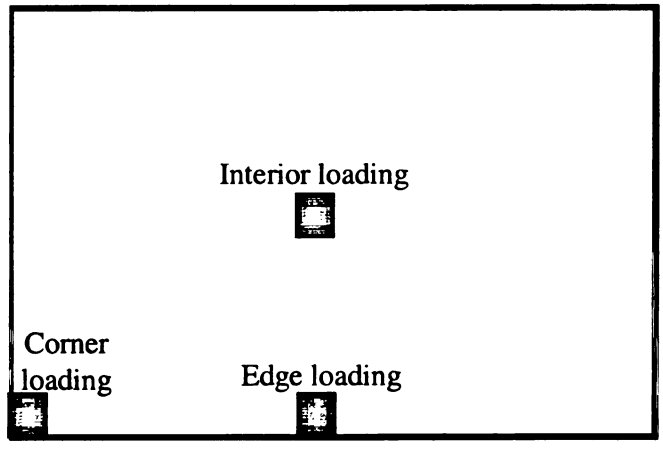

Figure 9: Critical loading conditions (Yu et al., 2001).

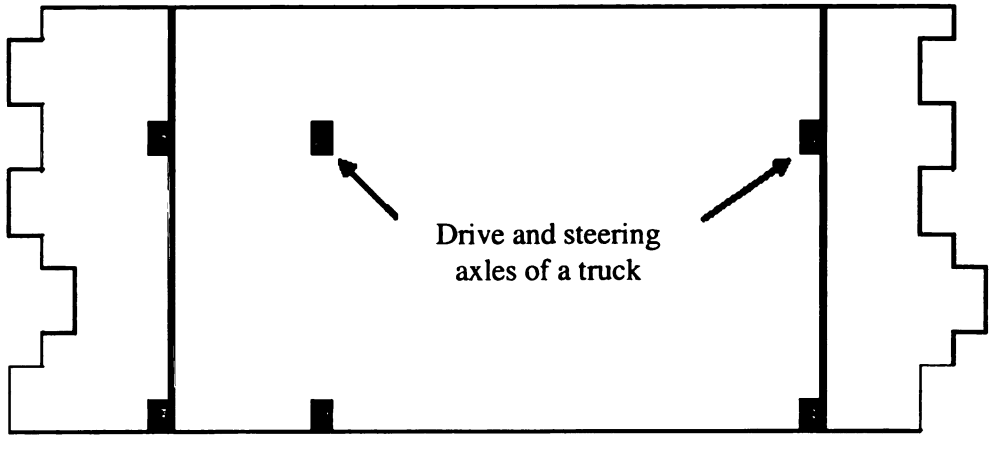

Figure 10: Critical loading condition for top-down stresses (Yu et al., 2001).

Due to the complexity of multi-axle truck configurations, the critical loading conditions can vary substantially, depending on axle spacing lengths, weights, and structural parameters. While the direct application of the finite element analysis may address the impact of loading factors in a time-consuming fashion, the use of influence surface technique can tackle complex loading scenarios effectively and efficiently.

2.3 Application of influence surfaces

The technique of influence surfaces was first introduced in the 1910's. Although the term influence surface was not directly mentioned in his work, Hencky may have been the first to develop influence surfaces for deflections of elastic plates by applying Maxwell's theorem of reciprocal deflections (Hencky, 1913). More than a decade later, a comprehensive work on plate theory and the influence surfaces of plate deflections, which became the basic theory of influence surfaces, was published (Nádai, 1925). However, deflections of the structure are of lesser interest, from a design standpoint, as compared to internal forces, such as the bending moment or shear force. Westergaard was among the first to develop influence surfaces for internal forces (Westergaard, 1930). While Westergaard is known for being a pioneer in the mechanistic analysis of rigid pavements, his work on influence surfaces only focused on the influence fields of bridge decks. Since that time, many researchers have developed influence surfaces for different internal forces, boundary conditions, and reference points; yet, application of influence surfaces remained limited to bridge decks (Lansdown, 1966; Oran and Lin, 1973; Dowling and Bawa, 1975; Kawama et al., 1980; Williams and du Preez, 1980; Imbsen and Schamber, 1982; Memari and West, 1991).

For the first time, in 1976, Nayak et al. attempted to develop influence surfaces for a plate resting on a dense liquid foundation, which is the general case for rigid pavements, by applying a pinch load and differentiating the influence fields of deflections using the finite element method (Nayak et al., 1976). However, the influence surfaces developed by Nayak et al. are limited only to single slab-on-grade systems without addressing the impact of boundary slabs or an elastic base layer.

Since the first development of the influence surface technique in the early 1910's, influence surfaces have conventionally been obtained through an analytical approach, in which the formulations of the surfaces are explicitly expressed. To begin this approach, expression of the deflection contour of the structure with a unit load applied at the reference point of the influence surface must be mathematically derived. Based on the Maxwell-Betti-Reciprocal Theorem, the influence surface of deflections can then be directly obtained from the deflection contour (Hencky, 1913). As illustrated in Figure 11, if the unit load is applied at the coordinate A (u, v), and B (x, y) is a general point on the plate, then the deflection contour can be symbolically expressed as Y (u, v, x, y). Consequently, through the reciprocal system, the coordinate (u, v) denotes the coordinate of the reference point of the influence surface of deflection, while the coordinate (x, y) also denotes the point of the applied unit load. Subsequently, differentiating the influence surface of deflections then provides the influence surfaces of internal forces, such as shear or moment.

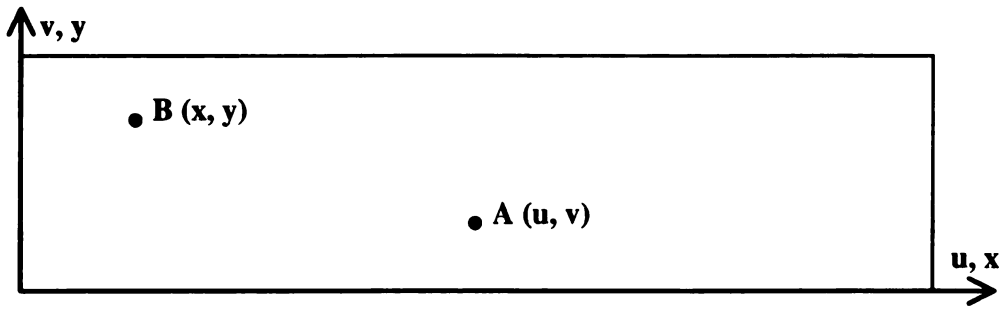

Figure 11: Symbolic expression of reference point and general point

CHAPTER III

PARAMETRIC STUDY

This chapter established the understanding of the impact of the interaction between such factors on mechanistic responses, captured through an extensive parametric study. Data collection procedure, development of the experimental matrix, and process involved with the analysis are included in this chapter, as well as documentation of the results.

3.1 Data collection

The Michigan Department of Transportation (MDOT) Technology Advisory Group (TAG) provided 14 "approved" designs for projects that were either recently constructed or were programmed for construction in the near future. The designs provided the structural parameters used for Michigan rigid pavements, e.g., cross-sections, pavement features, material properties, etc. The ranges of inputs obtained from the MDOT designs are summarized in Table 1. The details of the approved designs projects may be found in the final report to MDOT by Buch et al. (Buch et al., 2004).

In addition to these input parameters, the analytical model required the following additional parameters (i) coefficient of thermal expansion (CTE) of the concrete, (ii) thermal gradients, (iii) axle and truck configurations, (iv) Poisson's ratio and unit weight. Based on the review of the literature (Klieger and Lamond, 1994), LTPP database, Truck driver's guidebook for Michigan (Michigan Center for Truck Safety, 2001), and conversations with the TAG, ranges for these additional input parameters were established and are summarized in Table 2.

Table 1: Summary of design parameters from the 14 MDOT designs

Inputs	Minimum	Maximum
Slab thickness	9.5 in.	12.0 in.
Base thickness	4.0 in.	16.0 in.
Subbase thickness	No subbase	12.0 in.
Joint spacing	177 in.	315 in.
Lane width	12 ft	14 ft
Lateral support condition	Widened lane	
Joint design	Doweled 1.25 in. diameter at 12 in. spacing center to center	
Concrete elastic modulus	4.2×10^6 psi	
Modulus of subgrade reaction	90 psi/in.	220 psi/in.

Table 2: Ranges of input parameters obtained from other sources

Input variables	Ranges
Concrete unit weight	0.0087 lb/in.^{3}
Concrete Poisson's ratio	0.15 - 0.20
Aggregate base unit weight	0.0061 lb/in.^{3}
Aggregate base Poisson's ratio	0.35
Thermal gradient	-4 - +4 °F/in.
Coefficient of thermal expansion	3×10^{-6} - 9 x 10^{-6} in./in./°F
Location of stress	Top and bottom
Load configuration	Single axle, tandem axle,... Multi-axle (8), MI-1, MI-2,... MI-20

3.2 Experimental matrix

An experimental matrix was constructed based on the concept of complete factorial (Fisher, 1960) for all combinations of design inputs reflecting MDOT practice, climatic condition, and load configurations in Michigan. Several engineering principles and common knowledge were applied to make the experimental matrix more concise, but still provide the same level of information. An overview of the process is illustrated in Figure 12.

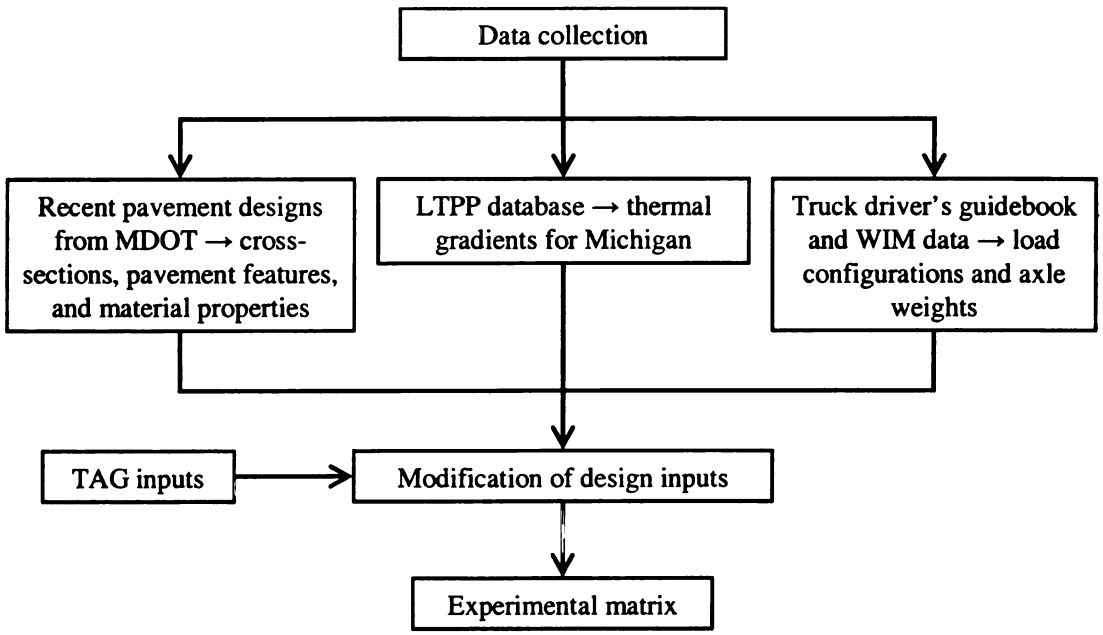

Figure 12: An overview of the development of experimental matrix

An important first step in data analysis is to ensure that the project objectives can be accomplished within the limitations of time and funds. If every combination of input parameters is to be considered, the complete factorial experimental matrix would result in millions of FE runs. To reduce the experimental matrix size, the preparation of the final matrix was achieved by carrying out the following strategies: combining variables, considering only frequently seen load configurations, and adjusting increments for non-discrete inputs.

Combining variables

Two variables are combined into one variable to reduce the number of input combinations in the experimental matrix based on an assumption that the mechanistic response computed either with one combined variable or two separate variables would be the same or approximately the same. The variables to be combined are base thickness and subbase thickness, which are combined into base/subbase thickness, and CTE (α) and thermal gradient ($\Delta T/D$), which are combined into thermal strain gradient.

Figure 13 illustrates how base thickness and subbase thickness can be combined. It is assumed that the two layers have an unbonded interface, one elastic modulus represents the combined layer, and the Poisson's ratios of the two layers are approximately the same (Khazanovich and Yu, 2001). This sensitivity study of the accuracy of the combined base/subbase thickness was conducted for the 14 MDOT designs by comparing the mechanistic responses computed based on the two-layer system (concrete and combined base/subbase layers on the top of the subgrade) and that based on the three-layer system (concrete, base and subbase layers on the top of the subgrade). In

this sensitivity study, for the three-layer system approach, an unbonded interface condition and Totski interface model (ERES Consultants, 1999) were considered between base and subbase layers and between concrete and base layers, respectively. An unbonded interface condition was considered for the two-layer system approach. It was found that the difference in the magnitudes of stresses between the two approaches is less than 4%. The results from the sensitivity study are illustrated in Figure 14 as compared with the results based on no subbase for the 14 MDOT designs.

The CTE and thermal gradient are simultaneously accounted for in terms of the product of the two variables, $\alpha(\Delta T/D)$ or thermal strain gradient. Figure 15 illustrates the sensitivity plots to validate this assumption. The sensitivity study was conducted for nine cases by comparing the mechanistic responses computed based on two analysis approaches. Analysis approach 1 consists of varying CTE values, while keeping a thermal gradient constant. Analysis approach 2 consists of keeping a CTE value constant, while varying thermal gradients.

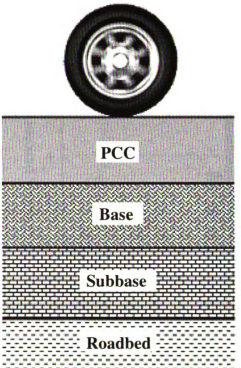

$$h_{base/subbase} = \sqrt[3]{h_{base}^3 + \frac{E_{subbase}}{E_{base}} h_{subbase}^3}$$

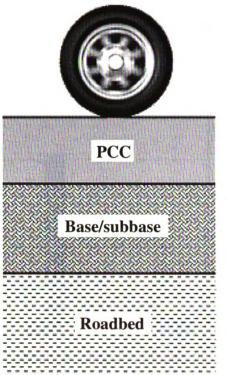

Figure 13: Combining base and subbase layers

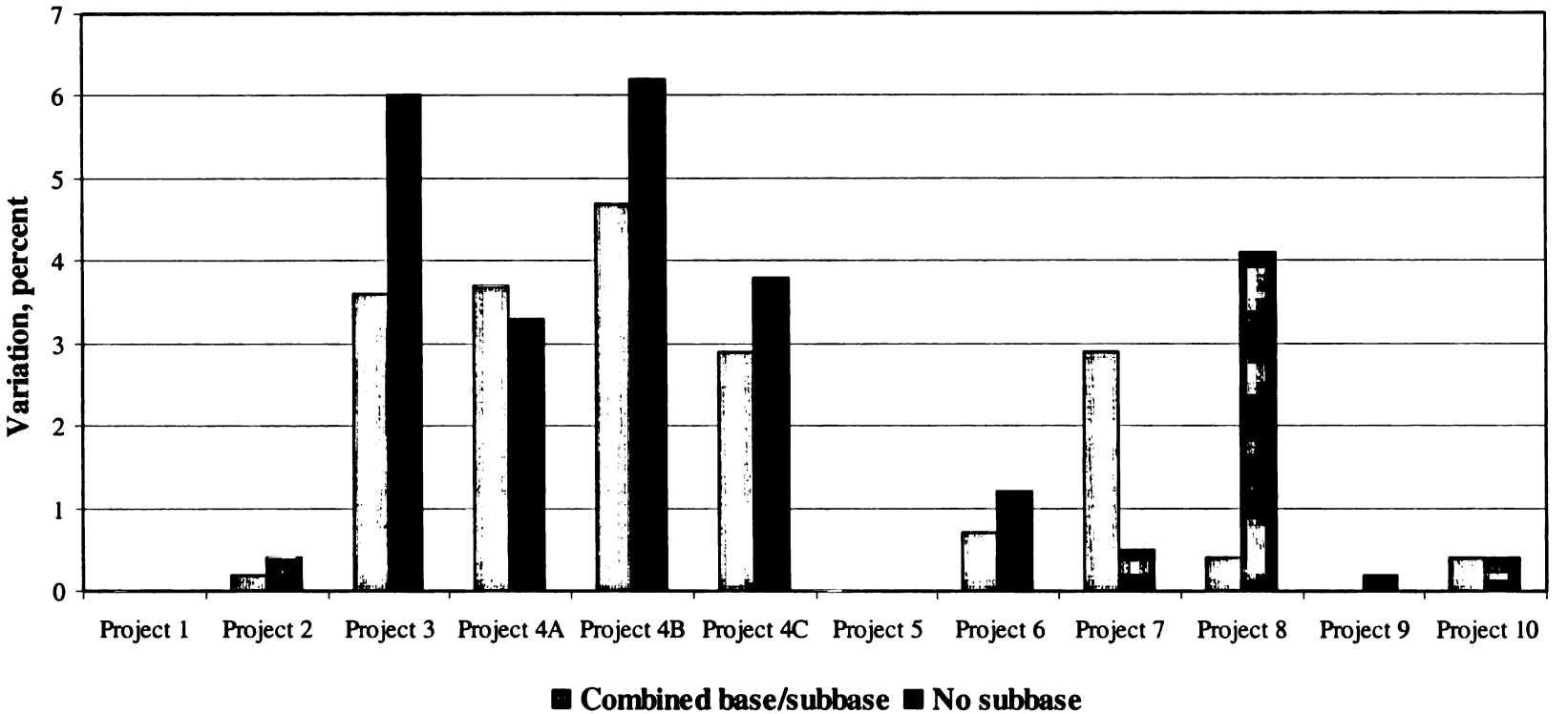

Figure 14: Comparison of variation in results for combined base/subbase and no subbase approaches

*Remarks: there is no subbase layer for projects 1 and 5

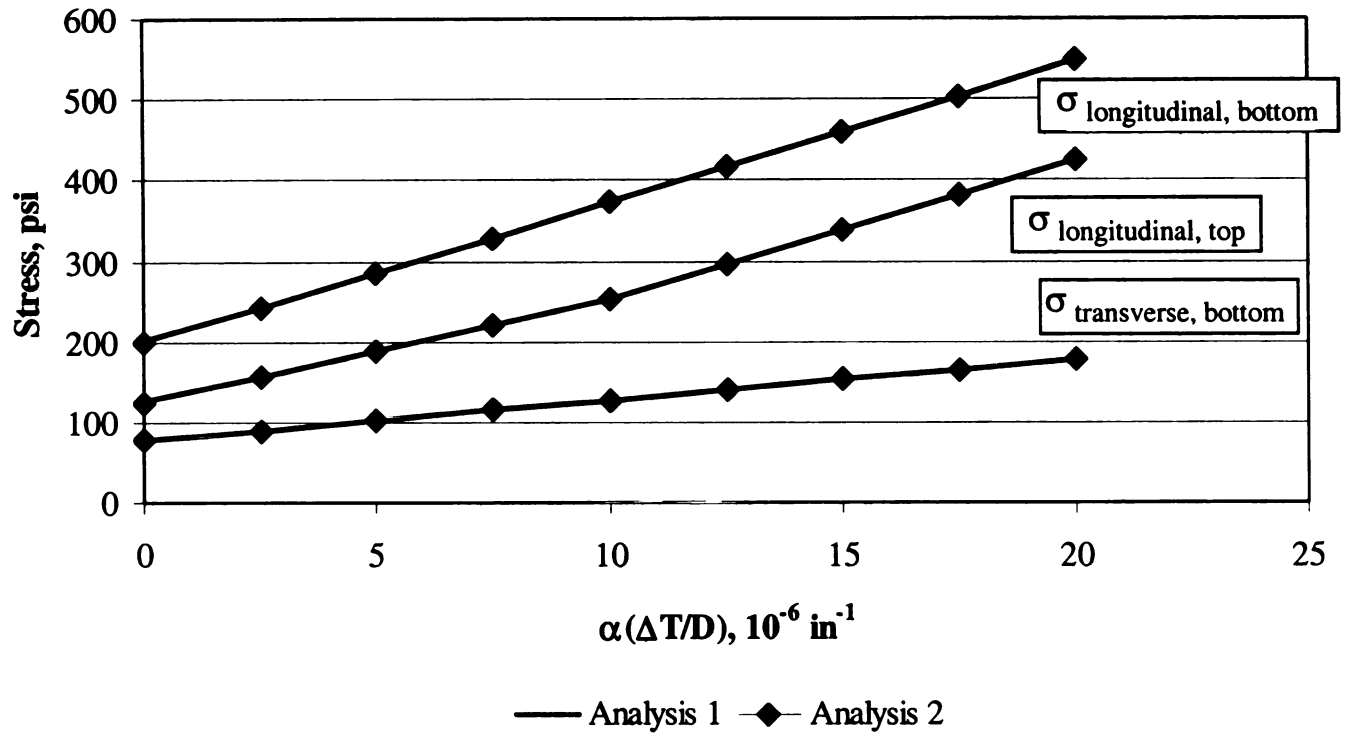

Figure 15: Combining CTE and thermal gradient

* Analysis 1: Constant temperature gradient (+2 ^{o}F/in.) with variation of CTE (0.1x10^{-6} to 10x10^{-6} in./in./^{o}F)

Analysis 2: Constant CTE (5x10^{-6} in./in./^{o}F) with variation of temperature gradient (0 to +4 ^{o}F/in.)

** Concrete shoulder, 10-in. slab, 16-in. base/subbase, 100-psi/in. k-value, single axle loading, 177-in. joint spacing

It was found that the mechanistic responses computed based on the two approaches are identical. A statistical experiment to illustrate the validity of combining CTE and thermal gradient was conducted by repeating this process for eight more combinations of pavement parameters selected based on a fractional factorial (Buch et al., 2004). It should be noted that comparison between pavements with different slab thickness even with the same thermal strain gradient is not valid, since the pavements are subjected to different temperature differentials. Comparison of pavement responses under a curled slab condition, therefore, should only be made within the same slab thickness.

Considering only frequently seen load configurations

Several axle and truck configurations are contained in the Truck driver's guidebook for Michigan (Michigan Center for Truck Safety, 2001). Based on the TAG's recommendations, certain axle and truck configurations, not existent or not frequently seen, could presumably be omitted. Only 8 axle configurations and 11 truck configurations are selected for the experimental matrix. Figures 16 (a) and (b) illustrate the axle and truck configurations included in the parametric study.

Axle Type	Axle Configuration
Single	
Tandem	
Tridem	
Quad	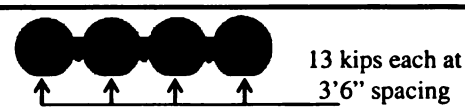
Group of 5	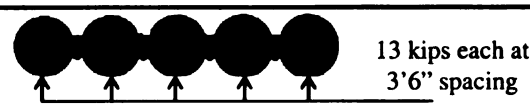
Group of 6	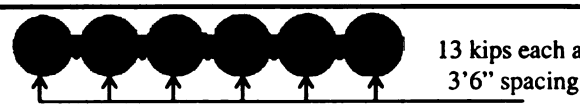
Group of 7	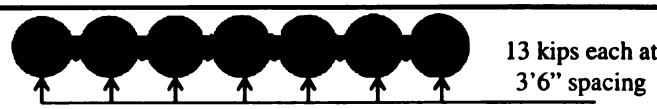
Group of 8	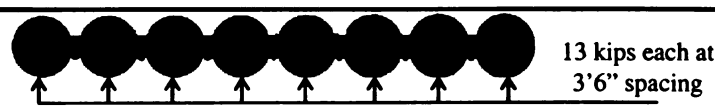

(a) Axle configurations

Figure 16: Load configurations considered in the study

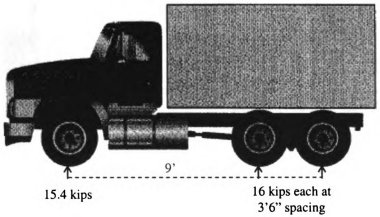

MI-2

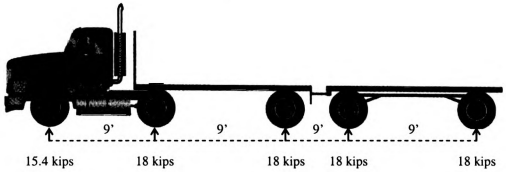

MI-7

(b) Truck configurations

Figure 16: Load configurations considered in the study (continued)

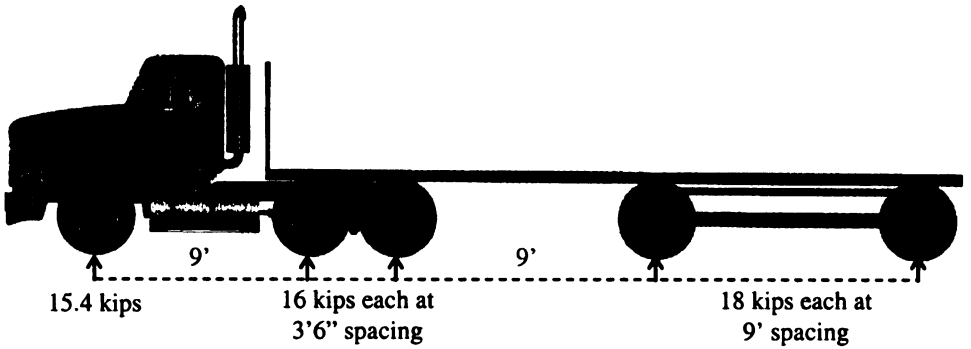

MI-8

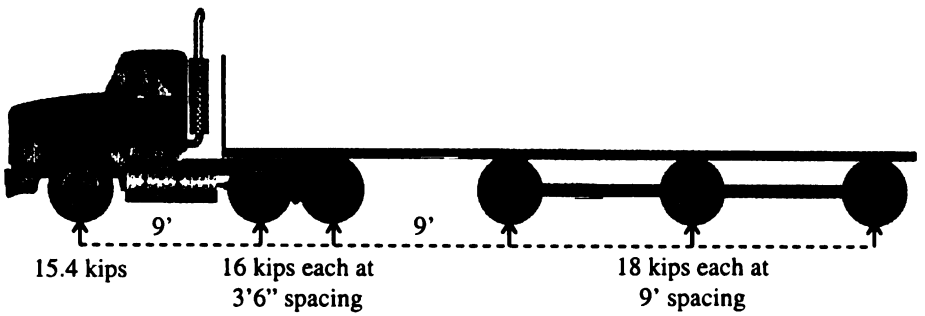

MI-9

(b) Truck configurations (continued)

Figure 16: Load configurations considered in the study (continued)

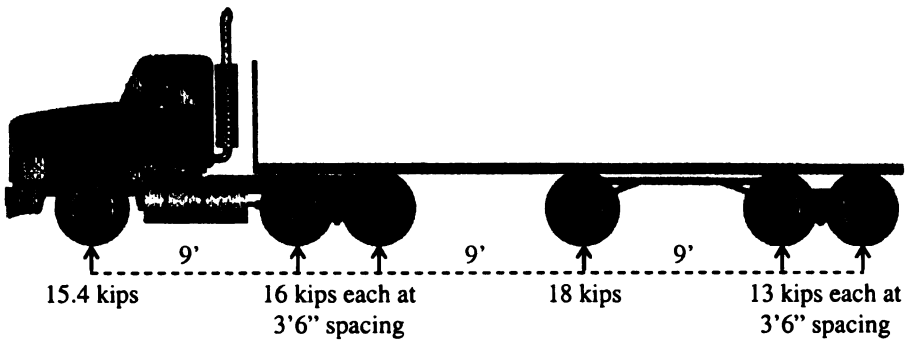

MI-11

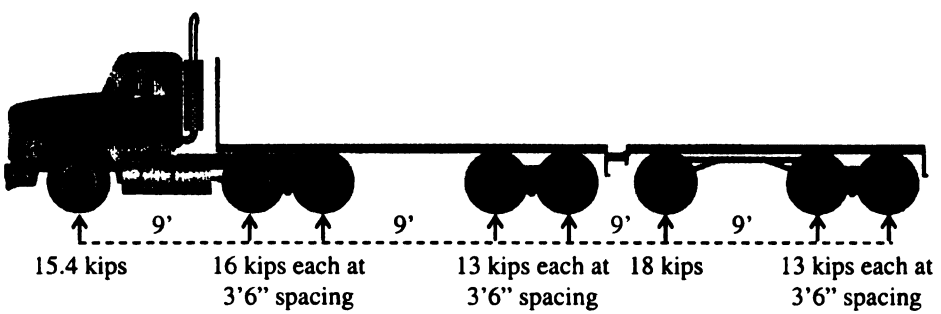

MI-12

(b) Truck configurations (continued)

Figure 16: Load configurations considered in the study (continued)

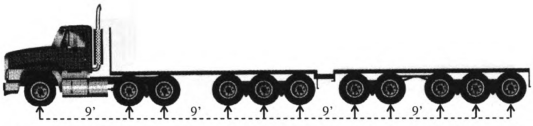

MI-13

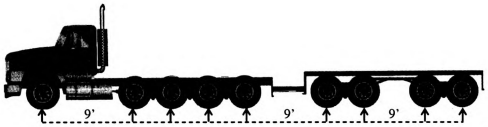

MI-16

(b) Truck configurations (continued)

Figure 16: Load configurations considered in the study (continued)

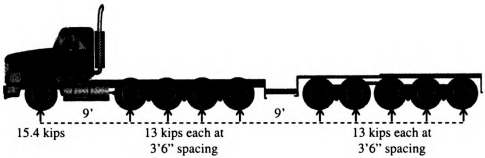

MI-17

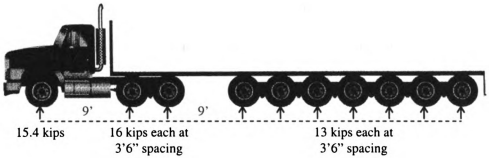

MI-19

(b) Truck configurations (continued)

Figure 16: Load configurations considered in the study (continued)

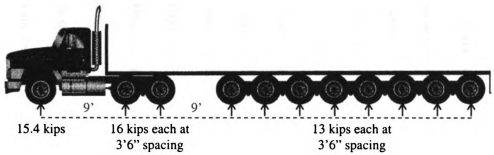

MI-20

(b) Truck configurations (continued)

Figure 16: Load configurations considered in the study (continued)

Adjusting increments for non-discrete inputs

Input increments need to be carefully considered for non-discrete variables; in this case, these included base/subbase thickness, modulus of subgrade reaction (k-value), and thermal strain gradient. The finer increments can better capture trends of the mechanistic responses, but will also result in increasing the required FE runs. Therefore, it is crucial to capture trends of the mechanistic responses with as large increments of input parameters as possible. Five values of each non-discrete variable were used in the sensitivity study of input increments. Based on this "mini-analysis", it was determined that response trends could be adequately captured by using three values for each non-discrete variable. These values for the base/subbase thickness, k-value, and thermal strain gradient are 4, 16, 26 in., 30, 100, 200 psi/in., and 0, ±10, $\pm 20 \times 10^{-6}$ $in.^{-1}$, respectively. Positive thermal gradients are considered for analysis of stresses at the bottom of the concrete slab, while negative thermal gradients are considered for analysis of stresses at the top of the concrete slab, since the critical stress locations correspond with the types of thermal gradient. Figures 17 through 19 illustrate the trends of stresses with variations of base/subbase thickness, modulus of subgrade reaction, and thermal strain gradient, respectively. Note that if not specified, the parameters for these sensitivity plots are 10-in. concrete slab, 16-in. base/subbase, 100-psi/in. modulus of subgrade reaction, concrete shoulder, 177-in. joint spacing, 18-kips single axle, and thermal strain gradient of zero.

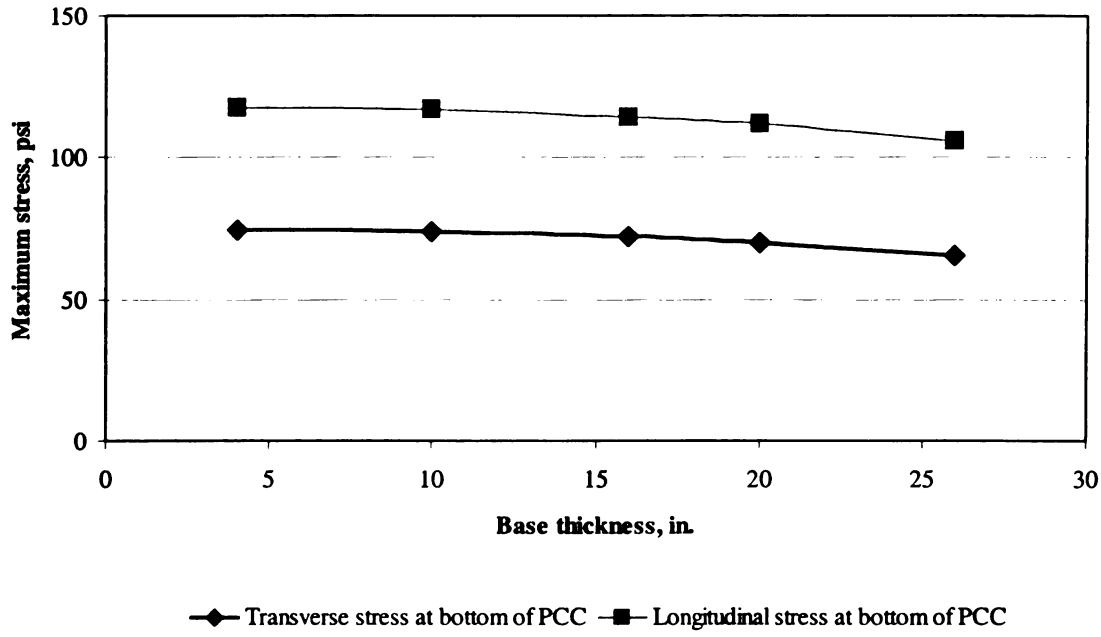

Figure 17: Sensitivity trend due to the variation in base/subbase thickness

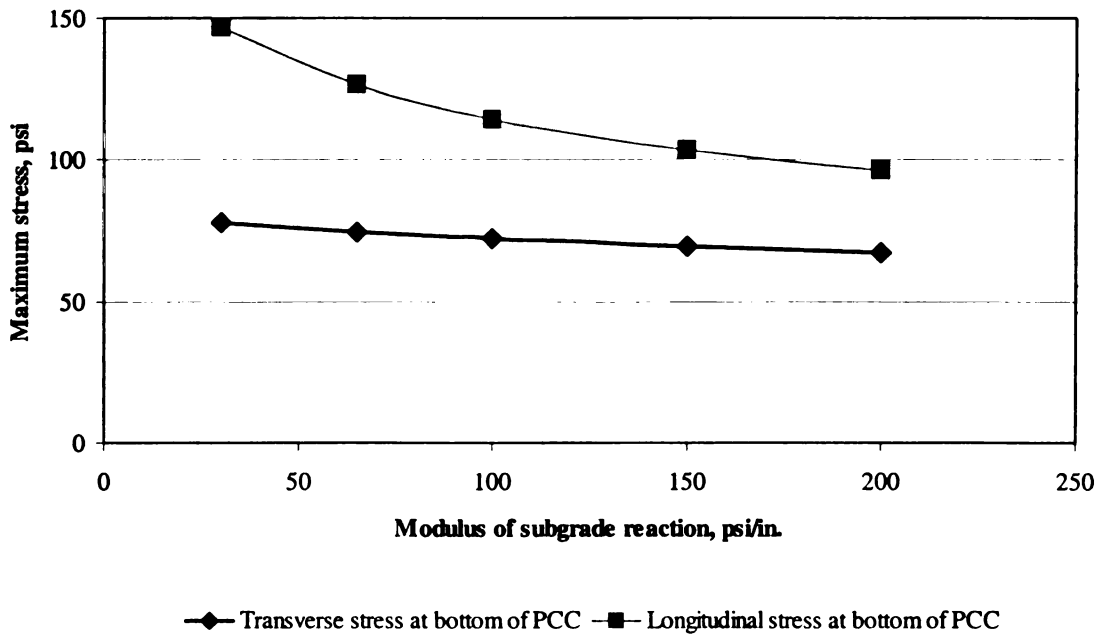

Figure 18: Sensitivity trend due to the variation in modulus of subgrade reaction

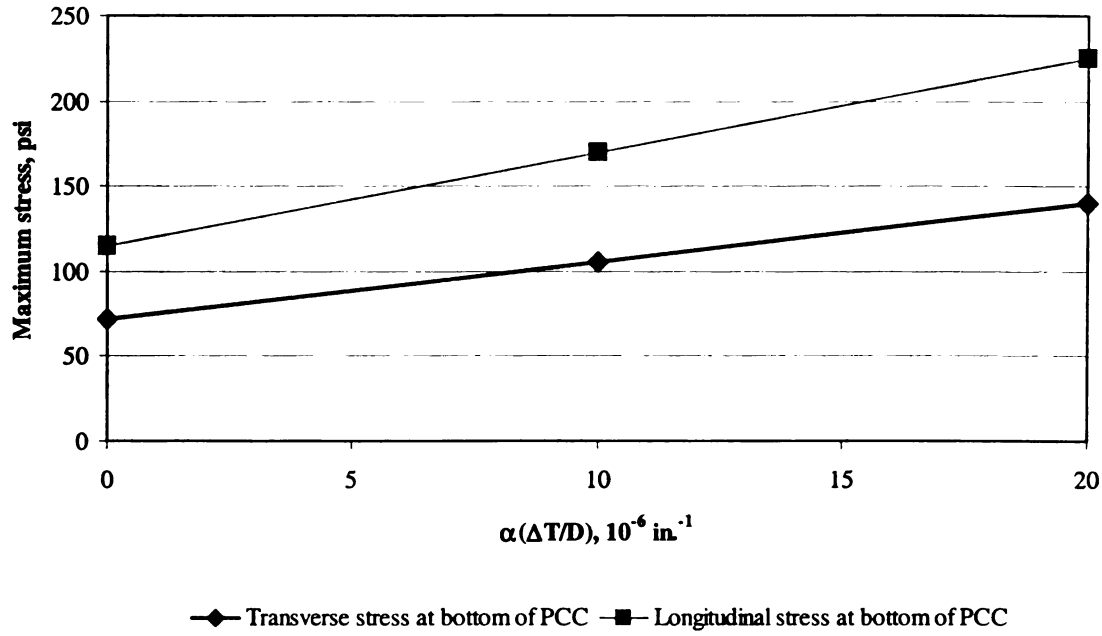

Figure 19: Sensitivity trend due to the variation in thermal strain gradient

In addition to the above mentioned strategies, locations of stresses (at the bottom and the top of the concrete slab) are also effectively selected to reduce the number of runs. For positive thermal gradients, only stresses at the bottom of the concrete slab are considered, while stresses at the top of the concrete slab are considered for negative thermal gradients. The experimental matrix size has been reduced to 43,092 FE runs as illustrated in Table 3. It should be noted that this final experimental matrix addresses all possible input parameters for all discrete variables and three levels of each non-discrete variable. However, the combinations of non-discrete variables that are not addressed in this final experimental matrix are still of interest and will be obtained through the interpolation scheme, which is to be discussed later.

Table 3: Final experimental matrix

Input variables	Number of cases
PCC slab thickness	7 (6, 7,... 12 in.)
Base/subbase thickness	3 (4, 16, 26 in.)
Modulus of subgrade reaction	3 (30, ,100, 200 psi/in.)
Slab length (joint spacing)	2 (177 in. and 315 in.)
Joint design	1
Shoulder type	3
$\alpha.\Delta T/D$	3 (0, ±10, ±20x10^{-6} in^{-1})
Location of stress	2
Load configuration	19
Total combinations	43,092

3.3 Analysis process

Based on a complete factorial of 43,092 combinations of parameters identified previously, a preliminary parametric study is conducted by performing a series of FE analyses using the ISLAB2000 program. The results obtained from this parametric study are included in this section. The parametric study will be presented in four parts: structural model, analysis process, documentation of analysis results and interpretation of analysis results.

The pavement system for this analysis typically is comprised of three to six concrete slabs, depending on the length of the load configuration. This is to ensure that the first and last concrete slabs are unloaded as recommended in Report 1-26 (NCHRP, 1990) to analyze the pavement system with extended slabs in order to reflect realistic boundary conditions that all the slabs are bounded by two slabs on both directions. Two lane widths (12 and 14 ft) and two shoulder types (untied AC and tied concrete) are considered. The study focuses on the analysis of the mechanistic responses in the outer lane (the truck lane), which is traditionally the design lane. Two joint spacing lengths

(177 and 315 in.) are considered. The structural model with two traffic lanes was not found to result in different pavement response in the outer wheel path as compared to the results obtained from the structural model with one traffic lane. Therefore, the second traffic lane is not included in the structural model to reduce the structure size and, consequently, analysis time. The wheel path considered in this study is 20 in. from the center of the outer wheel to the traffic stripe, similar to the pavement model used by Darter et al, 1994. Mesh size of 12x12 in. is used as a standard mesh size. This mesh size was found to achieve both satisfactory convergence and reasonable runtime. Figure 20 illustrates the typical slab structure layout as modeled using ISLAB2000.

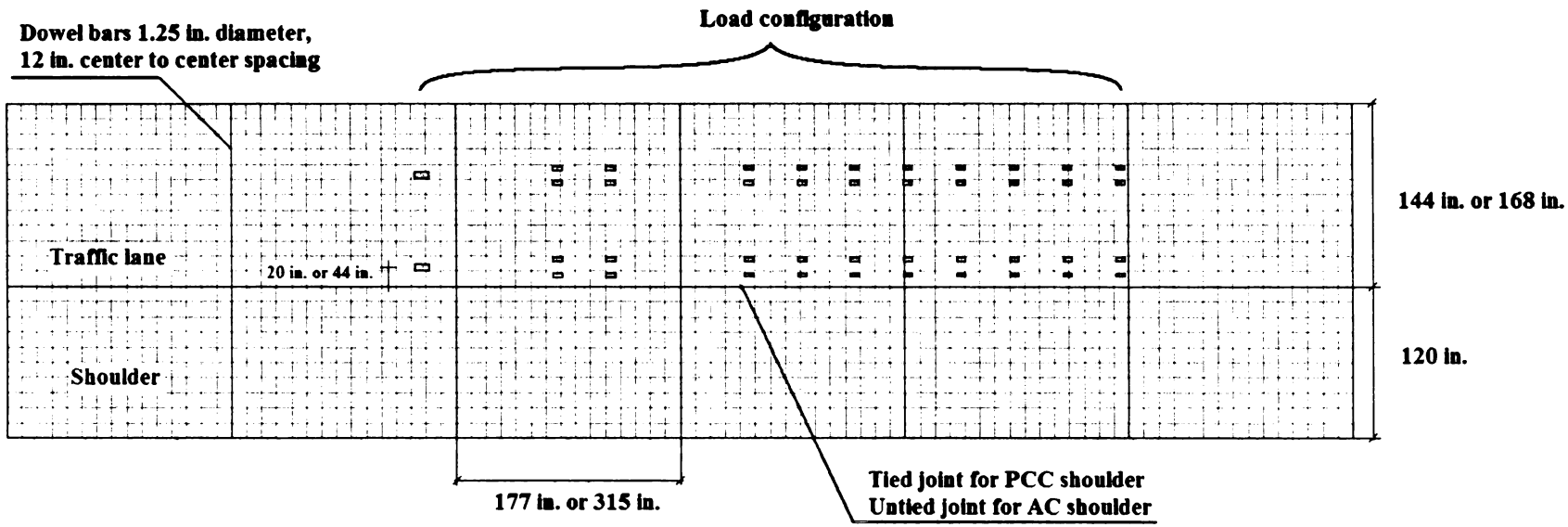

Figure 20: Overview of structural model

The flow chart in Figure 21 illustrates the required components for the FE analysis. It can be seen that all structural and environmental factors have been addressed in the final experimental matrix. However, the critical load location needs to be derived first before the creation of the stress catalog. The critical load location is defined by the load location along the wheel path that results in the most critical mechanistic response, the highest value of the maximum responses for each load location.

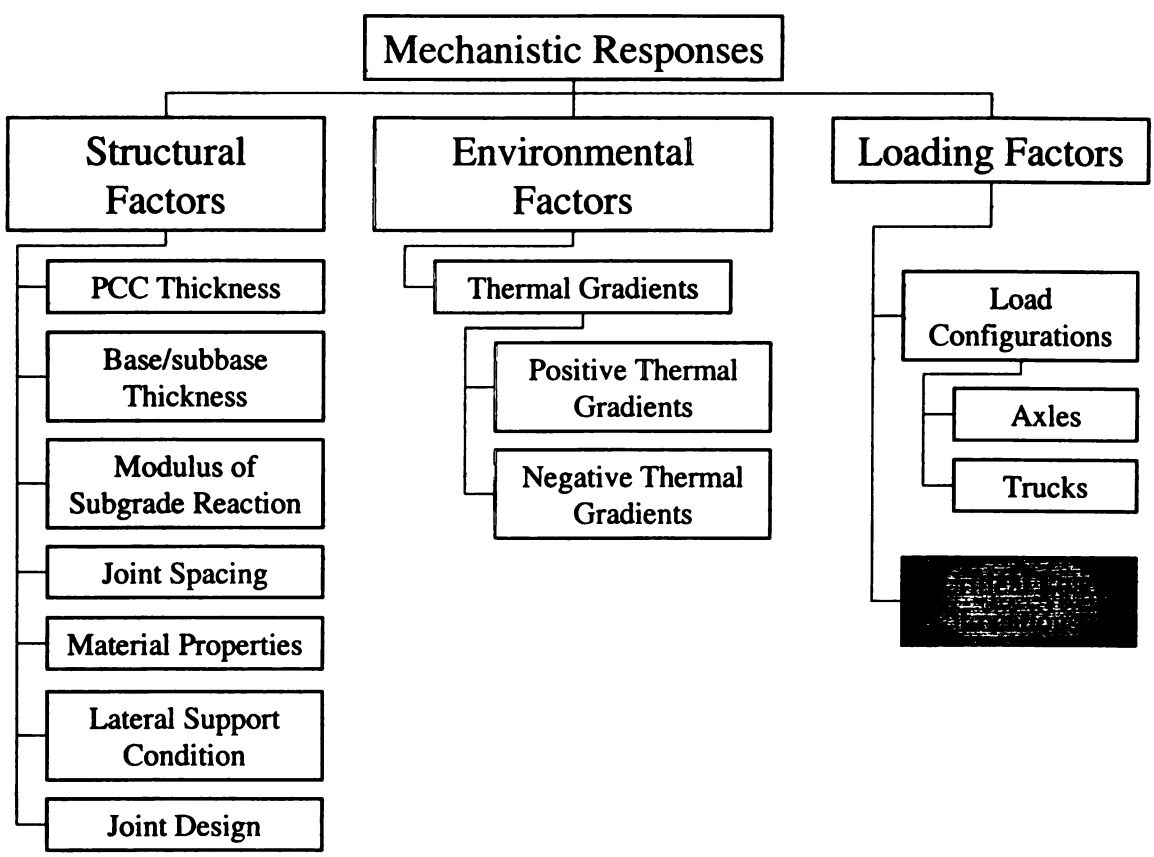

Figure 21: Required components for the analytical tool

Procedure of determining critical load location

The procedure for determining critical load location is illustrated in Figure 22. The procedure involves the computation of stresses at every load location along the wheel path for a given set of conditions. The load location that results in the most critical (maximum) stress will be considered as the critical load location.

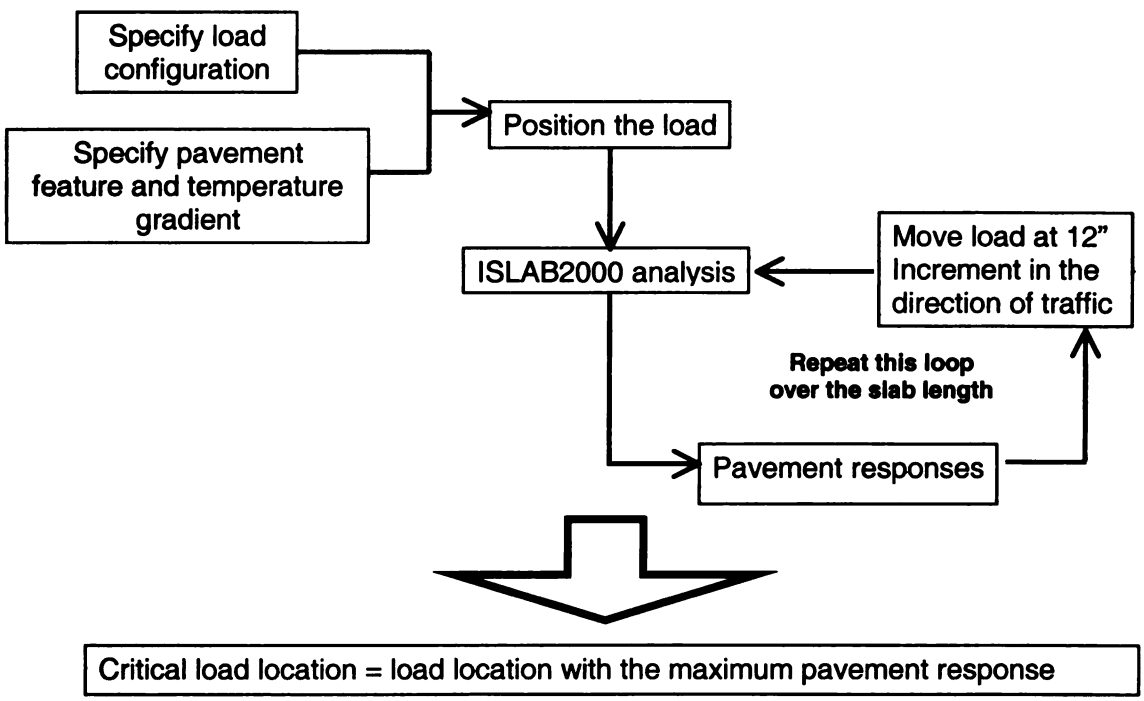

Figure 22: Procedure of determining critical load location

Assumptions and validation process

The procedure for determining critical load location is a time consuming process; it is impractical to perform the procedure for all possible combinations of input parameters in the final experimental matrix. It was assumed that variations in the following variables do not affect critical load locations:

- Slab thickness,
- Base/subbase thickness,
- k-value,
- Lateral support condition and
- Thermal strain gradient.

Validation of these assumptions was conducted to show that the critical load location is constant with the variation of the five non-influential variables. The fractional factorial design of $\frac{1}{3^3} \cdot 3^5 = 9$ is the method used to study the impact of variables within a practical size of validation matrix. The validation matrix used for all trucks and axles is summarized in Table 4. Fundamentally, fractional factorial design is a statistical method that allows for fractionation of a complete experimental factorial, while still balancing the fraction.

This process needs to be repeated for every axle and truck configuration, joint spacing, and stress location (top and bottom of the concrete slab) as these factors are considered influential in affecting critical load locations. Critical load locations for all eight axle configurations and 11 truck configurations are summarized in Table 5. Critical load locations for axle configurations were found to be in the vicinity of the middle of the slab and the transverse joint for stresses at the bottom and top of the concrete slab, respectively. However, no typical location was found for critical load locations for truck configurations due to the complex combinations of the axles and axle spacing lengths within truck configurations.

Table 4: Validation matrix

Validation case	Lateral support condition	Slab thickness (in.)	Base/subbase thickness (in.)	Modulus of subgrade reaction (psi/in.)	Thermal strain gradient (10^{-6} in.$^{-1}$)
1	12-ft lane width with tied concrete shoulder	10	16	100	10
2	12-ft lane width with untied asphalt shoulder	10	26	30	5
3	14-ft lane width with untied asphalt shoulder	10	4	200	15
4	12-ft lane width with tied concrete shoulder	12	26	200	10
5	12-ft lane width with untied asphalt shoulder	12	4	100	5
6	14-ft lane width with untied asphalt shoulder	12	16	30	15
7	12-ft lane width with tied concrete shoulder	8	4	30	10
8	12-ft lane width with untied asphalt shoulder	8	16	100	5
9	14-ft lane width with untied asphalt shoulder	8	26	100	15

(a) Physical meaning of determined critical load location

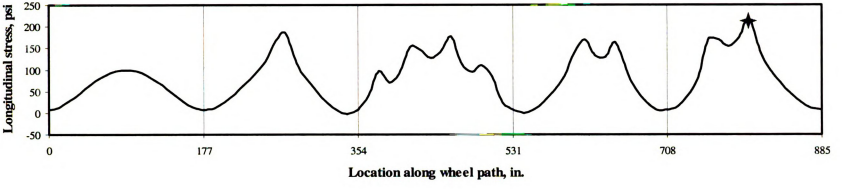

(b) Longitudinal stress profile and location of critical stress at critical load location for validation case 1

Figure 23: Validation and determination of critical load location

This example shows the determination process of the critical load location for bottom-up stresses for MI-16 on 177-in. joint spacing pavements. Stresses were computed for load locations along the wheel path for the nine validation cases as identified in Table 4. The non-influential variables were found to impact the stress magnitude; however, the non-influential variables did not significantly impact critical load location. For this example, the critical load location was approximately 84 in. for all the nine cases irrespective of the variation of the non-influential factors. Figure 23 (a) illustrates the physical meaning of the computed critical location. An example stress profile for validation case 1 and the corresponding critical stress location are illustrated in Figure 23 (b). More example illustrations can be seen in Figures 24 and 25.

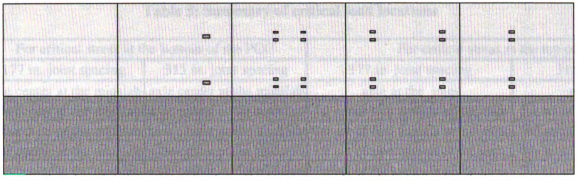

Figure 24: Example validation and determination (bottom stresses, MI-9, 177-in. joint spacing)

Figure 25: Example validation and determination (bottom stresses, MI-20, 177-in. joint spacing)

Table 5: Summary of critical load locations

Load configuration	For critical stress at the bottom of the PCC		For critical stress at the top of the PCC	
	177 in. joint spacing	315 in. joint spacing	177 in. joint spacing	315 in. joint spacing
Single axle	axle center at the midslab	axle center at the midslab	axle at the joint	axle at the joint
Tandem axle	axle center at the midslab	axle center at the midslab	1st set of two wheels at the joint	1st set of two wheels at the joint
Tridem axle	axle center at the midslab	axle center at the midslab	1st set of two wheels at the joint	3rd set of two wheels at the joint
Quad axle	axle center at the midslab	axle center at the midslab	1st set of two wheels at the joint	4th set of two wheels at the joint
Multi-axle 5	axle center at the midslab	axle center at the midslab	1st set of two wheels at the joint	5th set of two wheels at the joint
Multi-axle 6	axle center at the midslab	axle center at the midslab	1st set of two wheels at the joint	6th set of two wheels at the joint
Multi-axle 7	axle center at the midslab	axle center at the midslab	1st set of two wheels at the joint	7th set of two wheels at the joint
Multi-axle 8	axle center at the midslab	axle center at the midslab	1st set of two wheels at the joint	8th set of two wheels at the joint
MI-2	108 in. from the joint	48 in. from the joint	24 in. from the joint	240 in. from the joint
MI-7	at the joint	36 in. from the joint	96 in. from the joint	192 in. from the joint
MI-8	60 in. from the joint	96 in. from the joint	60 in. from the joint	264 in. from the joint
MI-9	132 in. from the joint	at the joint	60 in. from the joint	264 in. from the joint
MI-11	144 in. from the joint	36 in. from the joint	60 in. from the joint	264 in. from the joint
MI-12	144 in. from the joint	48 in. from the joint	48 in. from the joint	264 in. from the joint
MI-13	144 in. from the joint	156 in. from the joint	48 in. from the joint	264 in. from the joint
MI-16	84 in. from the joint	252 in. from the joint	156 in. from the joint	180 in. from the joint
MI-17	72 in. from the joint	156 in. from the joint	144 in. from the joint	180 in. from the joint
MI-19	144 in. from the joint	36 in. from the joint	48 in. from the joint	276 in. from the joint
MI-20	144 in. from the joint	36 in. from the joint	48 in. from the joint	252 in. from the joint

3.4 Documentation of analysis results

The parametric study results provide information used in investigating the impact of structural, environmental, and loading factors, and the interaction between them on three types of mechanistic responses: longitudinal stress at the bottom of the concrete slab, transverse stress at the bottom of the concrete slab, and longitudinal stress at the top of the concrete slab.

Impact of structural factors

Figures 26 (a) through (f) are example illustrations of the impact of structural features on the longitudinal stress at the bottom of the concrete slab under various conditions as stated in the figures. Note that these figures represent MI-16 loading (see Figure 26 (c) for configuration), 16-in. base/subbase, 100-psi/in. k-value, concrete shoulder, and 177-in. joint spacing unless identified otherwise. All the figures show that slab thickness has a significant impact in reducing stresses. In addition, the figures show that the changes in stresses due to changes in base/subbase thickness, k-value, and lateral support condition appear to be less relevant as the concrete slab becomes thicker. Also, joint spacing does not appear to have significant impact on edge stresses. Impact of lateral support condition will be discussed in detail later. Figures 26 (d) and (f) show an interaction of k-value and joint spacing with thermal gradients, which is to be discussed later. Although the magnitude of longitudinal stress at the bottom of the concrete slab was found to vary with combinations of input parameters, similar trends were observed in sensitivity plots over the entire experimental matrix. Similar trends were observed for the transverse stress at the bottom of the concrete slab with the exception of the impact of joint spacing, which

was found to have no significant impact on the transverse stresses, even under the influence of a thermal gradient. An example critical location of stress is illustrated in Figure 26 (g).

The impact of structural features on longitudinal stress at the top of the concrete slab is illustrated in Figures 27 (a) through (f). Note that these figures represent MI-16 loading (see Figure 16 (b) for configuration), 16-in. base/subbase, 100-psi/in. k-value, concrete shoulder, and 177-in. joint spacing, the same conditions as previous parts unless identified otherwise. It can be seen in these figures that the magnitudes of longitudinal stresses at the top of the concrete slab are lower than the longitudinal stresses at the bottom of the concrete slab illustrated in the previous part. However, the trends observed for these stresses are similar. It should be noted that negative thermal gradients are considered in Figures 27 (d) and (f), since the critical location of stresses is at the top of the concrete slab in these figures. An example critical location of stress is illustrated in Figure 27 (g).

Impact of loading factors

Figures 26 (h) and 27 (h) are example illustrations of the impact of the load configurations (axles and trucks) on the magnitude and normalized magnitude (by total weight of the configuration) of longitudinal stresses at the bottom and top of the concrete slab, respectively. In order to compare the contribution of each axle type (carrying different weight) on loading stress, it is necessary to express the stress as psi/kip. It can be seen that the normalized stress magnitudes are lower as the axle configurations have more load carrying wheels, implying that at the same stress level, a multi-axle can carry

heavier loads than a single or tandem axle. However, the impact of truck configurations is not shown in these figures because each truck configuration makes various numbers of passes at the point of interest on the pavement slab. For example, the truck type MI-16 (see Figure 16 (b)) will result in four peaks of stresses corresponding to one single axle (driving axle), one quad axle, and two tandem axles. Hence, normalization based on total weight is not valid. The normalization should be based on the number of passes made by each axle group.

Impact of load lateral placement on mechanistic responses presented in Figure 28 (a), in which stresses are shown for several load locations across the lane width, suggests that the concrete shoulder resulted in the lowest stresses among the three lateral support conditions considered in the study for the load located along the wheel path. It was found that the magnitudes of longitudinal stresses for AC shoulder (12-ft lane with AC shoulder) were higher than that for widened lane (also AC shoulder but with 14-ft lane). This could be attributed to the fact that a widened lane (14 ft.) creates a pseudo-interior loading condition (the wheel path shifted 2 ft towards the centerline, resulting in the reduction of stresses from edge loading). An example sensitivity plot of temperature-induced stresses in Figure 28 (b) illustrates that lateral support condition does not have a significant impact on temperature-induced stress in longitudinal direction.

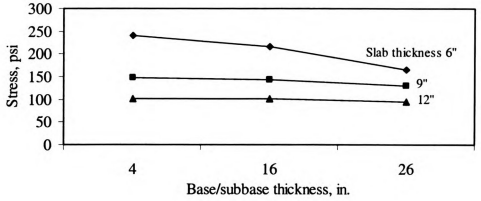

(a) Impact of base/subbase thickness, thermal strain gradient of $0x10^{-6}$ in.$^{-1}$

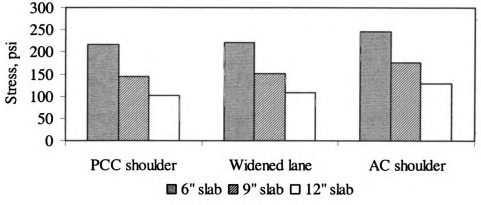

(b) Impact of lateral support condition, thermal strain gradient of $0x10^{-6}$ in.$^{-1}$

Figure 26: Example sensitivity plots of bottom-up stresses

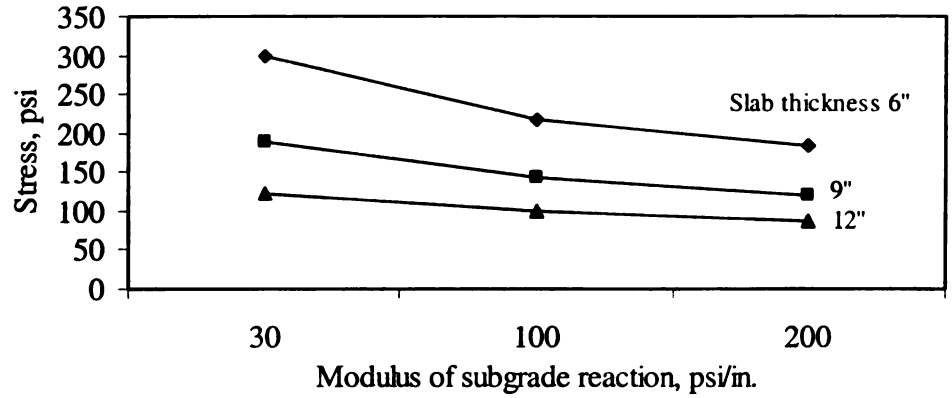

(c) Impact of modulus of subgrade reaction, thermal strain gradient of 0x10^{-6} in.$^{-1}$

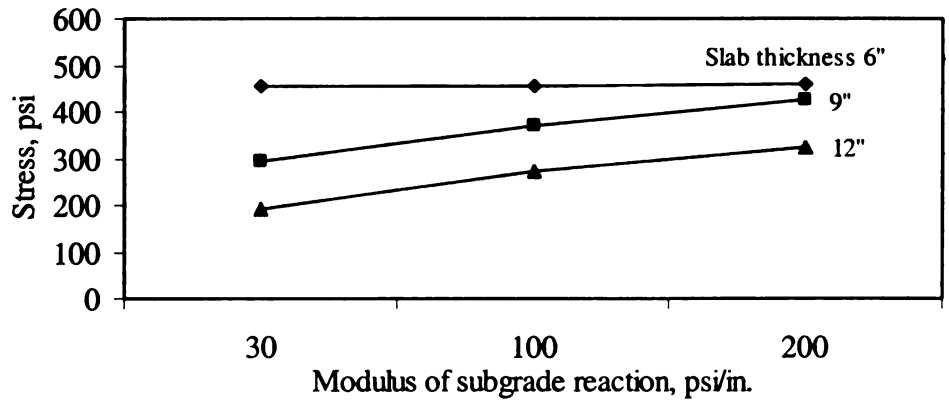

(d) Impact of modulus of subgrade reaction, thermal strain gradient of 20x10^{-6} in.$^{-1}$

Figure 26: Example sensitivity plots of bottom-up stresses (continued)

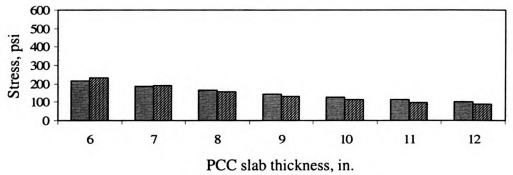

(e) Impact of joint spacing, thermal strain gradient of $0x10^{-6}$ $in.^{-1}$

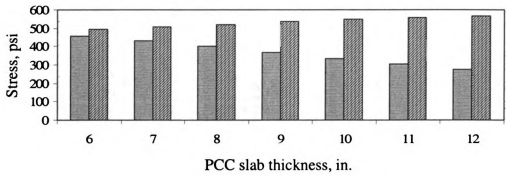

(f) Impact of joint spacing, thermal strain gradient of $+20x10^{-6}$ $in.^{-1}$

Figure 26: Example sensitivity plots of bottom-up stresses (continued)

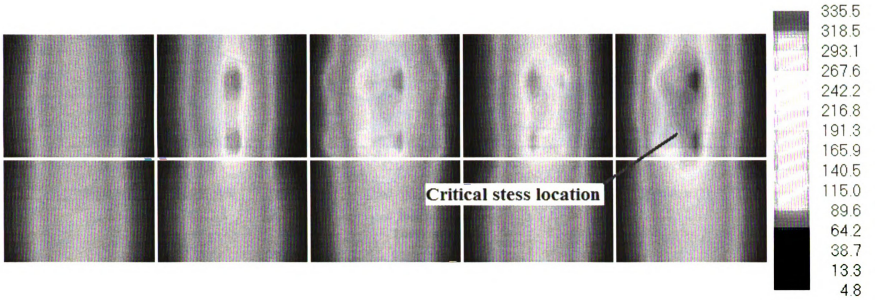

(g) Stress contour for 10-in. concrete slab, thermal strain gradient of +20x10^{-6} in.$^{-1}$

Figure 26: Example sensitivity plots of bottom-up stresses (continued)

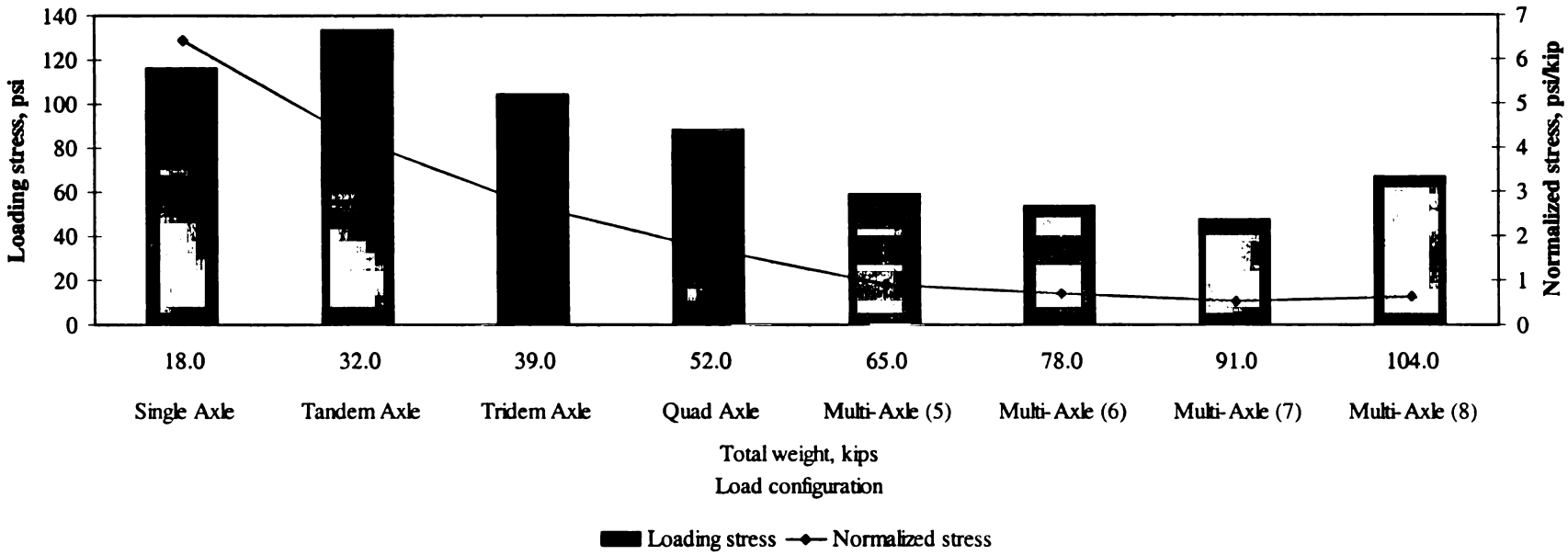

(h) 10-in. concrete slab, thermal strain gradient of $0x10^{-6}$ $in.^{-1}$

Figure 26: Example sensitivity plots of bottom-up stresses (continued)

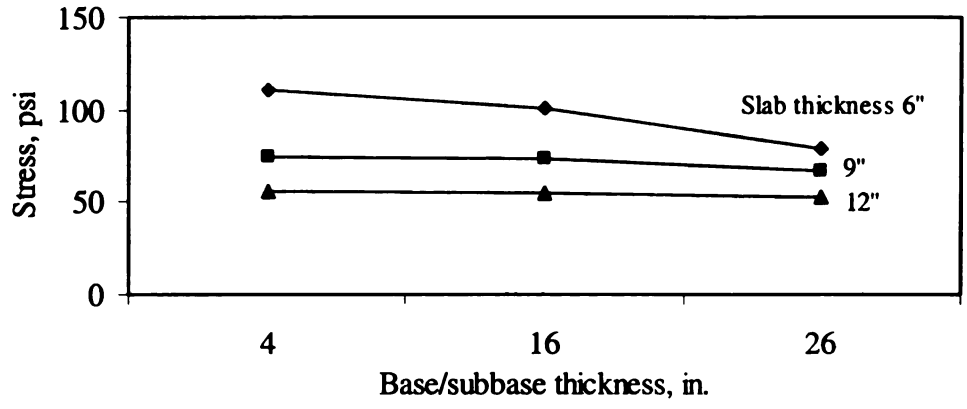

(a) Impact of base/subbase thickness, thermal strain gradient of $0x10^{-6}$ $in.^{-1}$

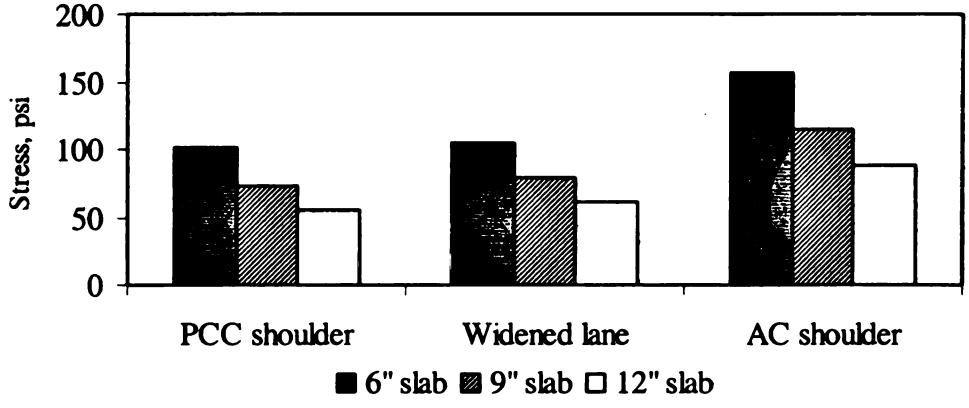

(b) Impact of lateral support condition, thermal strain gradient of $0x10^{-6}$ $in.^{-1}$

Figure 27: Example sensitivity plots of top-down stresses

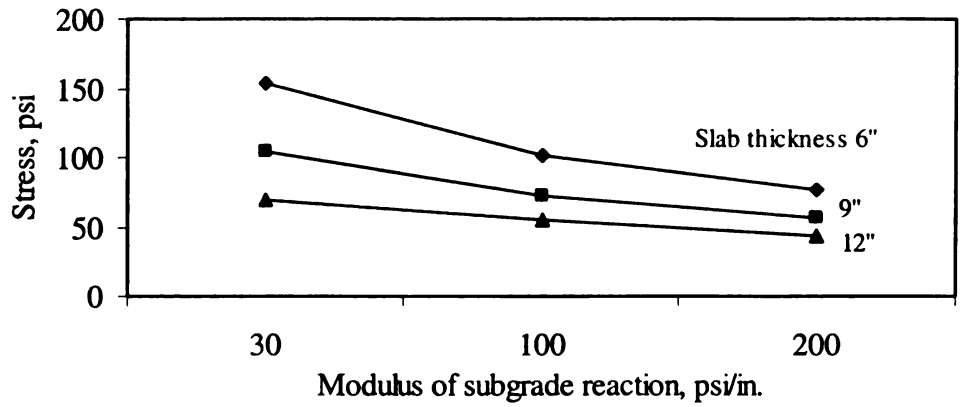

(c) Impact of modulus of subgrade reaction, thermal strain gradient of $0x10^{-6}$ $in.^{-1}$

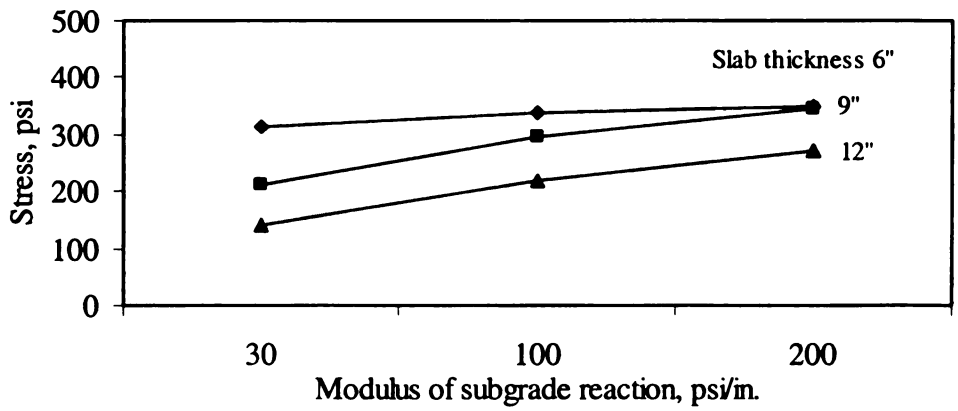

(d) Impact of modulus of subgrade reaction, thermal strain gradient of $20x10^{-6}$ $in.^{-1}$

Figure 27: Example sensitivity plots of top-down stresses (continued)

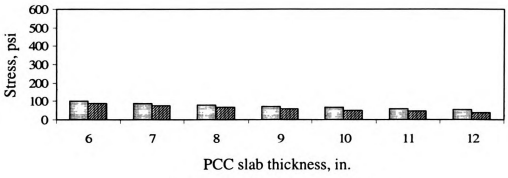

(e) Impact of joint spacing, thermal strain gradient of $0x10^{-6}$ $in.^{-1}$

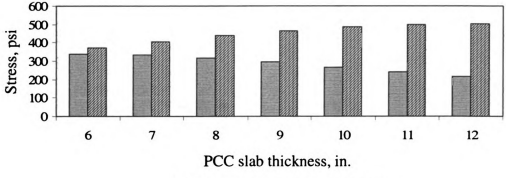

(f) Impact of joint spacing, thermal strain gradient of $20x10^{-6}$ $in.^{-1}$

Figure 27: Example sensitivity plots of top-down stresses (continued)

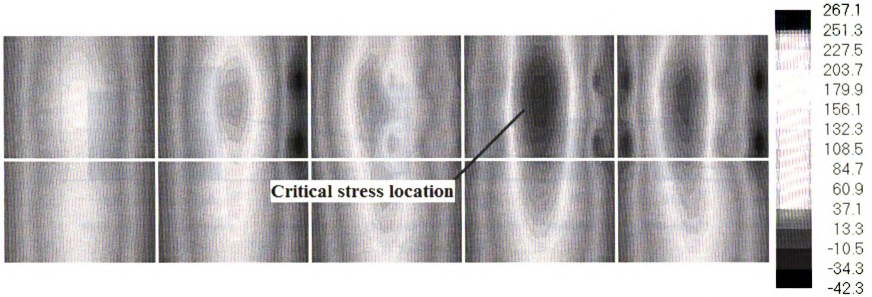

(g) Stress contour for 10-in. concrete slab, thermal strain gradient of -20x10^{-6} in.$^{-1}$

Figure 27: Example sensitivity plots of top-down stresses (continued)

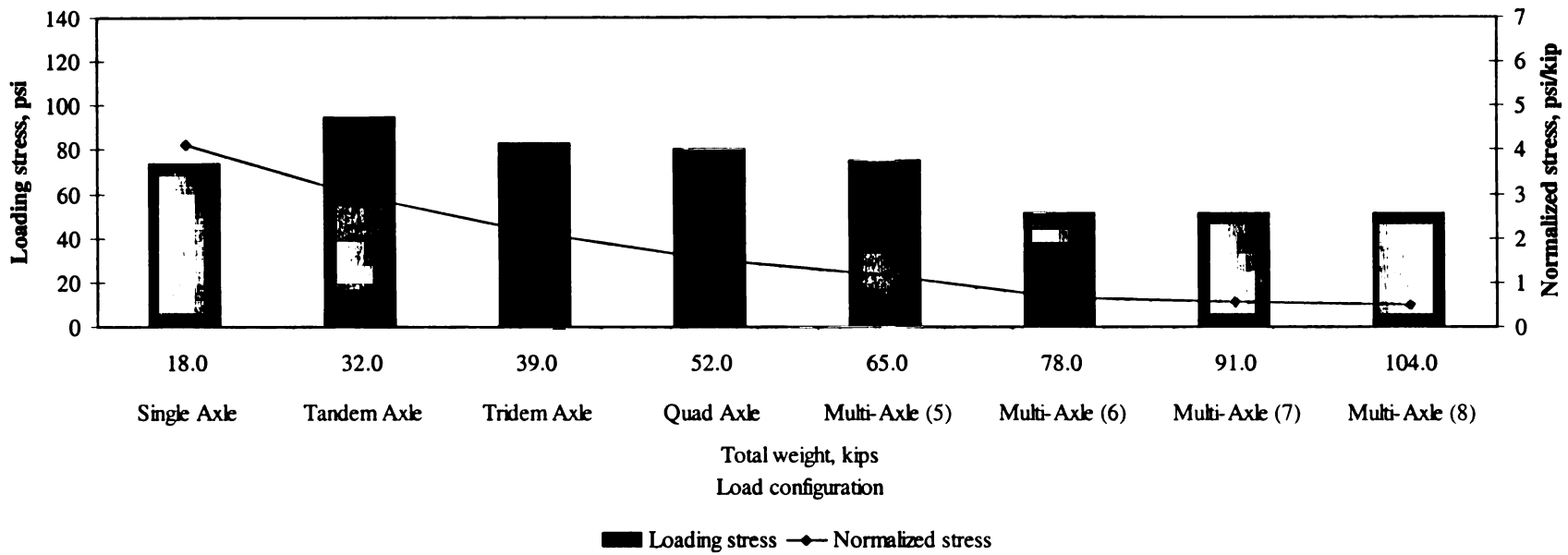

(h) 10-in. concrete slab, thermal strain gradient of $0x10^{-6}$ $in.^{-1}$

Figure 27: Example sensitivity plots of top-down stresses (continued)

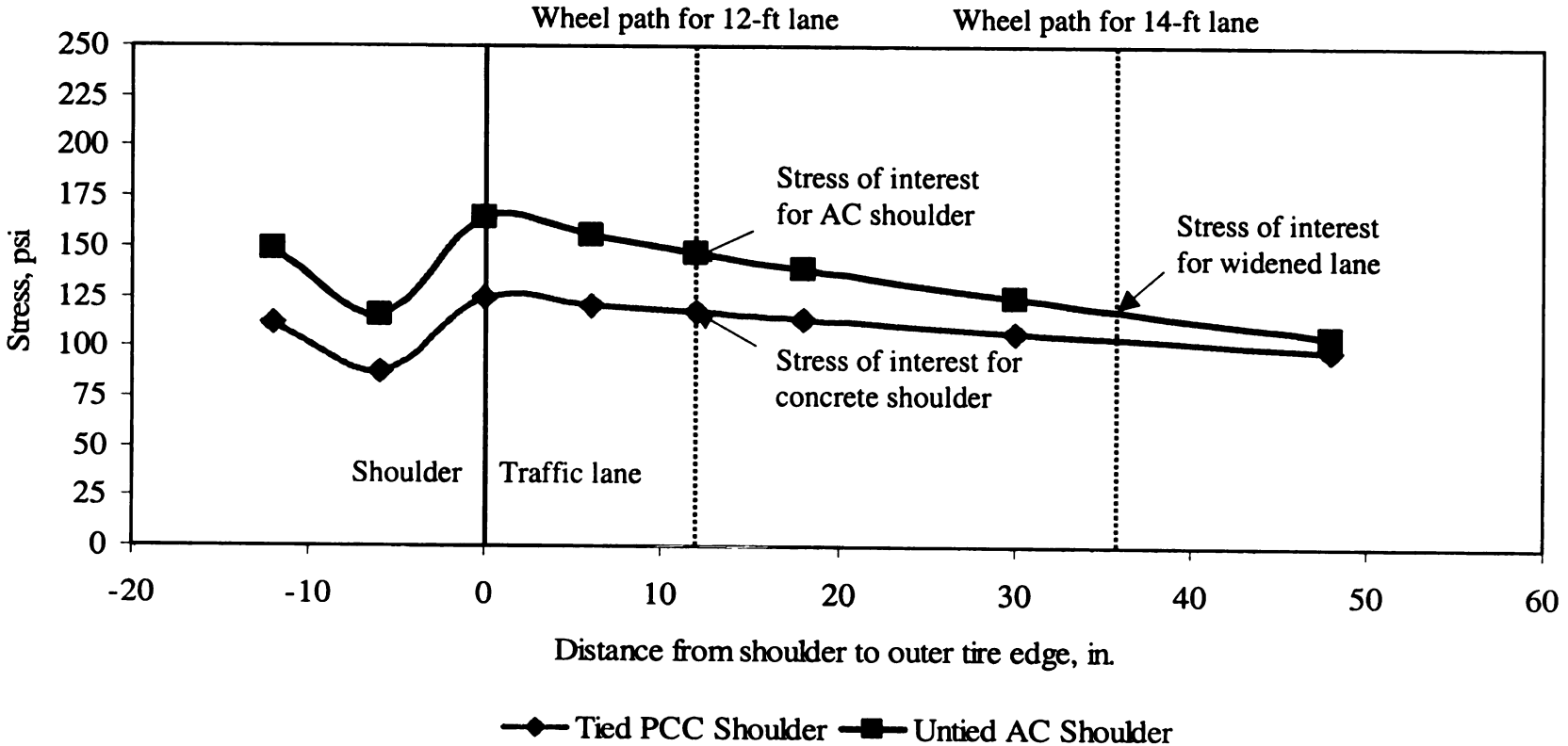

(a) Effect of load lateral placement on different lateral support conditions

Figure 28: Impact of lateral support condition

Remarks: Longitudinal stresses at the bottom of the concrete slab, 10-in. slab thickness, 16-in. base/subbase thickness, 100-psi/in. k-value, single axle, zero thermal strain gradient)

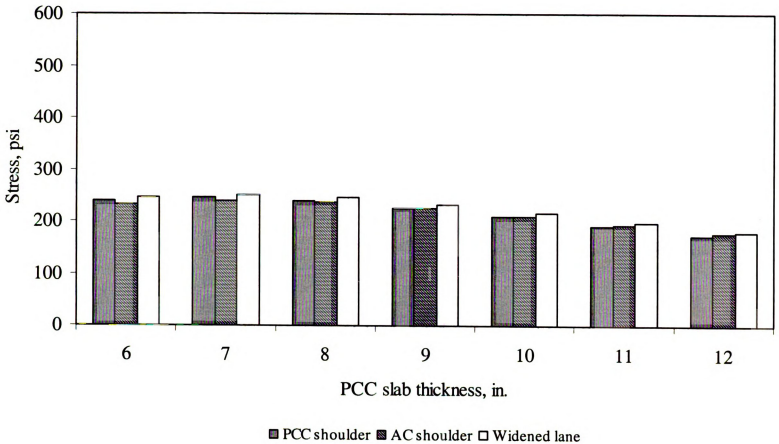

(b) Longitudinal temperature stress at the bottom of the slab

Figure 28: Impact of lateral support condition (continued)

Impact of environmental factors

Environmental factors in this study are addressed in terms of thermal strain gradient (the product of CTE with positive or negative thermal gradients). As illustrated in Figures 29 (a) and (b), a positive gradient causes a downward curling of the slab, while a negative gradient causes an upward curling of the slab. The increase in magnitude of thermal gradient results in the increase in the magnitude of stresses, when positive and negative thermal gradients are considered in computation of stresses at the bottom and top of the concrete slab, respectively.

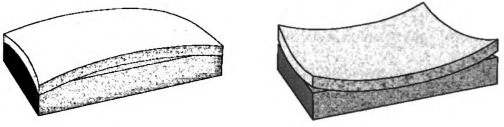

(a) Downward curling **(b) Upward curling**

Figure 29: Slab curling due to different types of thermal gradients (Yu et al, 2004)

As observed in the previous section (Figures 26 (d) and 27 (d)), the magnitude of the longitudinal stress appears to be impacted by the interaction between the thermal strain gradients, k-value and pavement thickness. This interactive trend is supported by the curling stress equations by Bradbury (Huang, 1993), where thermal curling stress is a function of the finite slab correction factor. This factor generally increases with the increase in the ratio of joint spacing (for longitudinal stresses) to radius of relative stiffness. This phenomenon could also be explained by

Significance of parametric study results

Based on the parametric study results, the insight into the impact of the interaction between various parameters on pavement stresses was established. Understanding the mechanistic behavior of the pavement provides an indirect connection to a better comprehension of pavement performance. From the mechanistic standpoint, the results suggest various types of interactions in that several parameters were found to affect pavement stresses. These effects include i) the interactive effect between slab thickness and base/subbase thickness on loading stress, ii) direct effect of lateral support condition on loading stress and combined loading and thermal stress, iii) the interactive effect between slab thickness and modulus of subgrade reaction on loading stress, iv) the interactive effect between thermal strain gradient and modulus of subgrade reaction on combined loading and thermal stress, v) the interactive effect between thermal strain gradient and joint spacing on combined loading and thermal stress.

Figures 26 (a) and 27 (a) illustrate the interactive effect between slab thickness and base/subbase thickness on loading stress at the bottom and top of the slab, respectively. It can be seen that the increase in base/subbase thickness results in a reduction in stress magnitude with diminishing effect as the slab thickness increases. As the base/subbase layer provides uniformity of support to the slab, an increase in base/subbase thickness reduces the magnitude of loading stress. The results suggest that from the loading stress standpoint the base/subbase thickness should also have a substantial effect on slab cracking for a pavement system with a thin slab, especially thinner than 10 in. However, the results should not suggest that the base/subbase thickness has a less significant impact for a pavement system with a thicker slab, since

the base/subbase layer could also affect the drainage characteristic of the pavement system.

Figures 26 (b) and 27 (b) suggest that lateral support condition has only direct effect on loading stress and combined loading and thermal stress. For various surrounding conditions, it was found that AC shoulder results in the highest stress magnitude as compared to PCC shoulder and widened lane. This could imply that from the standpoint of load-related distress a pavement system with PCC shoulder or widened lane should have a better performance than a pavement system with AC shoulder.

The impact of lateral support condition along with lateral wander of traffic loading was further illustrated in Figure 28 (a), suggesting that the lateral load location directly affects the magnitude of pavement stress for all types of lateral support condition. The results also imply the significance of the location of traffic paint stripe as it would dictate the location of wheel path.

It should be noted that the parametric study results are based on wheel path as the lateral load locations, which are 20 in. for PCC and AC shoulders and 44 in. for widened lane. The impact of lateral support condition and various lateral load locations are illustrated in Figure 28 (b). While lateral support condition has a significant effect on loading stress magnitude, its effect on thermal stress magnitude appears to be insignificant as shown in the figure. This implies that the variation in lateral support condition should not affect temperature-related performance of the pavement.

Figures 26 (c) and 27 (c) illustrate the interactive effect between slab thickness and modulus of subgrade reaction on loading stress at the bottom and top of the slab, respectively. It can be seen that the increase in modulus of subgrade reaction results in a

reduction in stress magnitude with diminishing effect as the slab thickness increases. The results suggest that from the loading stress standpoint the modulus of subgrade reaction should also have a substantial effect on slab cracking for a pavement system with a thin slab, especially thinner than 10 in.

However, Figures 26 (d) and 27 (d) illustrate an interactive effect between thermal strain gradient and modulus of subgrade reaction on combined loading and thermal stress. It could be suggested that an increase in the magnitude of modulus of subgrade reaction results in an increase in the magnitude of thermal stress as the combined stress magnitudes are compared to the loading stress magnitudes in Figures 26 (c) and 27 (c). From the mechanistic standpoint, this could imply that a roadbed with higher modulus of subgrade reaction should result in a better load-related performance but not for a temperature-related performance. However, the mechanistic behavior alone may not sufficiently provide such a conclusion to the actual performance of the pavement, since a roadbed with higher modulus of subgrade reaction usually also has a better erodibility resistance and also a better drainage characteristic.

Figures 26 (e) and 27 (e) suggest that from the loading stress standpoint joint spacing should not have a significant effect on load-related performance of the pavement. As stated by the Portland Cement Association's thickness-design procedure, the presence of joints has no effect on the pavement stress magnitude, since the load is placed adjacent to the midslab away from the joints. However, it should be noted that the results did not account for the interaction between axle spacing and joint spacing, which will be further discussed in Chapter 5.

When combined with thermal stress, Figure 26 (f) and 27 (f) illustrate an interactive effect between thermal strain gradient and joint spacing on combined loading and thermal stress. This implies that an increase in joint spacing should result in a higher level of temperature-related distress.

Figures 26 (h) and 27 (h) illustrate the impact of load configuration on pavement stress magnitude. The results imply that a more complex axle group should result in a lower pavement stress magnitude. However, the results did not account for the interaction between axle spacing and joint spacing. The impact of load configuration and its interaction with joint spacing will be further discussed in Chapter 5 through the use of influence surface technique.

Justification of the selection of AGG factor

Boundary support condition along the longitudinal joints of the slabs is characterized through AGG factor in ISLAB2000 program. It is crucial that an appropriate value of AGG factor is selected to represent the load transfer mechanism. The AGG factor can be empirically estimated as follows (Crovetti, 1994):

$$AGG = \left(\frac{\frac{1}{LTE} - 0.01}{0.012} \right)^{-\frac{1}{0.849}} \cdot k \cdot l \qquad (30)$$

Where AGG = AGG factor

LTE = Load transfer efficiency, percent

ℓ = Radius of relative stiffness, in

k = Modulus of subgrade reaction

The radius of relative stiffness is defined as follows:

$$l = \sqrt[4]{\frac{E \cdot h^3}{12\left(1-\mu^2\right) \cdot k}} \tag{31}$$

Where ℓ = Radius of relative stiffness, in

E = Elastic modulus of layer 1

h = Thickness of layer 1

μ = Poisson's ratio for layer 1

k = Modulus of subgrade reaction

In general, the typical values of LTE for tied concrete shoulder and untied AC shoulder vary from 25-90% and 0-40%, respectively. Based on equation 1, the ranges of AGG/kℓ were calculated as 0-0.77 and 0.34-16.5 for tied concrete shoulder and untied AC shoulder, respectively. Based on the inputs in the parametric study, the range of kℓ varies from 1188 to 8286 psi. A sensitivity study of the effect of AGG factor on magnitude of edge stresses is conducted for ranges of AGG factor from 5 to 7,000 psi (AC shoulder and widened lane) and from 300 to 2,500,000 psi (concrete shoulder). Based on these results, the AGG factors of 1,000,000 psi and 1,000 psi are selected for tied concrete shoulder and untied AC shoulder for the parametric study, respectively. Note that this sensitivity study is conducted for 177-in. joint spacing and 18-kips single axle at flat slab condition. Several sensitivity plots are generated as illustrated in Figures 30 (a) through (c). It can be seen that the stress magnitude is not significantly sensitive to AGG factor for concrete shoulder and widened lane, while for AC shoulder the variation

in stress magnitude could be up to 10% from the stress magnitude computed based on the selected AGG factor (1,000 psi). Table 6 summarizes the details of the documented interaction.

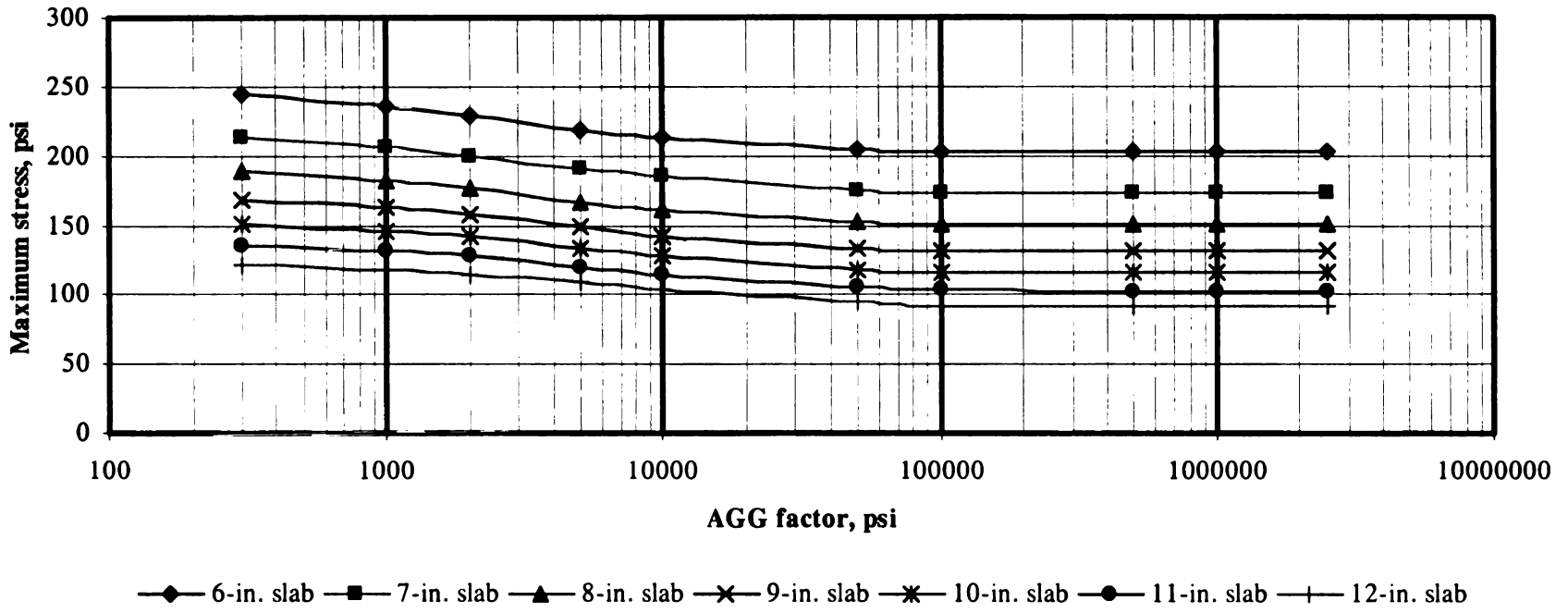

(a) Concrete shoulder

Figure 30: Effect of longitudinal joint AGG factor on stress magnitude

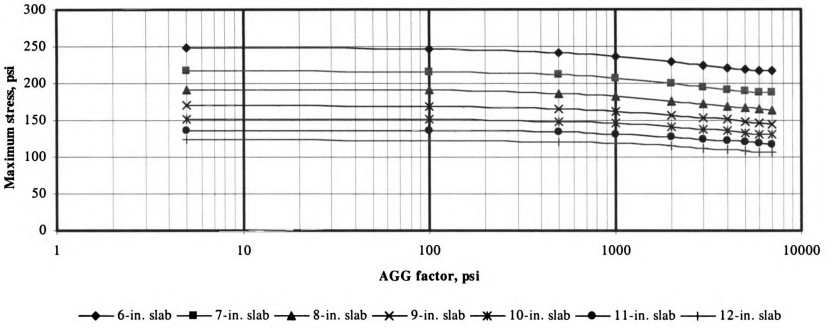

(b) AC shoulder

Figure 30: Effect of longitudinal joint AGG factor on stress magnitude (continued)

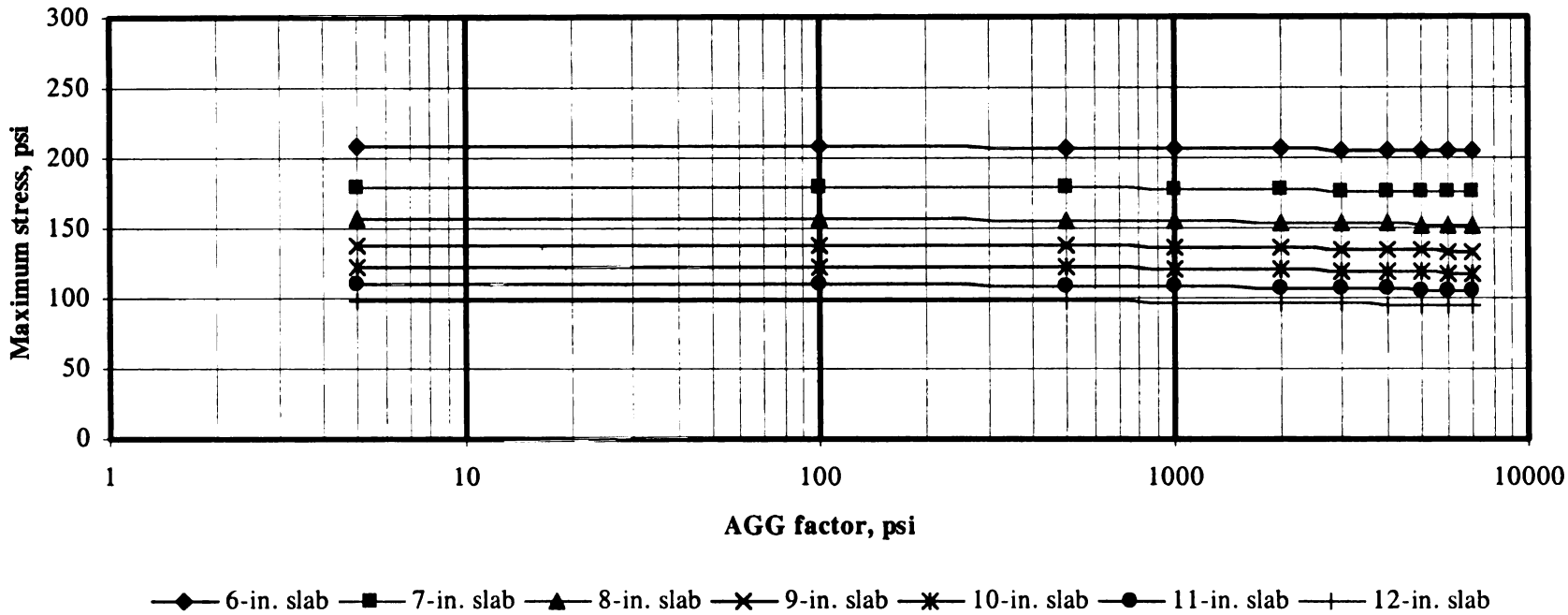

(c) Widened lane

Figure 30: Effect of longitudinal joint AGG factor on stress magnitude (continued)

Table 6: Summary of interaction between parameters on stresses

Parameters	Slab condition	Response type	Effects of parameters
Slab thickness versus base/subbase thickness	Flat slab	Longitudinal at bottom of slab	Thicker base/subbase thickness results in lower stress, but smaller magnitude of stress reduction was observed with thicker slab
		Longitudinal at top of slab	Same as that for longitudinal stress at bottom of slab
		Transverse at bottom of slab	Same as that for longitudinal stress at bottom of slab
	Curled slab	Longitudinal at bottom of slab	With higher temperature differential (thicker slab), thicker base/subbase thickness results in higher stress magnitude
		Longitudinal at top of slab	Same as that for longitudinal stress at bottom of slab
		Transverse at bottom of slab	Same as that for longitudinal stress at bottom of slab
Slab thickness versus modulus of subgrade reaction	Flat slab	Longitudinal at bottom of slab	Higher value of modulus of subgrade reaction results in lower stress value. There is no significant interaction between these parameters observed.
		Longitudinal at top of slab	Same as that for longitudinal stress at bottom of slab
		Transverse at bottom of slab	Same as that for longitudinal stress at bottom of slab
	Curled slab	Longitudinal at bottom of slab	Higher value of modulus of subgrade reaction results in higher stress value. Change in stress due to modulus of subgrade reaction is larger as temperature differential increases (slab thickness increases), and eventually the change in stress will remain constant.
		Longitudinal at top of slab	Same as that for longitudinal stress at bottom of slab
		Transverse at bottom of slab	Same as that for longitudinal stress at bottom of slab

Table 6: Summary of interaction between parameters on stresses (continued)

Parameters	Slab condition	Response type	Effects of parameters
Slab thickness versus lateral support condition	Flat slab	Longitudinal at bottom of slab	Higher stress value is observed in pavement with asphalt shoulder. There is no significant interaction between these parameters observed.
		Longitudinal at top of slab	Same as that for longitudinal stress at bottom of slab
		Transverse at bottom of slab	The magnitude of stress are about the same for all three lateral support conditions. There is no significant interaction between these parameters observed.
	Curled slab	Longitudinal at bottom of slab	Higher stress value is observed in pavement with asphalt shoulder. There is no significant interaction between these parameters observed.
		Longitudinal at top of slab	Same as that for longitudinal stress at bottom of slab
		Transverse at bottom of slab	Higher stress value is observed in pavement with widened lane. There is no significant interaction between these parameters observed.

Table 6: Summary of interaction between parameters on stresses (continued)

Parameters	Slab condition	Response type	Effects of parameters
Thermal strain gradient versus base/subbase thickness	177-in. joint spacing, curled slab	Longitudinal at bottom of slab	Increase in product of CTE with thermal gradient linearly results in increase in stress magnitude. Interaction between these parameters is observed that increase in stress magnitude due to increase in product of CTE with thermal gradient is more intense with thicker base/subbase
		Longitudinal at top of slab	Same as that for longitudinal stress at bottom of slab
		Transverse at bottom of slab	Same as that for longitudinal stress at bottom of slab
	315-in. joint spacing, curled slab	Longitudinal at bottom of slab	Increase in product of CTE with thermal gradient linearly results in increase in stress magnitude. However, the interaction observed for 177-in. joint spacing is not observed for this 315-in. joint spacing.
		Longitudinal at top of slab	Increase in product of CTE with thermal gradient linearly results in increase in stress magnitude. However, the interaction observed for 177-in. joint spacing is not observed for this 315-in. joint spacing.
		Transverse at bottom of slab	Same as that for 177-in. joint spacing

Table 6: Summary of interaction between parameters on stresses (continued)

Parameters	Slab condition	Response type	Effects of parameters
Thermal strain gradient versus base/subbase thickness	177-in. joint spacing, curled slab	Longitudinal at bottom of slab	Increase in product of CTE with thermal gradient linearly results in increase in stress magnitude. Interaction between these parameters is observed that increase in stress magnitude due to increase in product of CTE with thermal gradient is more intense with higher value of moduluf of subgrade reaction
		Longitudinal at top of slab	Same as that for longitudinal stress at bottom of slab
		Transverse at bottom of slab	Same as that for longitudinal stress at bottom of slab
	315-in. joint spacing, curled slab	Longitudinal at bottom of slab	Increase in product of CTE with thermal gradient linearly results in increase in stress magnitude. However, the interaction observed for this 315-in. joint spacing is not as intense as that for 177-in. joint spacing.
		Longitudinal at top of slab	Increase in product of CTE with thermal gradient linearly results in increase in stress magnitude. However, the interaction observed for this 315-in. joint spacing is not as intense as that for 177-in. joint spacing.
		Transverse at bottom of slab	Same as that for 177-in. joint spacing

Table 6: Summary of interaction between parameters on stresses (continued)

Parameters	Slab condition	Response type	Effects of parameters
Thermal strain gradient versus joint spacing	Curled slab	Longitudinal at bottom of slab	Increase in product of CTE with thermal gradient linearly results in increase in stress magnitude. Interaction between these parameters is observed that increase in stress magnitude due to increase in product of CTE with thermal gradient is more intense with longer joint spacing.
		Longitudinal at top of slab	Same as that for longitudinal stress at bottom of slab
		Transverse at bottom of slab	Increase in product of CTE with thermal gradient linearly results in increase in stress magnitude. Joint spasphalting has no significant impasphaltt on stress magnitude.

CHAPTER IV

INTERPOLATION SCHEME

Interpolation is a statistical procedure used to approximate unknown values (non-nodal points) in the vicinity of known values (nodal points). An interpolation scheme in this study is used because it is required to obtain mechanistic responses for all the combinations of the non-discrete inputs, not addressed in the final experimental matrix. The experimental matrix includes all possibilities of all the discrete design inputs: slab thickness, joint spacing, lateral support condition, and load configuration. However, only three values were specified for each of these non-discrete inputs in the final experimental matrix:

- Modulus of subgrade reaction (30, 100, 200 psi/in.),
- Base/subbase thickness (4, 16, 26 in.),
- Thermal strain gradients (0, $\pm 10 \times 10^{-6}$, $\pm 20 \times 10^{-6}$ in.$^{-1}$).

The interpolation process in this study is used to approximate the results that are not directly analyzed by the finite element model across ranges of the three non-discrete input parameters: modulus of subgrade reaction, base/subbase thickness, thermal strain gradient, this interpolation scheme is a three-dimensional process.

4.1 Least-squares criteria

The statistical method of least-squares approximation, proposed by Carl Friedrich Gauss in 1795 (Rassias, 1991), is applied to develop and evaluate interpolation schemes in this

study. The method is unbiased and algebraically provides an approximation to a dependent variable $\tilde{Y}$, with minimal variance. With a linear model, coefficients β_j for the least-squares solution satisfy the normal equations:

$$\frac{\partial\left(\sum_{i=1}^{n} e_i^2\right)}{\partial \beta_j} = 0 \quad , j = 0, 1, 2, \ldots, m \tag{32}$$

where $\tilde{Y}_i$ is the value of variable $\tilde{Y}$ at point i,

$\tilde{y}_i = \beta_0 + \beta_1 \cdot \tilde{x}_i^1 + \beta_2 \cdot \tilde{x}_i^2 + \beta_3 \cdot \tilde{x}_i^3 + \ldots + \beta_m \cdot \tilde{x}_i^m$ is the predicted value at point i,

$e_i = \tilde{Y}_i - \tilde{y}_i$ is the predicted value's error, and $\tilde{x}_i^1, \tilde{x}_i^2, \tilde{x}_i^3, \ldots \tilde{x}_i^m$ are independent (predictor) variables evaluated at point i, $i = 1, 2, \ldots, n$.

The matrix formulation of the solution in the nonsingular case is:

$$\tilde{y}_i = \beta_0 + \beta_1 \cdot \tilde{x}_i^1 + \beta_2 \cdot \tilde{x}_i^2 + \beta_3 \cdot \tilde{x}_i^3 + \ldots + \beta_m \cdot \tilde{x}_i^m = \bar{x}_i \cdot \bar{\beta} \tag{33}$$

$$\bar{x}_i = \left\{ 1 \quad \tilde{x}_i^1 \quad \tilde{x}_i^2 \quad \ldots \quad \tilde{x}_i^m \right\} \tag{34}$$

$$\bar{\beta} = \begin{Bmatrix} \beta_0 \\ \beta_1 \\ \beta_2 \\ \vdots \\ \beta_m \end{Bmatrix} = \left[X^T \cdot X \right]^{-1} \cdot X^T \cdot \hat{Y} \tag{35}$$

$$X = \begin{Bmatrix} \bar{x}_1 \\ \bar{x}_2 \\ \bar{x}_3 \\ \vdots \\ \bar{x}_n \end{Bmatrix} = \begin{Bmatrix} 1 & \tilde{x}_1^1 & \tilde{x}_1^2 & \ldots & \tilde{x}_1^m \\ 1 & \tilde{x}_2^1 & \tilde{x}_2^2 & \ldots & \tilde{x}_2^m \\ 1 & \tilde{x}_3^1 & \tilde{x}_3^2 & \ldots & \tilde{x}_3^m \\ \vdots & \vdots & \vdots & & \vdots \\ 1 & \tilde{x}_n^1 & \tilde{x}_n^2 & \ldots & \tilde{x}_n^m \end{Bmatrix} \tag{36}$$

$$\hat{Y} = \begin{Bmatrix} \tilde{Y}_1 \\ \tilde{Y}_2 \\ \tilde{Y}_3 \\ \vdots \\ \tilde{Y}_n \end{Bmatrix} = X \cdot \overline{\beta} \qquad (37)$$

4.2 Development of interpolation scheme

First, a sensitivity study was conducted to investigate the impact of the three non-discrete input parameters. The impact of modulus of subgrade reaction and base/subbase thickness on the magnitude of stresses were found to be highly non-linear as the change in the slope of the relationship was observed. On the other hand, initial trials showed the impact of thermal strain gradient to have little curvature. Therefore, the interpolation process is divided into two steps: (i) two-dimensional interpolation based on known anchor results obtained from the finite element model across the ranges of the base/subbase thickness and the modulus of subgrade reaction at each level of the thermal strain gradient, and (ii) one-dimensional interpolation based on the interpolated results from step 1 across the range of the thermal strain gradient. The overview of the interpolation process is illustrated in Figure 31. Using the least-squares criteria, several interpolation schemes were developed and compared as discussed later. The prototype of the interpolation scheme is explained below in matrix form.

Step 1:

$$\sigma(H^*, k^*, \alpha_i) = \overline{X}^* \cdot \hat{\beta} \qquad (38)$$

Where $\sigma(H^*, k^*, \alpha_i)$ is mechanistic response for the target combination of base/subbase thickness and modulus of subgrade reaction at level α_i of thermal strain gradient

$\overline{X}^*$ is the vector of predictor variables

$$\overline{X}^* = \left\{ 1 \quad H^* \quad H^{*2} \quad \ln(k^*) \quad H^* \cdot \ln(k^*) \quad H^{*2} \cdot \ln(k^*) \quad \frac{1}{k^*} \quad \frac{H^*}{k^*} \quad \frac{H^{*2}}{k^*} \right\} \tag{39}$$

Where H* is target base/subbase thickness

k* is target modulus of subgrade reaction

α_1 is anchor value 0 $in.^{-1}$ of thermal strain gradient

α_2 is anchor value $\pm 10 \times 10^{-6}$ $in.^{-1}$ of thermal strain gradient

α_3 is anchor value $\pm 20 \times 10^{-6}$ $in.^{-1}$ of thermal strain gradient

$\hat{\beta}$ is least-squares coefficient vector

$$\hat{\beta} = \begin{Bmatrix} \beta_0 \\ \beta_1 \\ \beta_2 \\ \beta_3 \\ \beta_4 \\ \beta_5 \\ \beta_6 \\ \beta_7 \\ \beta_8 \end{Bmatrix} = \left[X^T \cdot X \right]^{-1} \cdot X^T \cdot \hat{\sigma} \tag{40}$$

$$X = \begin{Bmatrix} \bar{X}(H_1,k_1) \\ \bar{X}(H_1,k_2) \\ \bar{X}(H_1,k_3) \\ \bar{X}(H_2,k_1) \\ \bar{X}(H_2,k_2) \\ \bar{X}(H_2,k_3) \\ \bar{X}(H_3,k_1) \\ \bar{X}(H_3,k_2) \\ \bar{X}(H_3,k_3) \end{Bmatrix} = \begin{bmatrix} 1 & H_1 & H_1^2 & \ln(k_1) & \ln(k_1)H_1 & \ln(k_1)H_1^2 & \frac{1}{k_1} & \frac{H_1}{k_1} & \frac{H_1^2}{k_1} \\ 1 & H_1 & H_1^2 & \ln(k_2) & \ln(k_2)H_1 & \ln(k_2)H_1^2 & \frac{1}{k_2} & \frac{H_1}{k_2} & \frac{H_1^2}{k_2} \\ 1 & H_1 & H_1^2 & \ln(k_3) & \ln(k_3)H_1 & \ln(k_3)H_1^2 & \frac{1}{k_3} & \frac{H_1}{k_3} & \frac{H_1^2}{k_3} \\ 1 & H_2 & H_2^2 & \ln(k_1) & \ln(k_1)H_2 & \ln(k_1)H_2^2 & \frac{1}{k_1} & \frac{H_2}{k_1} & \frac{H_2^2}{k_1} \\ 1 & H_2 & H_2^2 & \ln(k_2) & \ln(k_2)H_2 & \ln(k_2)H_2^2 & \frac{1}{k_2} & \frac{H_2}{k_2} & \frac{H_2^2}{k_2} \\ 1 & H_2 & H_2^2 & \ln(k_3) & \ln(k_3)H_2 & \ln(k_3)H_2^2 & \frac{1}{k_3} & \frac{H_2}{k_3} & \frac{H_2^2}{k_3} \\ 1 & H_3 & H_3^2 & \ln(k_1) & \ln(k_1)H_3 & \ln(k_1)H_3^2 & \frac{1}{k_1} & \frac{H_3}{k_1} & \frac{H_3^2}{k_1} \\ 1 & H_3 & H_3^2 & \ln(k_2) & \ln(k_2)H_3 & \ln(k_2)H_3^2 & \frac{1}{k_2} & \frac{H_3}{k_2} & \frac{H_3^2}{k_2} \\ 1 & H_3 & H_3^2 & \ln(k_3) & \ln(k_3)H_3 & \ln(k_3)H_3^2 & \frac{1}{k_3} & \frac{H_3}{k_3} & \frac{H_3^2}{k_3} \end{bmatrix} \quad (41)$$

Where H_1, H_2 and H_3 are base/subbase thicknesses 4, 16 and 26 in.

k_1 , k_2 and k_3 are k-values 30, 100 and 200 psi/in.

$$\hat{\sigma} = \begin{Bmatrix} \sigma_{11} \\ \sigma_{12} \\ \sigma_{13} \\ \sigma_{21} \\ \sigma_{22} \\ \sigma_{23} \\ \sigma_{31} \\ \sigma_{32} \\ \sigma_{33} \end{Bmatrix} \quad (42)$$

Where σ_{ij} is known anchor value stress from finite element analysis at H_i and k_j

Step 2:

$$\sigma(H^*,k^*,\alpha^*) = \overline{\alpha}^* \cdot \hat{\gamma} \tag{43}$$

Where $\sigma(H^*,k^*,\alpha^*)$ is mechanistic response for the target combination of base/subbase thickness, modulus of subgrade reaction, and product of $\alpha(\Delta T/D)$

$\overline{\alpha}^*$ is the vector of predictor variables based on $\alpha(\Delta T/D)$

$$\overline{\alpha}^* = \begin{Bmatrix} 1 & \alpha^* & \alpha^{*2} \end{Bmatrix} \tag{44}$$

$$\hat{\gamma} = \begin{Bmatrix} \gamma_0 \\ \gamma_1 \\ \gamma_2 \end{Bmatrix} = \begin{bmatrix} 1 & \alpha_1 & \alpha_1^2 \\ 1 & \alpha_2 & \alpha_2^2 \\ 1 & \alpha_3 & \alpha_3^2 \end{bmatrix}^{-1} \cdot \begin{Bmatrix} \sigma(H^*,k^*,\alpha_1) \\ \sigma(H^*,k^*,\alpha_2) \\ \sigma(H^*,k^*,\alpha_3) \end{Bmatrix} \tag{45}$$

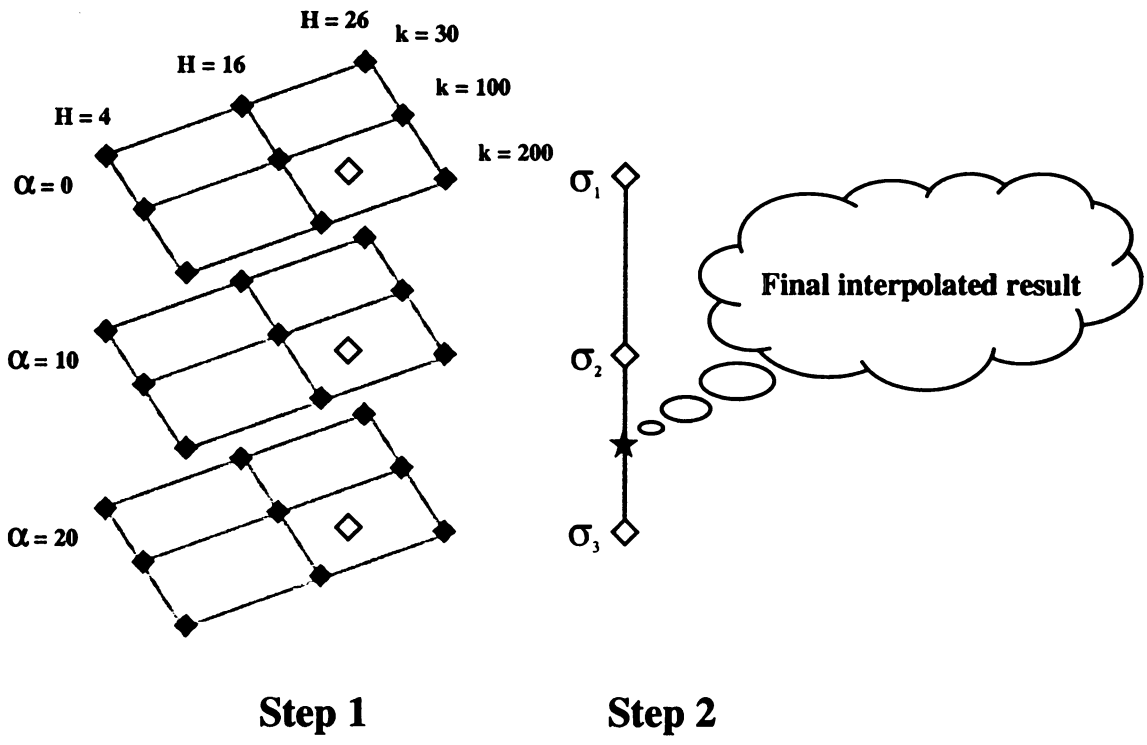

Figure 31: Interpolation process

Several interpolation schemes were developed following this prototype with different terms used in the prediction vectors (39) in step 1 and (44) in step 2. Examples of prediction vectors used in some of the schemes developed in this study are given in Table 7. It should be noted that the natural logarithm of modulus of subgrade reaction and the interaction terms with base/subbase thickness in the prediction matrices for schemes 15 and 16 are similar to terms suggested in the Westergaard's closed form stress equations (Huang, 1993). A significant drop in error due to the use of these terms was observed. Comparing the interpolated results with finite element results at non-nodal points validates these two interpolation schemes. Also note that the solutions to the normal equations for schemes 15 and 16 produce perfect fits at the nine nodal points corresponding to each level of the product $\alpha(\Delta T/D)$. Several more schemes have also been investigated. Most of these schemes that contain high order interaction term(s) in "step 1", e.g. $H^{*2}k^{*2}$, $H^{*}k^{*3}$, $H^{*3}k^{*}$, were found to result in low predictive power.

Table 7: Example prediction matrices

Scheme No.	Prediction Matrix for Step 1	Prediction Matrix for Step 2
Scheme 5	$\{1 \quad (H^*) \quad (k^*) \quad (H^*)^2 \quad (k^*)^2 \quad (H^*k^*)\}$	$\{1 \quad \alpha^*\}$
Scheme 6	$\{1 \quad (H^*) \quad (k^*) \quad (H^*)^2 \quad (k^*)^2 \quad (H^*k^*) \quad (H^*/k^*)^{0.5}\}$	$\{1 \quad \alpha^*\}$
Scheme 9	$\{1 \quad (H^*) \quad (k^*) \quad (H^*)^2 \quad (k^*)^2 \quad (H^*k^*) \quad (H^{*2}k^*)\}$	$\{1 \quad \alpha^*\}$
Scheme 10	$\{1 \quad (H^*) \quad (k^*) \quad (H^*)^2 \quad (k^*)^2 \quad (H^*k^*) \quad (H^*k^{*2})\}$	$\{1 \quad \alpha^*\}$
Scheme 15	$\{1 \quad (H^*) \quad (H^*)^2 \quad (\ln k^*) \quad (H^*\ln k^*) \quad (H^{*2}\ln k^*) \quad (1/k^*) \quad (H^*/k^*) \quad (H^{*2}/k^*)\}$	$\{1 \quad \alpha^*\}$
Scheme 16	$\{1 \quad (H^*) \quad (H^*)^2 \quad (\ln k^*) \quad (H^*\ln k^*) \quad (H^{*2}\ln k^*) \quad (1/k^*) \quad (H^*/k^*) \quad (H^{*2}/k^*)\}$	$\{1 \quad \alpha^* \quad \alpha^{*2}\}$

4.3 Validation of interpolation schemes

The validation process is illustrated in Figures 32 and 33. This process involves obtaining finite element results at non-nodal points that were not used in developing interpolation schemes. Error is defined as the difference between the interpolated result and the finite element result directly obtained from the ISLAB2000.

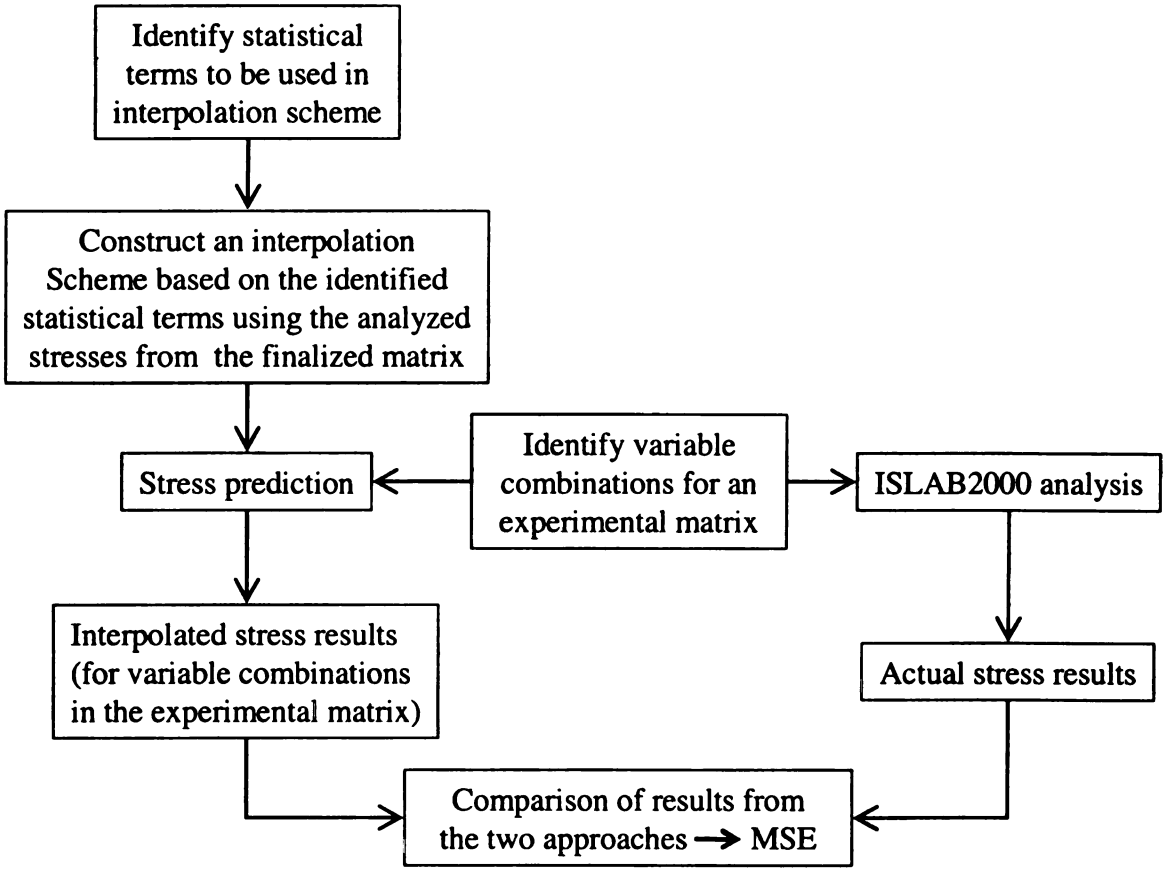

Figure 32: Validation procedure

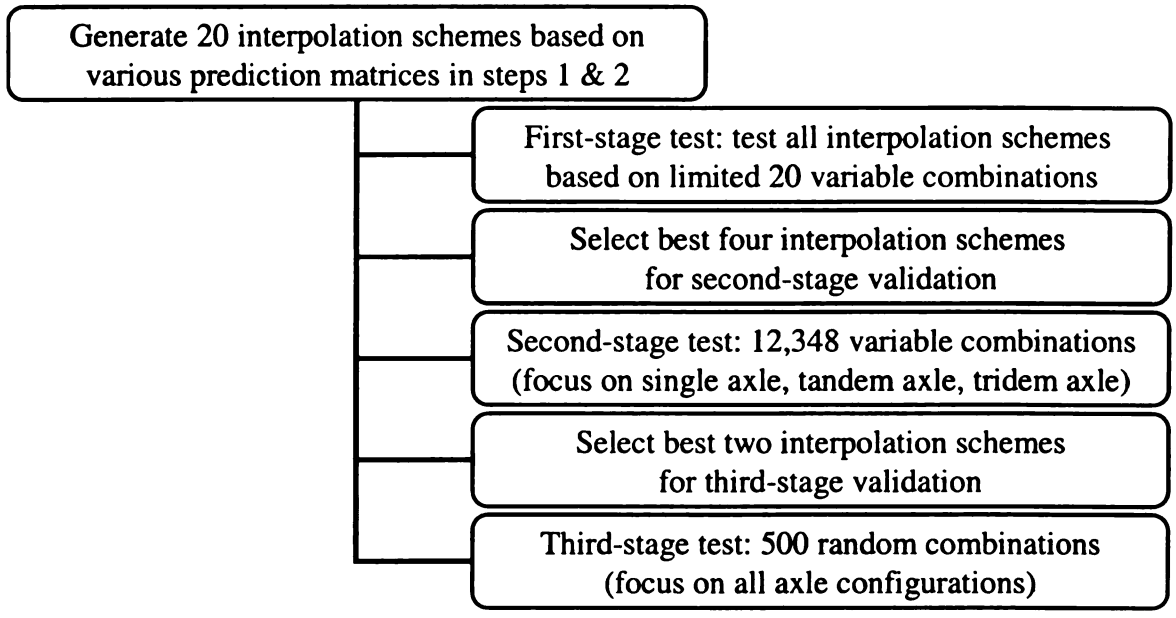

Figure 33: Overview of validation process

More than 12,000 non-nodal finite element results have been obtained and used to validate and select from interpolation schemes. The three stages of the validation process are as follows:

Validation stage 1: In the first stage, all interpolation schemes that were developed are validated with a limited number of non-nodal points. The validation matrix covers 20 non-nodal points with variations of all three non-discrete variables for a fixed combination of discrete variables (10-in. SLAB thickness, 16-in. base/subbase thickness, 177-in. joint spacing, concrete shoulder, and single axle edge loading). Non-nodal points at the middle between the anchor values are considered in this validation stage. These non-nodal points are believed to result in large magnitudes of errors since they are far from the anchor values. Mean square of errors (MSE), bias, and variance are the measures of the goodness of fit of the interpolation schemes considered in this study.

These values were calculated for the errors (difference between the finite element results and interpolated results) obtained from the validation process. Table 8 and Figures 34 (a) through (d) illustrate the validation results at the first stage for the six most promising interpolation schemes. The comparison between finite element and interpolated results illustrated in Figure 34 (a) suggests that all these schemes have high predictive power. However, based on MSE, bias, and variance in Table 8 and Figures 34 (b) through (d), schemes 5, 6, 15, and 16 appear to be the best four performing interpolation schemes, and consequently are selected for the next stage of validation.

Validation stage 2: The validation matrix for this stage consists of 12,348 non-nodal points (midpoints between nodal points). The experimental matrix of "validation stage 2" is a complete factorial of all discrete variable and five values of each of the three non-discrete variables (including two midpoints). The process focuses on single, tandem, and tridem axles for all non-discrete and discrete variables. The middle points between nodal points are also used for this validation stage. The validation results are illustrated in Table 9 and Figures 35 (a) through (d). Based on the validation results, the two best performing schemes are 15 and 16.

Validation stage 3: Instead of using the middle points between nodal points in the validation process, this validation stage considers non-nodal points that are randomly selected. This validation stage is based on 300 cases for single through tridem axles and 200 cases for quad through multi-axle (8). The validation results illustrated in Figures 36 (a) and (b) and Table 10 suggest that scheme 16 is the best performing interpolation

scheme. It should be noted that the only difference between schemes 15 and 16 is the prediction matrix in step 2. The values of MSE, bias, and variance obtained from this validation stage were found to be larger than those obtained from the other stages. Since the values for all three non-discrete variables are randomly selected, this validation stage should produce a more realistic result compared to the other stages.

Table 8: Summary of goodness of fit – stage 1

Goodness of Fit	Scheme 5	Scheme 6	Scheme 9	Scheme 10	Scheme 15	Scheme 16
MSE, psi^2	6.34	32.29	202.31	267.70	1.24	1.22
Variance, psi^2	6.23	13.64	69.31	120.71	1.08	1.07
Absolute bias, psi	0.33	4.32	11.53	12.12	0.40	0.39

Table 9: Summary of goodness of fit – stage 2

Goodness of Fit	Scheme 5	Scheme 6	Scheme 15	Scheme 16
MSE, psi^2	16.47	41.43	4.15	3.11
Variance, psi^2	16.40	28.39	4.14	3.11
Absolute bias, psi	0.25	3.61	0.11	0.01

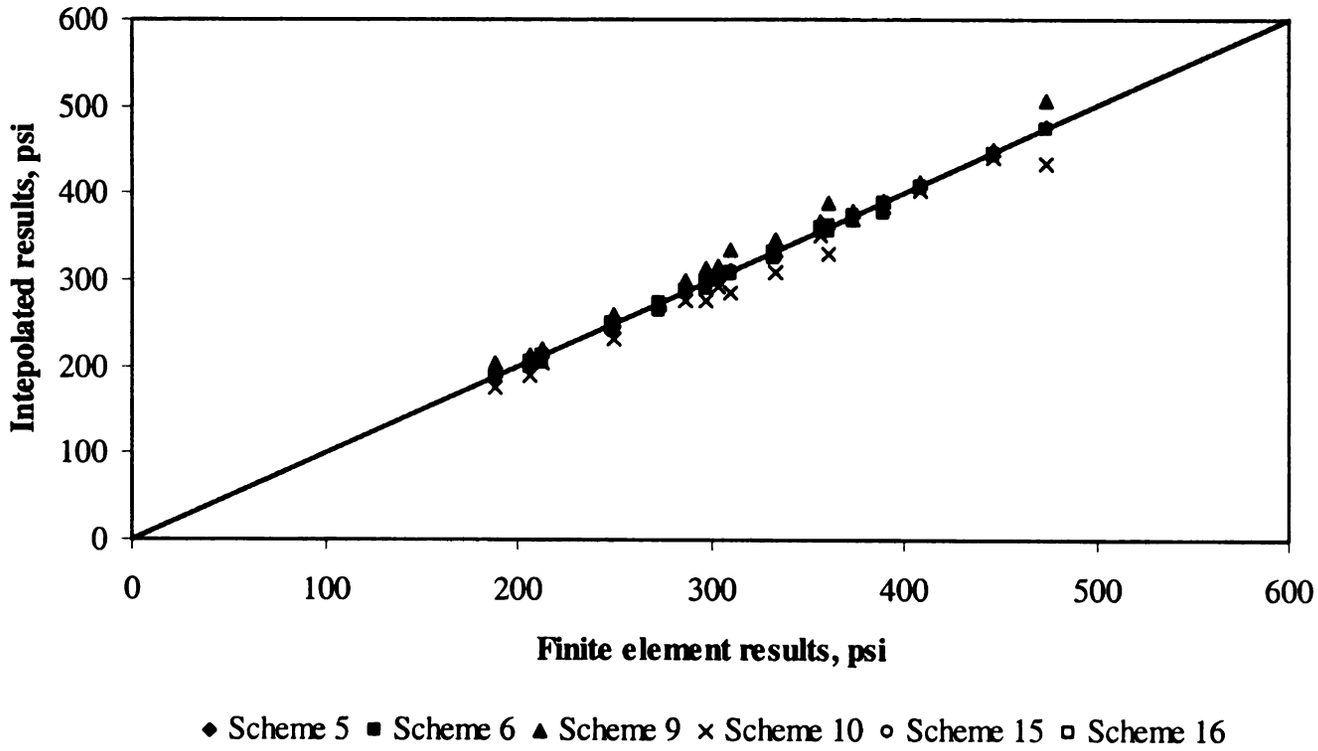

(a) Comparison between finite element and interpolated results

Figure 34: Validation results – stage 1

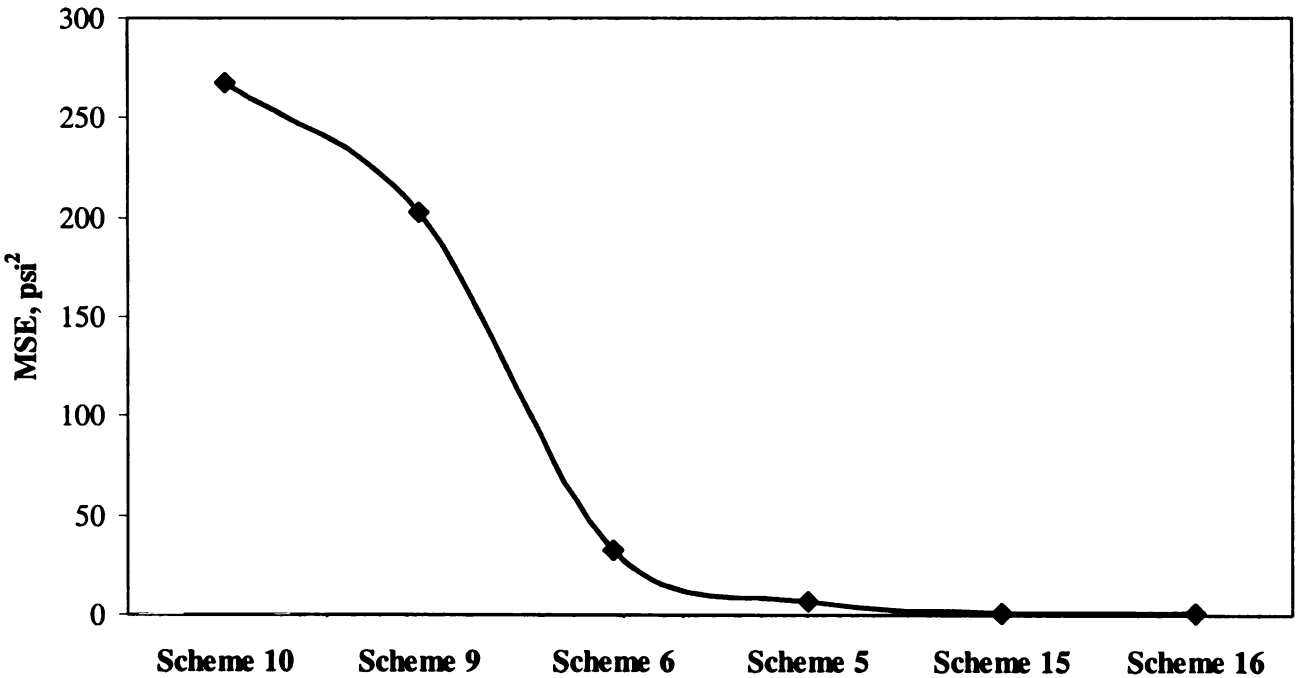

(b) Comparison of MSE

Figure 34: Validation results – stage 1 (continued)

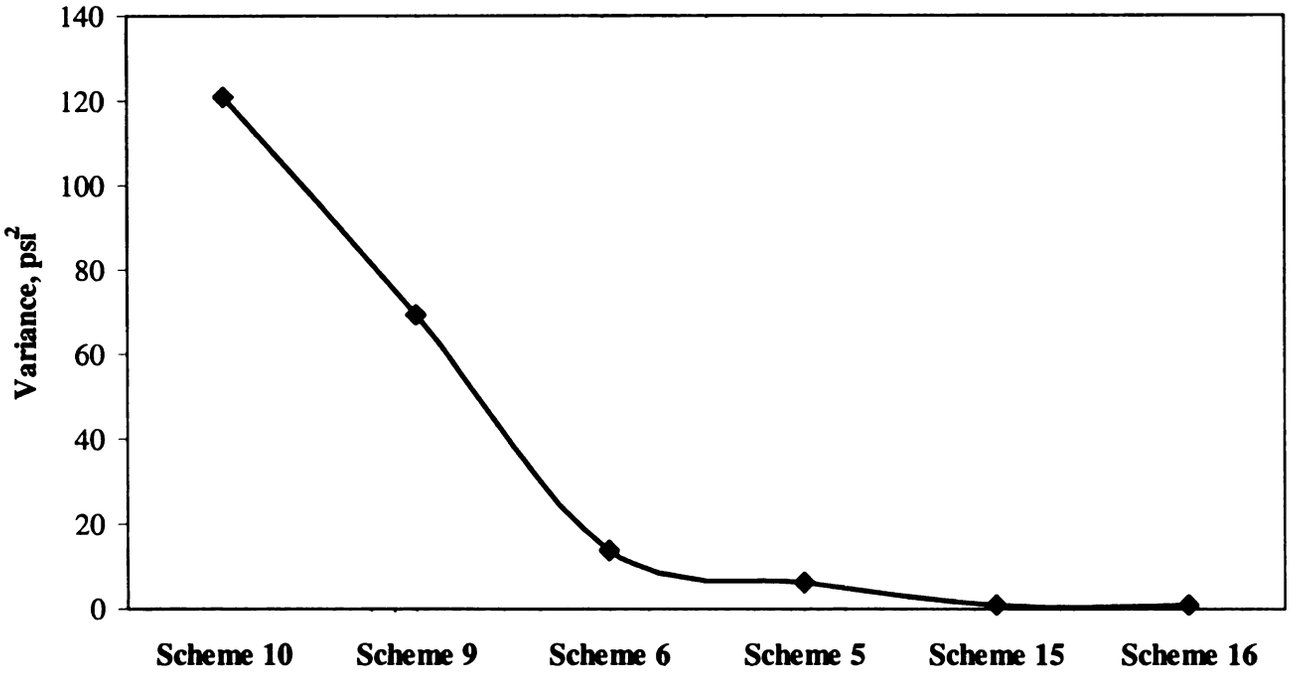

(c) Comparison of variance

Figure 34: Validation results – stage 1 (continued)

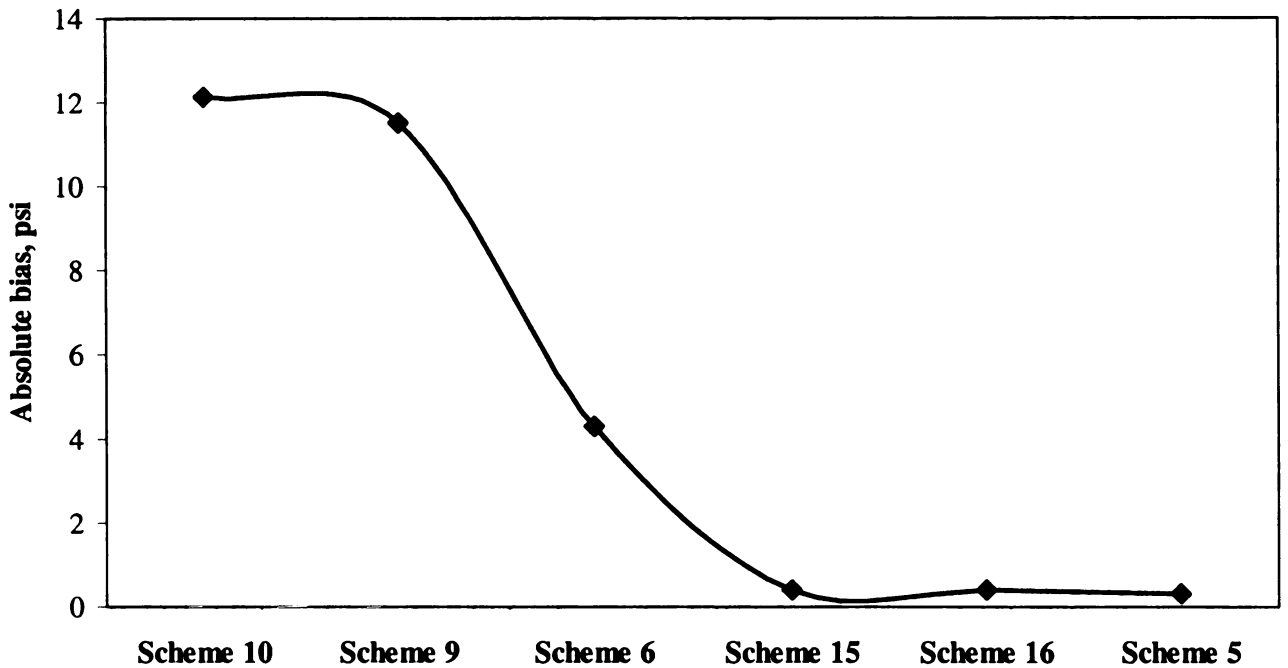

(d) Comparison of absolute value of bias

Figure 34: Validation results – stage 1 (continued)

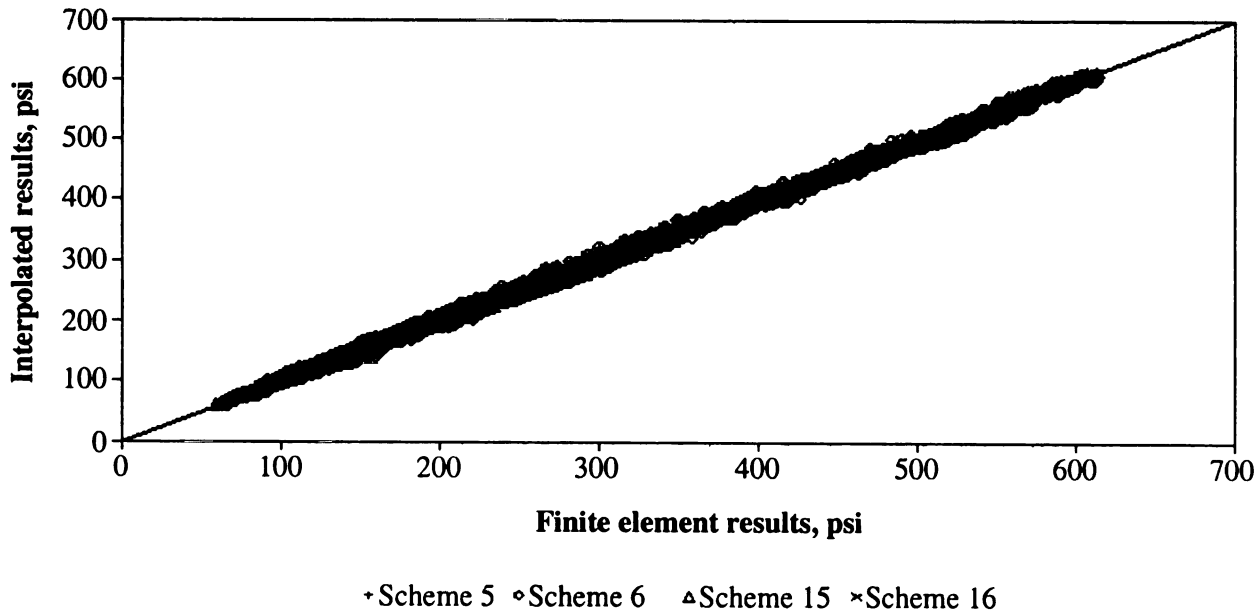

(a) Comparison between finite element and interpolated results

Figure 35: Validation results – stage 2

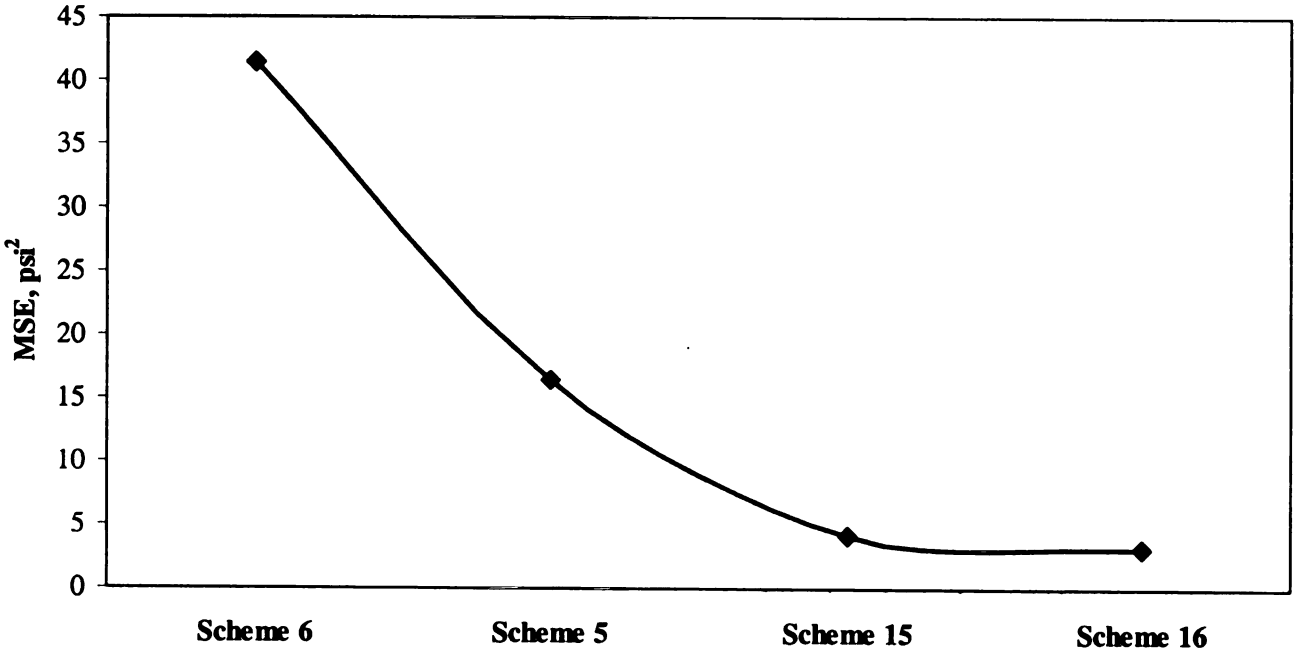

(b) Comparison of MSE

Figure 35: Validation results – stage 2 (continued)

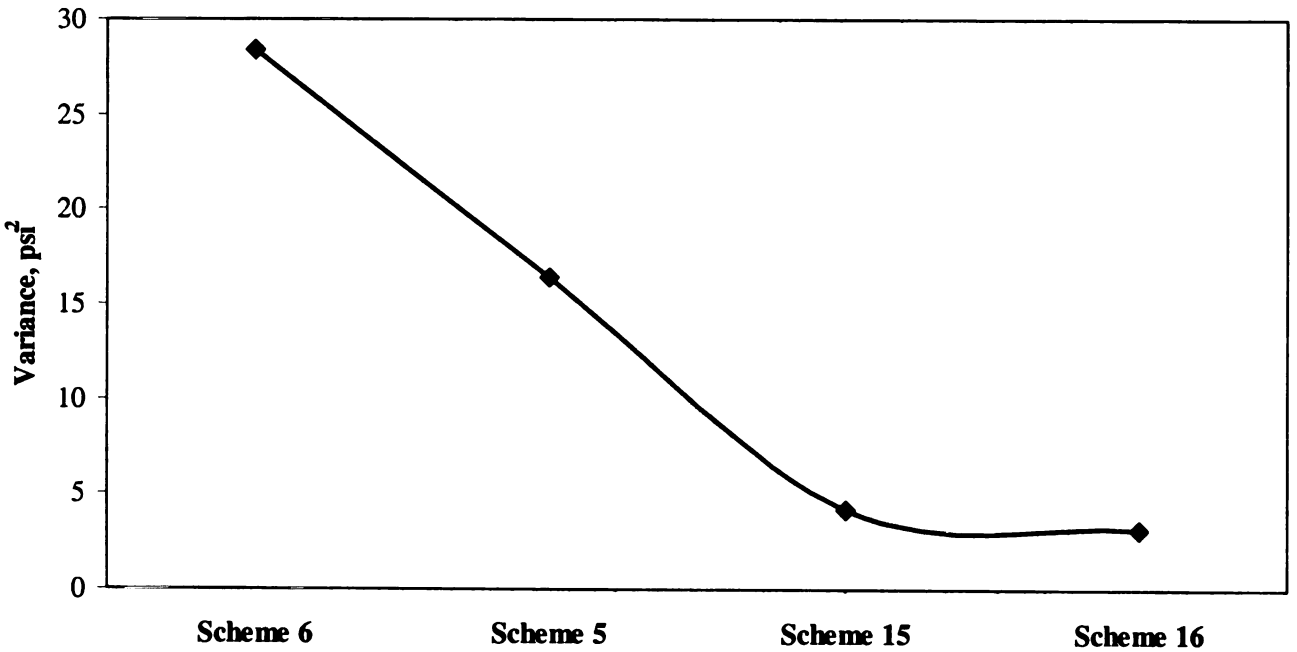

(c) Comparison of variance

Figure 35: Validation results – stage 2 (continued)

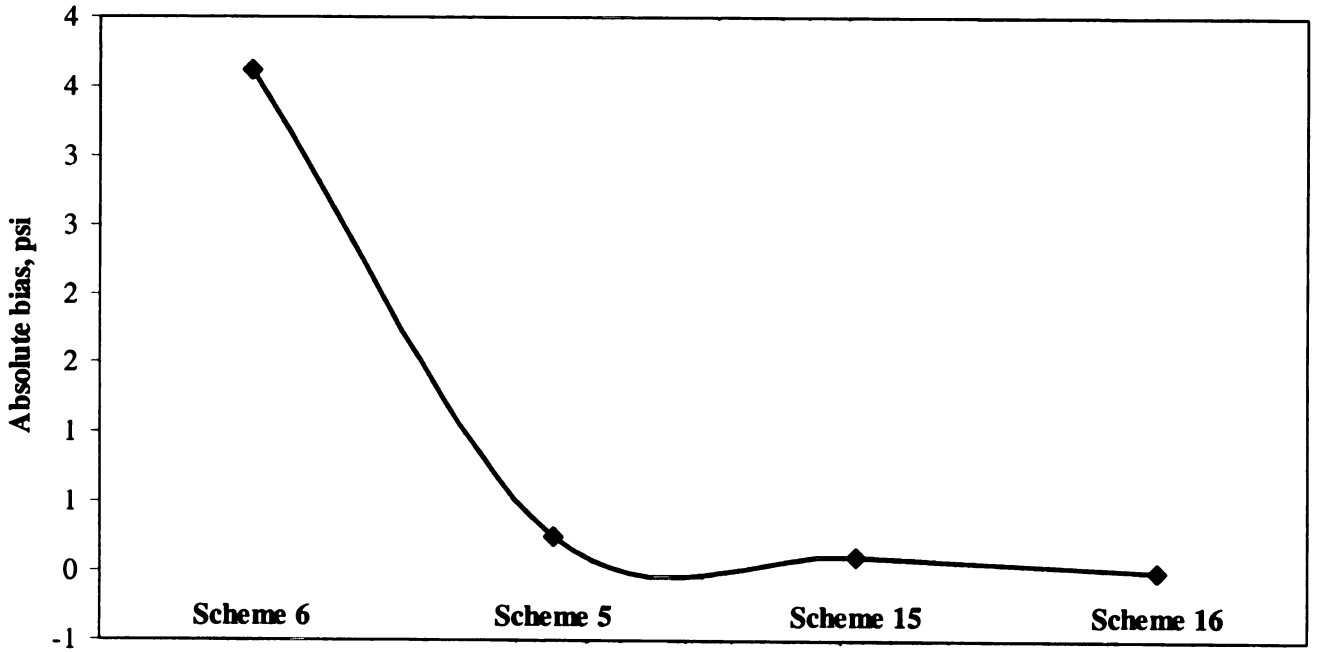

(d) Comparison of absolute value of bias

Figure 35: Validation results – stage 2 (continued)

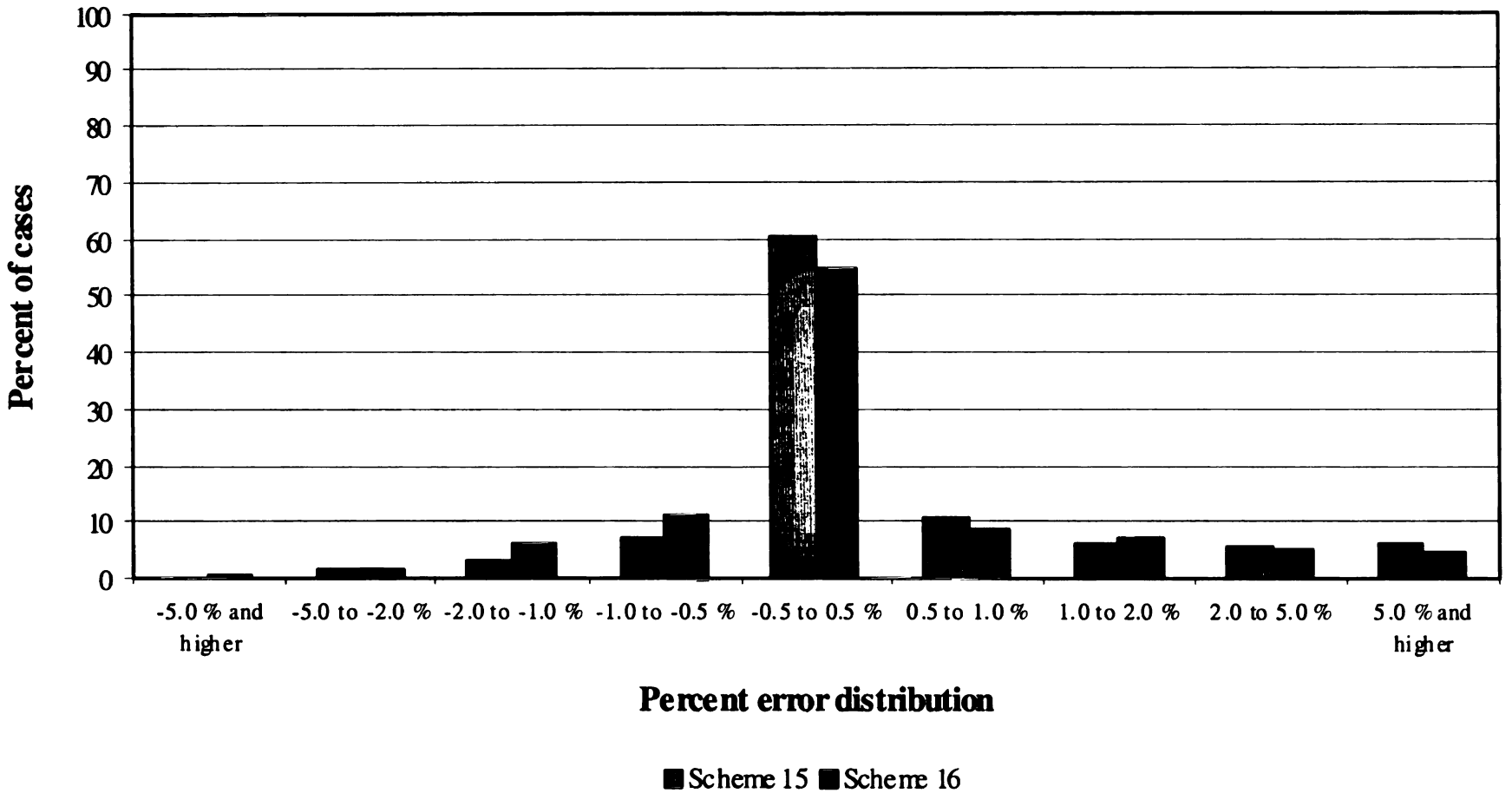

(a) Example error distribution

Figure 36: Validation results – stage 3

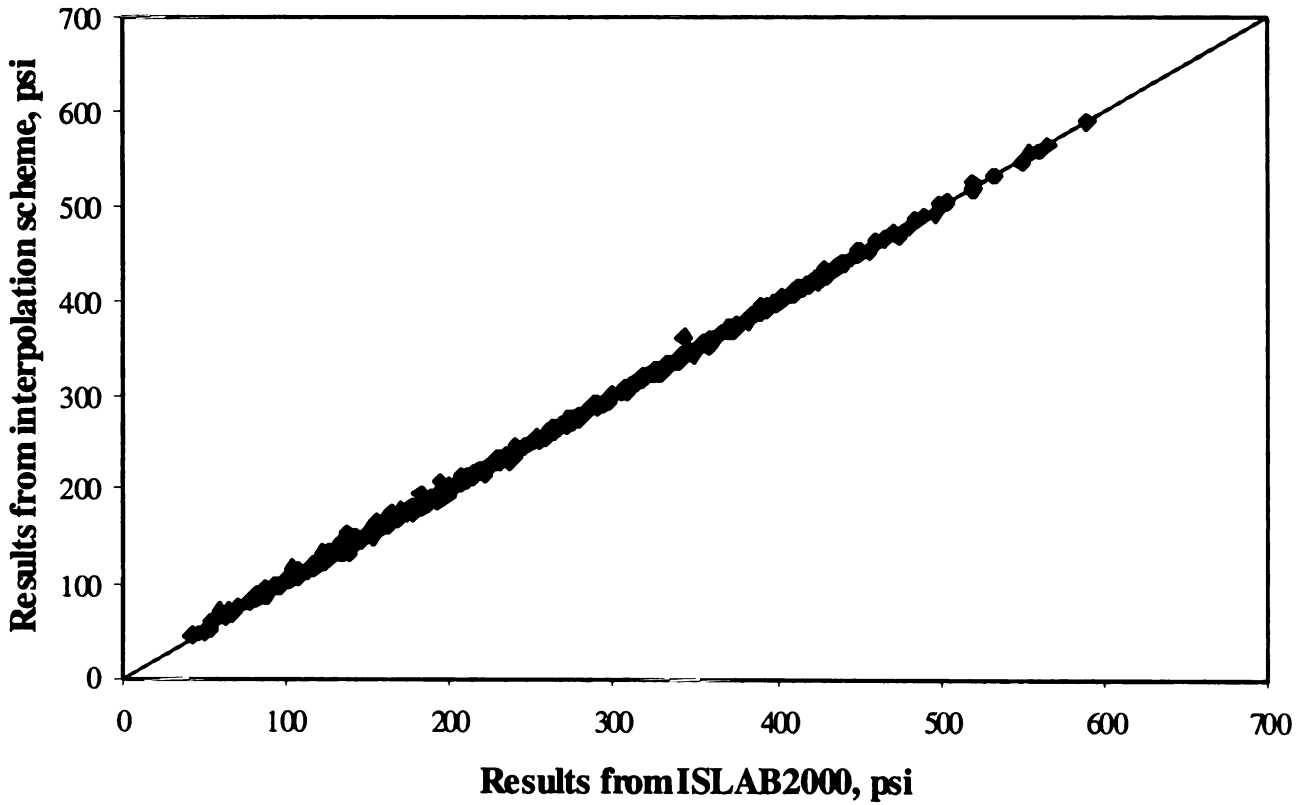

(b) Comparison between actual and interpolated results for scheme 16

Figure 36: Validation results – stage 3 (continued)

Table 10: Comparison of scheme 15 and scheme 16 – stage 3

Cases No.	Statistic Results	Longitudinal stress at bottom		Transverse stress at bottom	
		Scheme15	Scheme16	Scheme15	Scheme16
1-500	MSE, psi^2	11.51	8.89	16.40	15.93
	Bias, psi	1.02	0.51	-0.89	-1.21
	Variance, psi^2	10.46	8.63	15.61	14.47
1-300	MSE, psi^2	3.90	3.38	9.70	8.77
	Bias, psi	0.16	0.02	-0.36	-0.59
	Variance, psi^2	3.87	3.38	9.57	8.41
301-500	MSE, psi^2	22.93	17.15	26.46	26.67
	Bias, psi	2.32	1.25	-1.68	-2.13
	Variance, psi^2	17.53	15.60	23.63	22.14

MSE represents the overall measure of goodness of fit, estimated by the average of square of errors (difference between actual and interpolated values). The MSE can be decomposed into two parts: square of bias, and variance. Bias is the average value of errors, while variance is the average of squared deviation of errors from average error. Based on the results from validation stage 3, scheme 16 was found to be most promising. Figures 36 (a) and (b) provide for a comparison between actual and interpolated values based on these schemes. These figures suggest that the interpolation schemes can be a reliable alternative for approximating mechanistic responses. Table 10 also shows that the interpolated results for single through tridem axles are exceptionally accurate and precise. The biases and variances associated with the longitudinal stress at the bottom of the concrete slab for scheme 16 are 0.0 psi and 3.38 psi^2, respectively. Overall maximum absolute biases based on this scheme are 0.6 psi and 2.1 psi for single through tridem axles and quad through multi-axle (8), respectively.

As the validation process has been completed, the interpolation scheme is used to generate a catalog of stresses by assigning a series of sets of design inputs that are not addressed in the experimental matrix. The catalog of stresses can be found in the MDOT report.

4.4 Sample of calculation

Interpolation schemes can simply be implemented by carrying out the mathematical expressions as described earlier. For example, the longitudinal stress is estimated at the bottom of the slab. The pavement cross-section includes a 275-mm (11-in.) concrete slab, 500-mm (20-in.) base/subbase thickness, 40.7-kPa/mm (150-psi/in.) modulus of subgrade

reaction, 8.0-m (27-ft) joint spacing, tied concrete shoulder, thermal strain gradient of $6x10^{-7}$ mm^{-1} ($15x10^{-6}$ $in.^{-1}$), 142-kN (32-kips) tandem axle.

Step 1: Interpolation in 2-D space across the ranges of base/subbase thickness and modulus of subgrade reaction

Prediction vector was computed based on H* and k* at the target point (equation 39)

$$\bar{X}^* = \left\{ 1 \quad 500 \quad 500^2 \quad \ln(40.7) \quad 500 \cdot \ln(40.7) \quad 500^2 \cdot \ln(40.7) \quad \frac{1}{40.7} \quad \frac{500}{40.7} \quad \frac{500^2}{40.7} \right\}$$

A nine by nine matrix was computed based on H_i and k_j at nodal points (equation 41)

$$X = \begin{bmatrix} \bar{X}(100,8.13) \\ \bar{X}(100,27.1) \\ \bar{X}(100,54.2) \\ \bar{X}(400,8.13) \\ \bar{X}(400,27.1) \\ \bar{X}(400,54.2) \\ \bar{X}(650,8.13) \\ \bar{X}(650,27.1) \\ \bar{X}(650,54.2) \end{bmatrix} = \begin{bmatrix} 1 & 100 & 10000 & 2.10 & 210 & 20956 & 0.1230 & 12.30 & 1230 \\ 1 & 100 & 10000 & 3.30 & 330 & 32995 & 0.0369 & 3.69 & 369 \\ 1 & 100 & 10000 & 3.99 & 399 & 39927 & 0.0185 & 1.85 & 185 \\ 1 & 400 & 160000 & 2.10 & 838 & 335290 & 0.1230 & 49.20 & 19680 \\ 1 & 400 & 160000 & 3.30 & 1320 & 527925 & 0.0369 & 14.76 & 5904 \\ 1 & 400 & 160000 & 3.99 & 1597 & 638829 & 0.0185 & 7.38 & 2952 \\ 1 & 650 & 422500 & 2.10 & 1362 & 885374 & 0.1230 & 79.95 & 51968 \\ 1 & 650 & 422500 & 3.30 & 2145 & 1394053 & 0.0369 & 23.99 & 15590 \\ 1 & 650 & 422500 & 3.99 & 2595 & 1686908 & 0.0185 & 11.99 & 7795 \end{bmatrix}$$

Anchor stresses were obtained from finite element analysis at H_i and k_j for α=0, 4 and $8x10^{-7}$ mm^{-1} (equation 42)

$$\hat{\sigma}_{\alpha=0} = \begin{Bmatrix} 1092.6 \\ 752.2 \\ 619.3 \\ 1074.0 \\ 738.9 \\ 608.0 \\ 1017.1 \\ 698.3 \\ 573.7 \end{Bmatrix} kPa \qquad \hat{\sigma}_{\alpha=4} = \begin{Bmatrix} 2192.8 \\ 2312.6 \\ 2320.8 \\ 2182.2 \\ 2298.5 \\ 2305.9 \\ 2150.9 \\ 2255.9 \\ 2266.8 \end{Bmatrix} kPa \qquad \hat{\sigma}_{\alpha=8} = \begin{Bmatrix} 3293.1 \\ 3857.2 \\ 3989.4 \\ 3290.4 \\ 3857.1 \\ 4035.2 \\ 3284.7 \\ 3813.5 \\ 3969.3 \end{Bmatrix} kPa$$

Then, stresses at target H* and k* corresponding to the three levels of α were computed (equations 38 and 40)

$$\sigma(500,40.7,0) = \overline{X}^* \cdot \left[\left[X^T \cdot X \right]^{-1} \cdot X^T \cdot \hat{\sigma}_{\alpha=0} \right] = 647.5 \quad kPa$$

$$\sigma(500,40.7,4) = \overline{X}^* \cdot \left[\left[X^T \cdot X \right]^{-1} \cdot X^T \cdot \hat{\sigma}_{\alpha=4} \right] = 2292.5 \quad kPa$$

$$\sigma(500,40.7,8) = \overline{X}^* \cdot \left[\left[X^T \cdot X \right]^{-1} \cdot X^T \cdot \hat{\sigma}_{\alpha=8} \right] = 3954.2 \quad kPa$$

Step 2: Interpolation in 1-D across the range of thermal strain gradient

Prediction vector was computed based on α* at the target point (equation 44)

$$\overline{\alpha}^* = \begin{Bmatrix} 1 & 6 & 6^2 \end{Bmatrix}$$

A least-squares coefficient vector was computed based on α_i at nodal points and computed stresses obtained from step 1 (equation 45)

$$\hat{y} = \begin{bmatrix} 1 & 0 & 0 \\ 1 & 4 & 16 \\ 1 & 8 & 64 \end{bmatrix}^{-1} \cdot \begin{Bmatrix} 647.5 \\ 2292.5 \\ 3954.2 \end{Bmatrix} = \begin{Bmatrix} 647.5 \\ 409.1 \\ 0.526 \end{Bmatrix}$$

Then, the target stress at H*, k* and α* was computed (equation 43)

$$\sigma(H^*, k^*, \alpha^*) = \{1 \quad 6 \quad 36\} \cdot \begin{Bmatrix} 647.5 \\ 409.1 \\ 0.526 \end{Bmatrix} = 3121.2 \quad kPa$$

The stress computed using interpolation scheme is 3121.2 kPa (452.353 psi), while the result directly obtained from finite element analysis is 3121.8 kPa (452.436 psi). The error of interpolated result in this example is 0.6 kPa (0.1 psi) or 0.02%.

CHAPTER V

INFLUENCE SURFACE TECHNIQUE

The use of influence surfaces is considered the most effective and efficient approach for the analysis of structures that carry moving loads, and for the derivation of critical loading scenarios for such structures. However, in practice the influence surface technique has mostly been limited to the analysis of bridge decks. Logically, the analysis of rigid pavements should also benefit from the versatility of influence surfaces, since they also carry moving loads.

In general, the same logic applied to an influence line for a one-dimensional member is applicable to an influence surface for a two-dimensional structure. An influence surface for a plate or shell structure is usually represented pictorially as a three-dimensional plot (e.g., a surface plot or contour plot) of mechanistic responses at a reference point due to a unit load at various locations over the entire surface of the structure. When placing the unit load at a location on the structure, the values displayed on an influence surface represent the magnitudes of the mechanistic response at the reference point. In this study, a series of influence surfaces have been generated as the influence field data for various reference points, types of mechanistic responses, and boundary conditions stored in an extensive computer database. These are then directly used to compute magnitudes of stresses for design purposes and determine critical loading scenarios. The influence field data are also used to draw three-dimensional plots of influence surfaces to provide graphical interfaces for the application.

The use of influence surfaces for rigid pavements did not gain popularity since rigid pavements were designed empirically, where the mechanistic responses of the pavements were not essential to the design process. With the recent development of the mechanistic-based design procedure, and its forthcoming adoption, the application of the influence surface technique will be useful for the analysis and design of rigid pavements. This chapter establishes the application of the influence surface technique in rigid pavement study by accomplishing three goals: (i) to propose an approach for developing influence surfaces for rigid pavements, (ii) to validate the proposed approach, and (iii) to demonstrate potential applications of influence surfaces for further rigid pavement study.

5.1 Construction of influence surfaces

While the analytical approach to obtain influence surfaces has been well established with successes documented by many researchers, the process requires the structural analysis to be expressed mathematically. This alone can be a daunting task for a large and complex structure like a rigid pavement system. Therefore, a numerical process to obtain influence surfaces is proposed. The overall process of constructing influence surfaces is presented in Figure 37.

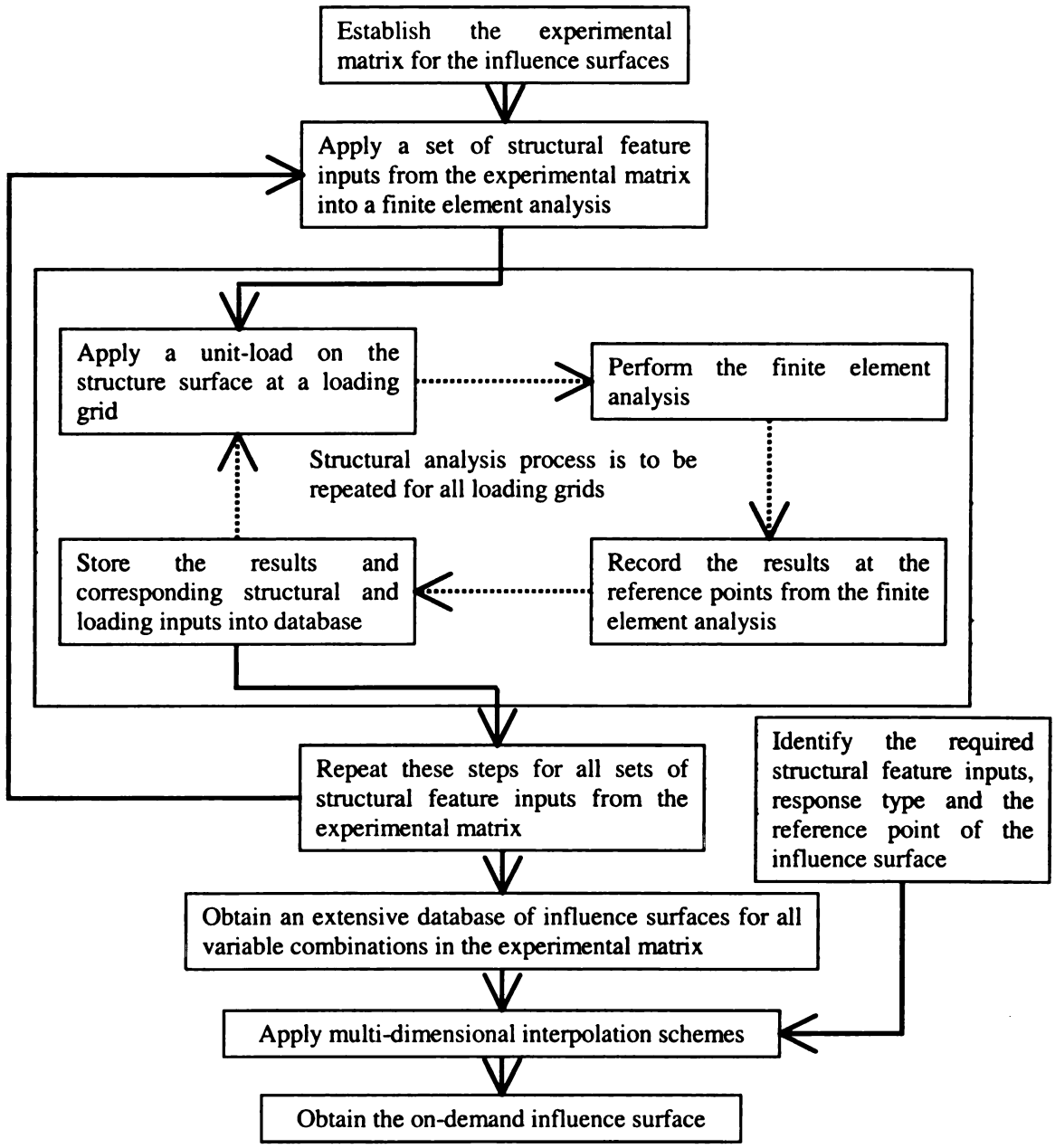

Figure 37: Overall process of the proposed approach to influence surface

The structural analysis part of this approach relies on an available finite element program specially developed for a multi-plate pavement system supported by a dense liquid foundation (Tabatabaie and Barenberg, 1978). It should be noted that the proposed

approach is also applicable to other conventional models for analysis of rigid pavements (Huang and Wang, 1973; Chou and Huang, 1981; Ozbeki et al., 1985; Davids and Mahoney, 1999). Through the determination of influence fields provided by a series of finite element analyses, influence surfaces for rigid pavement stresses are numerically assembled. Numerous finite element analyses are performed for a unit load by placing it all over the entire pavement slab surface one point at a time, while mechanistic responses at selected reference points are recorded and stored in an extensive computer database. This process is then repeated for other design variables. With the use of an interpolation scheme based on least-squares criteria, influence surfaces can be numerically generated on demand.

In general, limitations of the proposed approach should not be different from the limitations of the finite element method, on which the construction of the influence surfaces are based. While geometric non-linearity can possibly be handled by the finite element method (Davids and Mahoney, 1999), it is absolutely unacceptable to violate the principle of superposition, as it is the foundation of the influence surface technique. As a result, the proposed approach may not be applicable to heavily curled rigid pavements where the pavement structure is likely to exhibit geometric non-linearity due to the gap between slab and base layer.

Experimental matrix

As described in the overall process, the initial step towards the numerical approach of influence surfaces is to establish an experimental matrix containing ranges of structural feature inputs to be varied. Practically, variation of structural feature inputs of rigid

pavements is unlimited, including, but not limited to, layer thickness, layer material properties, joint designs, lateral support conditions, slab dimensions, skew orientations, and roadbed moduli. While the proposed technique should logically be applicable to all types and ranges of structural feature inputs, it is not an objective of this study to include all possible combinations of the aforementioned variables, but to propose the process and demonstrate the potential of the numerical approach of influence surfaces for rigid pavements. Concrete elastic modulus, Poisson's ratio, and unit weight are kept constant at $4x10^6$ psi, 0.15, and 150 lb/ft^3, respectively. Aggregate elastic modulus, Poisson's ratio, and unit weight are kept constant at $30x10^3$ psi, 0.35, and 105 lb/ft^3, respectively. Joint design is kept constant at 1.5 in. dowel diameter with 12 in. spacing center to center. This study does not include shoulder to offer significant lateral support to the slabs, assembling the general characteristics of an asphalt concrete shoulder. The key inputs selected as part of the experimental matrix in this study include concrete slab thickness ranging from 8 to 12 in., dense-graded aggregate base thickness ranging from 4 to 18 in., modulus of subgrade reaction ranging from 50 to 250 psi/in., slab length ranging from 15 to 20 ft, and slab width ranging from 12 to 14 ft. Altogether, there are 270 input combinations, including two levels of slab width, three levels of slab length, five levels of slab thickness, three levels of aggregate base thickness, and three levels of modulus of subgrade reaction.

In addition to these structural feature inputs, the construction of influence surfaces also involves various general points and reference points, as illustrated in Figure 11. Each combination of inputs requires a series of finite element analyses to be performed for a unit load positioned at every loading grid all over the pavement surface. As illustrated in

Figure 38, loading grids are spaced at 12 in., covering the entire area of three-slab surface of the pavement model. The number of loading grids on the pavement surface range from 540 to 840 grids, depending on the dimension of the slabs. However, with the advantage of the structural symmetric property, only a quarter of the surface area will need to be covered.

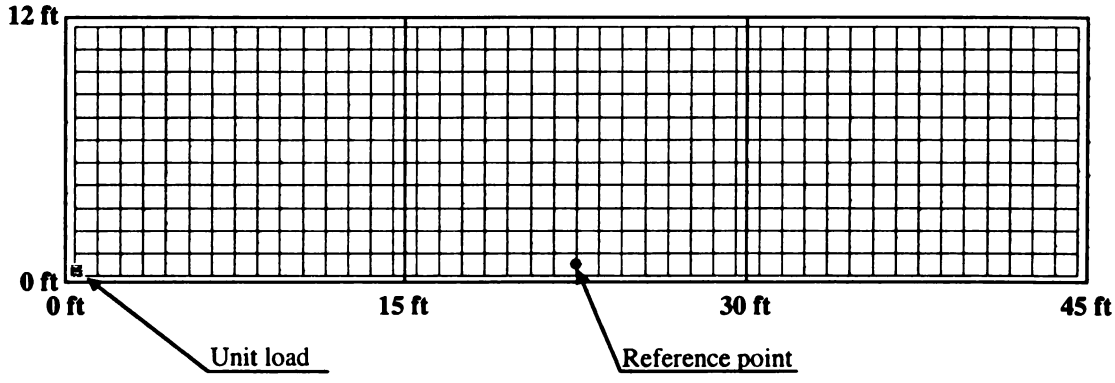

Figure 38: Typical loading grids, reference point, and unit load

An influence surface for a pavement system is a three-dimensional plot of a reference point's mechanistic responses to a unit load at various locations over the surface of the pavements; to be meaningful, the reference points should be the points where the mechanistic responses are pertaining to the design criteria. To relate the use of influence surfaces to the transverse cracking of the pavements, various mid-slab locations across the width of the slab were selected for reference points where critical values of longitudinal stress are expected. Figure 38 also illustrates a typical reference point in this study. The reference point shown in the figure is located at the mid-slab 12 in. away from the edge.

Since tire pressure, tire contact area, and tire aspect ratio have an impact on the mechanistic responses of rigid pavements obtained from the finite element method

(Ioannides, 1985), wheel load may not be treated as a discrete point load. Thus, in the formation of influence surfaces, it is of importance to appropriately select contact pressure, contact area, and aspect ratio for the unit load. Figure 39 presents a series of finite element analyses conducted to examine the impact of tire pressure and aspect ratio on pavement stress. In Figure 39 (a), the wheel load and tire aspect ratio are maintained at 9,000 lb and 1:1, respectively, while varying the tire contact area from 25 to 144 $in.^2$. The tire contact pressures ranged from 63 to 360 psi. Similarly, in Figure 39 (b), the wheel load and tire contact area are maintained at 9,000 lb and 100 $in.^2$, respectively, while varying the tire aspect ratio (width: length) from 2:1 to 1:3. As revealed in the figures, it is clear that both tire contact pressure and tire aspect ratio have an insignificant effect on pavement stress when the variations are within practical limits. As a result, a 10 in. by 10 in. square load of 9,000 lb is selected for the standard unit load. When compared to other tire pressures and aspect ratios, the results in Figure 39 suggest that the errors associated with the use of the standard unit load, instead of the actual wheel, are less than two percent within reasonable ranges.

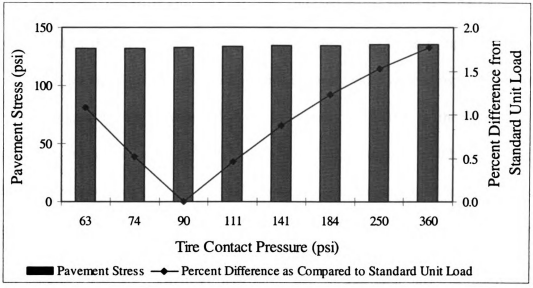

a) Impact of tire contact pressure on pavement stress

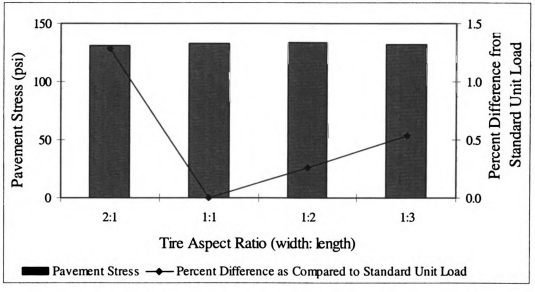

b) Impact of tire aspect ratio on pavement stress

Figure 39: Impact of tire contact pressure and aspect ratio on pavement stress

(Details: three-slab system of dimensions 12 ft by 15 ft with doweled joint, slab thickness of 10 in., aggregate base thickness of 4 in., modulus of subgrade reaction of 100 psi/in., wheel path at 24 in. from slab edge, mid-slab longitudinal stress underneath wheel path)

Interpolation process

As described in the overall process in Figure 37, the next step is to apply a series of interpolation schemes containing mechanistic responses only at loading grids and only for the structural features identified in the experimental matrix to the database. The interpolation process is applied only to the non-discrete variables, which are continuous in nature. Such variables include slab thicknesses, aggregate base thicknesses, moduli of subgrade reaction, and coordinates of general points and reference points on influence surfaces. While theoretically possible to also include slab widths and slab lengths in the interpolation process as they are numerical in their characteristic, they are actually limited to only a small number of design alternatives in practice. Consequently, slab widths and slab lengths are treated as discrete variables in this study. Only applicable across the ranges of non-discrete variables, the interpolation process thus requires repetitions for each of the combinations of discrete variables.

The interpolation process, through the least-squares method, involves a series of interpolation schemes. To disentangle the numerical complexity, the interpolation process is divided into three fundamental steps: (i) one-dimensional interpolation for a reference point, (ii) two-dimensional interpolation for a general point, and (iii) three-dimensional interpolation for structural feature inputs. Generally, with a function of two coordinates (as illustrated in Figure 11), reference point A (u, v) in this study could simply be viewed as a function of only one variable A ($u_{mid\text{-}slab}$, v), since the location for the reference points in this study is narrowed down to the various locations across the width of the slab at the mid-slab, where $u_{mid\text{-}slab}$ is the fixed u-coordinate at mid-slab. As a result, the response on the influence surface in this study is adjusted to a six-dimensional function

$\tilde{Y}(v,x,y,D,H,k)$, incorporating reference point (v), general point (x, y), slab thickness (D), aggregate base thickness (H), and modulus of subgrade reaction (k). The prototype of the interpolation schemes in matrix form is explained below.

Step 1: One-dimensional interpolation for a reference point

In the first step, a one-dimensional cubic interpolation scheme is selected. Cubic interpolation is preferred over linear and quadratic schemes since its error is significantly less. While more complex, the fourth degree interpolation scheme was not found to substantially improve the interpolated results. Note that each interpolated result obtained from a one-dimensional cubic interpolation scheme requires four mechanistic responses from the database. As the beginning of the interpolation process, this step directly retrieves the mechanistic responses at the anchor inputs from the database, $\tilde{Y}(v_i, x_j, y_k, D_l, H_m, k_n)$. Repeated at all anchor points (x_j, y_k, D_l, H_m, k_n), this step of the interpolation process is to propagate results at the desired reference point $\tilde{y}(v^*, x_j, y_k, D_l, H_m, k_n)$.

$$\tilde{y}(v^*, x_j, y_k, D_l, H_m, k_n) = \bar{X}_1(v^*) \cdot \hat{\beta}_1(x_j, y_k, D_l, H_m, k_n) \quad (46)$$

Where $\tilde{y}(v^*, x_j, y_k, D_l, H_m, k_n)$ is interpolated result for the targeted reference point at level x_j, y_k, D_l, H_m, and k_n, and

$\bar{X}_1(v^*)$ is the vector of predictor for step 1

$$\bar{X}_1(v^*) = \{1 \quad v^* \quad v^{*2} \quad v^{*3}\} \quad (47)$$

Where v* is the targeted reference point,

(x_j, y_k) are the sixteen most adjacent anchor general points,

D_l are anchor values of slab thickness where D_1, D_2,..., D_4 are the four most adjacent anchor values of slab thickness,

H_m are anchor values of aggregate base thickness where H_1, H_2 and H_3 are 4, 10, and 18 in., respectively,

k_n are anchor value of modulus of subgrade reaction where k_1, k_2 and k_3 are 13.6, 40.7, and 67.8 kPa/mm, respectively, and

$\hat{\beta}_1(x_j, y_k, D_l, H_m, k_n)$ is the least-squares coefficient vector for step 1

$$\hat{\beta}_1(x_j, y_k, D_l, H_m, k_n) = \left[X_1{}^T \cdot X_1 \right]^{-1} \cdot X_1{}^T \cdot \hat{Y}_1(x_j, y_k, D_l, H_m, k_n) \tag{48}$$

$$X_1 = \begin{bmatrix} 1 & v_1 & v_1^2 & v_1^3 \\ 1 & v_2 & v_2^2 & v_2^3 \\ 1 & v_3 & v_3^2 & v_3^3 \\ 1 & v_4 & v_4^2 & v_4^3 \end{bmatrix} \tag{49}$$

Where v_1, v_2,..., v_4 are the four most adjacent anchor reference points

$$\hat{Y}_1(x_j, y_k, D_l, H_m, k_n) = \begin{bmatrix} \tilde{Y}(v_1, x_j, y_k, D_l, H_m, k_n) \\ \tilde{Y}(v_2, x_j, y_k, D_l, H_m, k_n) \\ \tilde{Y}(v_3, x_j, y_k, D_l, H_m, k_n) \\ \tilde{Y}(v_4, x_j, y_k, D_l, H_m, k_n) \end{bmatrix} \tag{50}$$

Step 2: Two-dimensional interpolation for a general point

Based on the results at the specific reference point obtained in the first step, the second step further interpolates the results to specified general points on influence surfaces,

which is then repeated for all anchor values of structural inputs. To cubically interpolate the results for general points on a two-dimensional surface, each interpolation in this step requires 16 interpolated results from the previous step, which now serve as responses at anchor inputs. Repeated for all anchor structural inputs, the second step subsequently feeds results at the desired general points $\tilde{y}(v^*, x^*, y^*, D_l, H_m, k_n)$ into the last step of the interpolation process.

$$\tilde{y}(v^*, x^*, y^*, D_l, H_m, k_n) = \overline{X}_2(x^*, y^*) \cdot \hat{\beta}_2(v^*, D_l, H_m, k_n) \tag{51}$$

Where $\tilde{y}(v^*, x^*, y^*, D_l, H_m, k_n)$ is interpolated result for the targeted reference point and general point at level D_l, H_m, and k_n, and

$\overline{X}_2(x^*, y^*)$ is the vector of predictor for step 2

$$\overline{X}_2(x^*, y^*) = \left\{ x^{*3} \quad x^{*2} \cdot y^* \quad x^* \cdot y^{*2} \quad y^{*3} \right\} \tag{52}$$

Where (x*,y*) is targeted general point, and

$\hat{\beta}_2(v^*, D_l, H_m, k_n)$ is the least-squares coefficient vector for step 2

$$\hat{\beta}_2(v^*, D_l, H_m, k_n) = \left[X_2{}^T \cdot X_2 \right]^{-1} \cdot X_2{}^T \cdot \hat{Y}_2(v^*, D_l, H_m, k_n) \tag{53}$$

$$X_2 = \begin{bmatrix} x_1^3 & x_1^2 \cdot y_1 & x_1 \cdot y_1^2 & y_1^3 \\ x_1^3 & x_1^2 \cdot y_2 & x_1 \cdot y_2^2 & y_2^3 \\ \vdots & \vdots & \vdots & \vdots \\ x_4^3 & x_4^2 \cdot y_4 & x_4 \cdot y_4^2 & y_4^3 \end{bmatrix} \tag{54}$$

$$\hat{Y}_1(v^*, D_l, H_m, k_n) = \begin{bmatrix} \tilde{y}(v^*, x_1, y_1, D_l, H_m, k_n) \\ \tilde{y}(v^*, x_1, y_2, D_l, H_m, k_n) \\ \vdots \\ \tilde{y}(v^*, x_4, y_4, D_l, H_m, k_n) \end{bmatrix} \tag{55}$$

Step 3: Three-dimensional interpolation for structural feature input

The last step, which is a three-dimensional interpolation process, is divided into two parts: (i) one-dimensional interpolation across the range of slab thicknesses (D) to obtain results at the desired slab thickness $\tilde{y}(v^*, x^*, y^*, D^*, H_m, k_n)$ and (ii) two-dimensional interpolation across the ranges of aggregate base thickness (H) and moduli of subgrade reaction (k) to ultimately obtain the result at the desired slab thickness $\tilde{y}(v^*, x^*, y^*, D^*, H^*, k^*)$.

$$\tilde{y}(v^*, x^*, y^*, D^*, H_m, k_n) = \bar{X}_{3a}(D^*) \cdot \hat{\beta}_{3a}(v^*, x^*, y^*, H_m, k_n) \tag{56}$$

Where $\tilde{y}(v^*, x^*, y^*, D^*, H_m, k_n)$ is the interpolated result for the targeted reference point, general point, and slab thickness at level H_m, and k_n, and $\bar{X}_{3a}(D^*)$ is the predictor vector for the first part of step 3

$$\bar{X}_{3a}(D^*) = \begin{Bmatrix} 1 & D^* & D^{*2} & D^{*3} \end{Bmatrix} \tag{57}$$

Where D* is targeted slab thickness, and

$\hat{\beta}_{3a}(v^*, x^*, y^*, H_m, k_n)$ is the least-squares coefficient vector for the first part of step 3

$$\hat{\beta}_{3a}(v^*, x^*, y^*, H_m, k_n) = \left[X_{3a}{}^T \cdot X_{3a} \right]^{-1} \cdot X_{3a}{}^T \cdot \hat{Y}_{3a}(v^*, x^*, y^*, H_m, k_n) \tag{58}$$

$$X_{3a} = \begin{bmatrix} 1 & D_1 & D_1^2 & D_1^3 \\ 1 & D_2 & D_2^2 & D_2^3 \\ 1 & D_3 & D_3^2 & D_3^3 \\ 1 & D_4 & D_4^2 & D_4^3 \end{bmatrix} \tag{59}$$

$$\hat{Y}_{3a}(v^*, x^*, y^*, H_m, k_n) = \begin{bmatrix} \tilde{y}(v^*, x^*, y^*, D_1, H_m, k_n) \\ \tilde{y}(v^*, x^*, y^*, D_2, H_m, k_n) \\ \tilde{y}(v^*, x^*, y^*, D_3, H_m, k_n) \\ \tilde{y}(v^*, x^*, y^*, D_4, H_m, k_n) \end{bmatrix} \tag{60}$$

$$\tilde{y}(v^*, x^*, y^*, D^*, H^*, k^*) = \bar{X}_{3b}(H^*, k^*) \cdot \hat{\beta}_{3b}(v^*, x^*, y^*, D^*) \tag{61}$$

Where $\tilde{y}(v^*, x^*, y^*, D^*, H^*, k^*)$ is the final interpolated result, and

$\bar{X}_{3b}(H^*, k^*)$ is the vector of predictor for the second part of step 3

$$\bar{X}_{3b}(H^*, k^*) = \left\{ 1 \;\; H^* \;\; H^{*2} \;\; \ln(k^*) \;\; H^* \ln(k^*) \;\; H^{*2} \ln(k^*) \;\; \frac{1}{k^*} \;\; \frac{H^*}{k^*} \;\; \frac{H^{*2}}{k^*} \right\} \tag{62}$$

Where H* is targeted aggregate base thickness,

k* is targeted modulus of subgrade reaction , and

$\hat{\beta}_{3b}(v^*, x^*, y^*, D^*)$ is the least-squares coefficient vector for the second part of step 3

$$\hat{\beta}_{3b}(v^*, x^*, y^*, D^*) = \left[X_{3b}{}^T \cdot X_{3b} \right]^{-1} \cdot X_{3b}{}^T \cdot \hat{Y}_{3b}(v^*, x^*, y^*, D^*) \tag{63}$$

$$X_{3b} = \begin{bmatrix} 1 \;\; H_1 \;\; H_1{}^2 \;\; \ln(k_1) \;\; H_1 \ln(k_1) \;\; H_1{}^2 \ln(k_1) \;\; \frac{1}{k_1} \;\; \frac{H_1}{k_1} \;\; \frac{H_1{}^2}{k_1} \\ 1 \;\; H_1 \;\; H_1{}^2 \;\; \ln(k_2) \;\; H_1 \ln(k_2) \;\; H_1{}^2 \ln(k_2) \;\; \frac{1}{k_2} \;\; \frac{H_1}{k_2} \;\; \frac{H_1{}^2}{k_2} \\ 1 \;\; H_1 \;\; H_1{}^2 \;\; \ln(k_3) \;\; H_1 \ln(k_3) \;\; H_1{}^2 \ln(k_3) \;\; \frac{1}{k_3} \;\; \frac{H_1}{k_3} \;\; \frac{H_1{}^2}{k_3} \\ \vdots \;\; \vdots \;\; \vdots \;\; \vdots \;\; \vdots \;\; \vdots \;\; \vdots \;\; \vdots \;\; \vdots \\ 1 \;\; H_3 \;\; H_3{}^2 \;\; \ln(k_3) \;\; H_3 \ln(k_3) \;\; H_3{}^2 \ln(k_3) \;\; \frac{1}{k_3} \;\; \frac{H_3}{k_3} \;\; \frac{H_3{}^2}{k_3} \end{bmatrix} \tag{64}$$

$$\hat{Y}_{3b}(v^*, x^*, y^*, D^*) = \begin{bmatrix} \tilde{y}(v^*, x^*, y^*, D^*, H_1, k_1) \\ \tilde{y}(v^*, x^*, y^*, D^*, H_1, k_2) \\ \tilde{y}(v^*, x^*, y^*, D^*, H_1, k_3) \\ \vdots \\ \tilde{y}(v^*, x^*, y^*, D^*, H_3, k_3) \end{bmatrix} \quad (65)$$

5.2 Interpretation of influence surfaces

The details of each step in the interpolation process presented in the previous section can be implemented with the aid of any mathematical software or spreadsheet program. As the influence field database has been developed via the finite element method, an influence surface plot can be generated by feeding the targeted variables into the formulations described above. Three typical influence surfaces are illustrated in Figures 40 (a) through (c) in contour plot format through the use of spreadsheet program.

It should be noted that the pavement system in this study contains three slabs, where the reference point is always located on the second slab. However, the three-slab system sufficiently covers the entire non-zero area on the surface; as illustrated in the figures, all general points appear to have zero values near both ends of the three-slab system. Furthermore, the responses on the plot are required to be normalized to the unit load 9,000 lb to quantify the response for each wheel load. Then, through superposition, the response due to the entire load configuration at the reference point can be calculated.

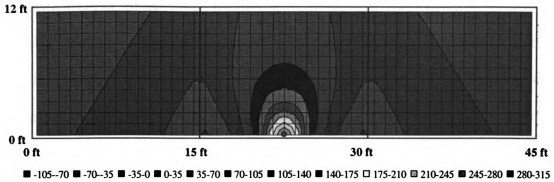

a) Reference point at 6 in.

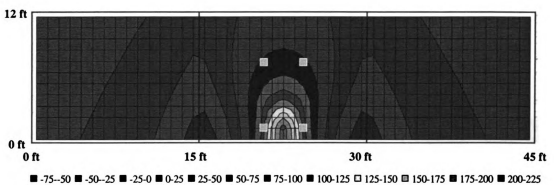

b) Reference point at 18 in.

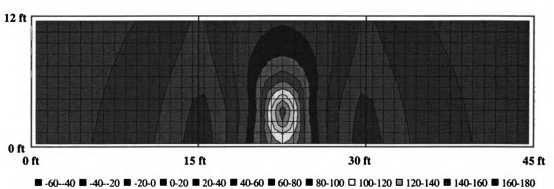

c) Reference point at 40 in.

Figure 40: Typical influence surfaces (in psi)

(Details: slab dimensions of 12 ft by 15 ft, slab thickness of 8 in., aggregate base thickness of 4 in., and modulus of subgrade reaction of 50 psi/in.)

5.3 Verification of the proposed technique

To validate the proposed technique, an extensive verification process is conducted involving a number of independent cases analyzed directly by the finite element method and then by the proposed technique of influence surface. Shown in Figure 41 is the multi-axle truck configuration used in the verification process. This truck is applied to a total of 14,850 combinations of slab dimensions, reference points, general points, and structural features. These are all features excluded from the experimental matrix.

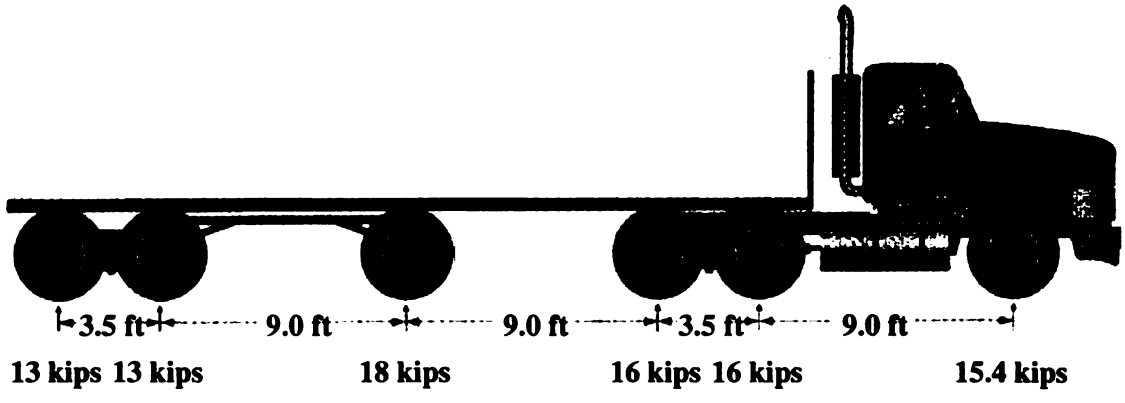

Figure 41: Multi-axle truck configuration used in the verification process

Goodness of fits

Comparing results of the two approaches (illustrated in Figure 42 (a)) generally suggests that the proposed technique can accurately and precisely quantify pavement stresses. Here we are comparing the proposed approach to the results obtained directly from the finite element method, which is also confirmed to have exceptionally low values of statistical fit indicators such as a mean of squares of error (MSE) of 0.303 psi^2, maximum error of 2.263 psi, and average absolute value of errors of 0.348 psi. More importantly,

the distribution of percent error in Figure 42 (b) illustrates the reliability of the results produced through the proposed approach. As can be seen, a majority of cases are associated with less than one percent of error and the maximum percent error observed is only 3.3 percent.

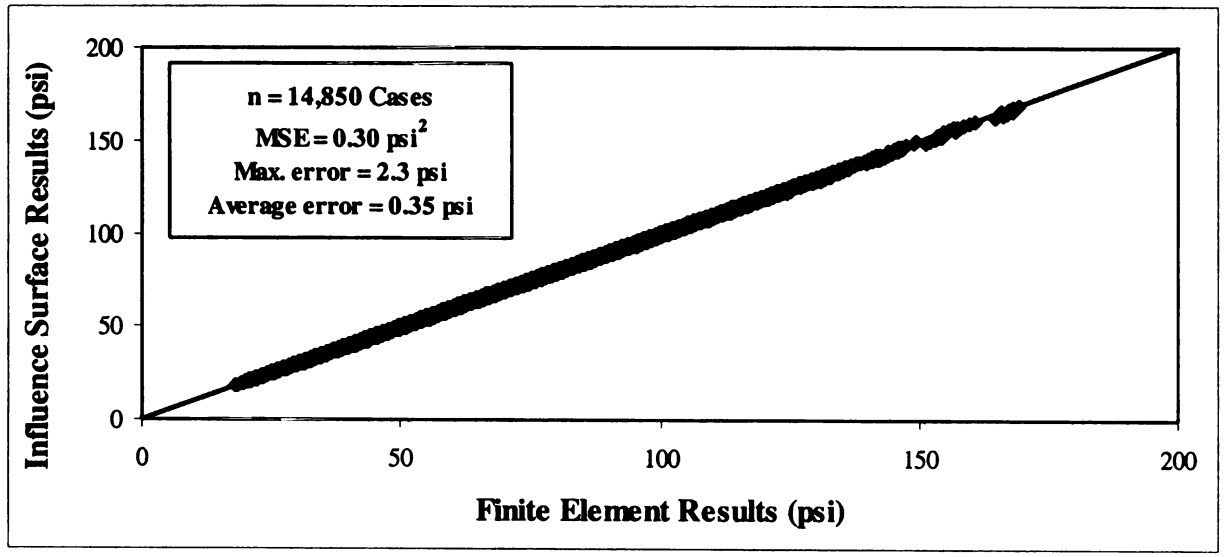

a) Comparison between interpolated results and finite element results

Figure 42: Verification results

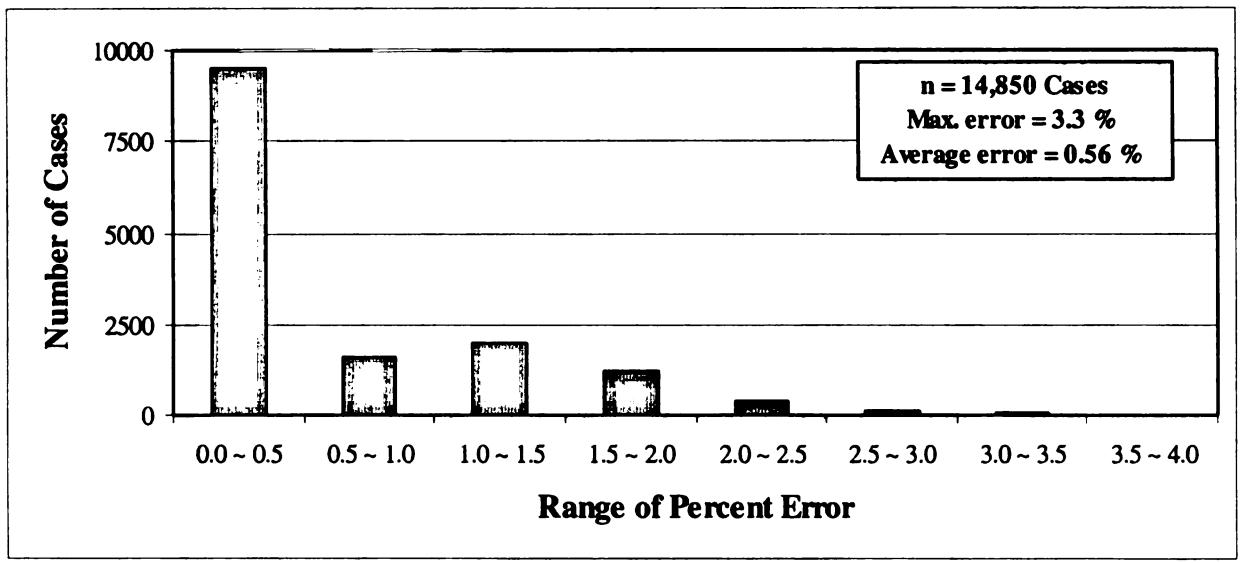

b) Percent error distribution

Figure 42: Verification results (continued)

Sources of errors

Through an analytical approach, the results obtained from influence surfaces should be identical to those obtained directly from the finite element method. However, for a numerical approach, such as the one proposed in this study, errors are naturally anticipated. Basically, since several assumptions have been made to accelerate and simplify the numerical process, calculation errors are the result of violations of the assumptions. The level of the errors depends on the degree of violation. As shown in the verification process, the level of errors appears to be acceptable; it is nevertheless important to future researchers to comprehend the sources of the errors.

One unavoidable assumption as a part the proposed approach is the unaddressed impact of tire contact pressure and aspect ratio. Deviations of both parameters away from the standard unit load used in the construction of influence surfaces, even within practical limits, violate the assumption and consequently result in errors. While this violation appears to have minimal consequences (as illustrated in Figure 39), it is still responsible for a significant portion of the overall half percent error. Another source of error comes from the use of power series in the interpolation process, on which the vectors of predictor X_1, X_2, and X_{3a} are based. A certain level of error is always associated with the use of power series, depending on the degree level of the series. As the fourth degree series was not found to substantially improve the interpolated results, the third degree series was chosen.

5.4 Potential applications

Like the finite element method, the influence surface technique has unlimited potential as a tool for the analysis and design of rigid pavements, but in a more time-efficient fashion. Thus, the use of the technique makes some of the most tedious tasks, if handled directly with finite element method, more effective and practical. To elaborate the potential applications of the proposed technique, the following four tasks in the field of rigid pavement study are performed using the influence surface technique: (i) rapid pavement stress calculation, (ii) determination of critical load location, (iii) pavement stress history, and (iv) investigation of interaction between load configuration and structural feature.

Rapid pavement stress calculation

Finite element analysis is a time-consuming approach to calculate pavement stresses, while the interpolated stresses can instantly be obtained via mathematical software or spreadsheet programming. The proposed approach is an attractive alternative to the finite element method.

To demonstrate the calculation process, a standard 32-kips tandem axle is placed on the influence surface shown in Figure 40 (b). The longitudinal stress values on the influence surface at each wheel load are 91.1 psi for the two wheels on the wheel path and 27.3 psi for the two wheels away from the wheel path. As the applied wheel loads are 8 kips apiece, the influence surface values are then normalized to the unit load, resulting in a value of 80.9 psi for the two wheels along the wheel path and 24.3 psi for the two wheels away from the wheel path. Note that these values are obtained through step 2 of the interpolation process, while the estimate values could also be obtained by reading

directly from the influence surface plot. Ultimately, via the superposition principle, it can be calculated that the response at the reference point due to the entire load configuration is 210.5 psi. In addition, it should also be noted that the use of the influence surface allows the pavements to be analyzed through more common mathematical software (e.g., MathCad®, Mathematica®, MATLAB®) or spreadsheet programs (e.g., Microsoft Excel®) at places where access to finite element software is not available.

Determination of critical load location

In general, for highway rigid pavements, stresses have a maximum value significantly lower than the concrete modulus of rupture. Therefore, unlike the design of bridge decks or airport pavements, where the design criteria is usually based on the worst case loading scenario, the design of highway rigid pavements for cracking prevention is based on load repetitions, which effect fatigue behavior. However, the worst loading scenario and the maximum value of pavement stress may become significant to the design of rigid pavements when actual wheel loads are much heavier. In such a situation, it is of interest to pavement engineers whether or not the pavement stresses exceed the modulus of rupture.

While the process to determine the critical load locations is time-consuming if done directly using the finite element method (Buch et al., 2004), they can be obtained almost instantaneously via the application of the proposed technique. Due to the swiftness of the influence surface technique in determining each pavement stress, with an extra line of loop command or macro applied to influence surfaces, pavement stresses for every load position required can be quantified in a short time frame. From the location

the driving axle approaches the pavement system to the location the last axle of the truck leaves the pavement system, critical load location is the load location corresponding to maximum stress. Based on the truck configuration in Figure 41, an example of the determination of critical load location is illustrated in Figure 43 for bottom-up stress at the reference point. While it is conventionally believed that the critical load location for bottom-up stress is the position where the heaviest axle is located at the reference point, this example proves that such general belief may not necessarily be true. The critical load location in this instance was found to be where the lighter tandem axle is located at the reference point. The impact of adjacent axles must be accounted for in the analysis, as it could either intensify or reduce the pavement stress at the reference point, depending on the spacing between axles and the length of the slab. In the same way, Figure 44 shows the determination of critical load location for top-down stress at the reference point.

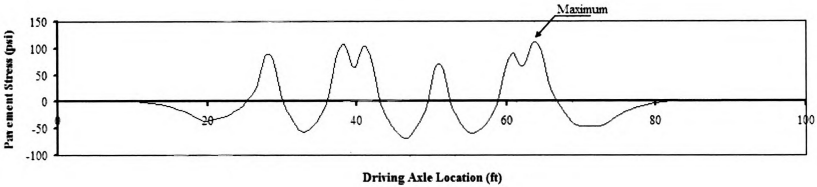

a) Pavement stresses at the reference point for various load locations

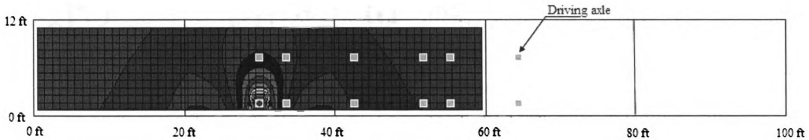

b) Critical load location

Figure 43: Typical determination of critical load location for bottom-up stress

(Details: longitudinal stress at the bottom of the slab (bottom-up stress), slab dimensions of 12 ft by 20 ft, slab thickness of 10 in., aggregate base thickness of 4 in., modulus of subgrade reaction of 100 psi/in., and reference point at 18 in.)

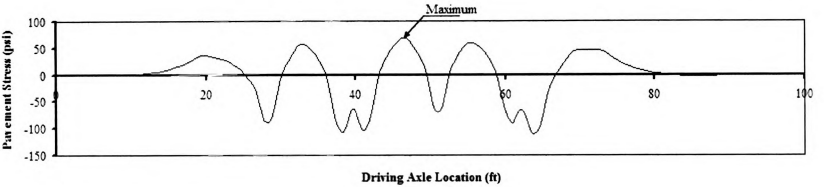

a) Pavement stresses at the reference point for various load locations

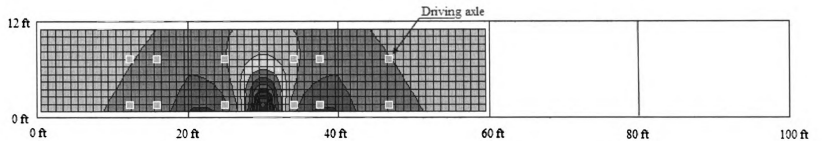

b) Critical load location

Figure 44: Typical determination of critical load location for top-down stress

(Details: longitudinal stress at the top of the slab (top-down stress), slab dimensions of 12 ft by 20 ft, slab thickness of 10 in., aggregate base thickness of 4 in., modulus of subgrade reaction of 100 psi/in., and reference point at 18 in.)

Pavement stress history

Addressed through Miner's hypothesis, the fatigue damage of rigid pavements is conventionally calculated based on moduli of rupture, peak stress values, and the number of associated repetitions. With the Weigh-in-Motion (WIM) data, pavement stress history can be provided via the proposed approach. For each truck configuration and its traveling speed imported from the WIM data into influence surface, pavement stress history can be presented in the same fashion as illustrated in Figures 43 (a) and 44 (a). The use of the proposed approach should have an advantage over considering each axle group and weight group separately. This is because the interaction from the adjacent axles is also addressed in the calculation. However, as WIM data do not generally contain the lateral placements of vehicles, additional study of vehicle wander may need to be conducted to obtain the proper y-coordinate of the general point for each truck wander and the appropriate reference point for the location of wheel path. Furthermore, in the future, once the fatigue analysis is improved to address the impacts of off-peak stress values and the sequence of the associated repetitions in the damage calculation, the use of the influence surface technique can be employed as a perfect fit to this puzzle.

To further elaborate this application of the influence surface technique, several pavement stress history plots were produced based on actual field data. The structural inputs were extracted from the Long-Term Pavement Performance (LTPP) Specific Pavement Study-2 (SPS-2) sections in Michigan. Constructed in 1993 along US-23 (N) near the Ohio-Michigan border, the experiment contains four sections with dense-graded aggregate base (DGAB), the same type of material as used in the developed influence surfaces. The inventory properties of the DGAB sections are shown in Table 11. The

other eight sections were not eligible in this demonstration as they were constructed with treated bases. Theoretically, this technique is applicable to all types of elastic base layer; however, it is not an objective of this study to capture the impact of all base types. Based on the LTPP database (Release 17), the backcalculated modulus of subgrade reaction has an average value of 225 and 300 psi/in. between May and June and between November and December, respectively.

Table 11: Inventory properties of the sections used in the demonstration

Inventory properties	Section			
	26-0213	26-0214	26-0215	26-0216
Lane width, ft	14	12	12	14
Slab length, ft	15	15	15	15
Dowel diameter, in.	1.25	1.25	1.50	1.50
Dowel spacing, in.	12	12	12	12
Slab thickness, in.	8.0	8.1	10.7	11.1
Base thickness, in.	6.1	5.8	6.2	5.9
Backcalculated slab elastic modulus, psi	5,570,000	5,030,000	5,480,000	5,360,000
Backcalculated base elastic modulus, psi	37,100	33,500	36,500	35,700

The main issues pertaining to applying the developed influence surfaces to the field data are the difference between the input values used in the influence surface analysis and the input values in actuality. These inputs are load transfer devices and layer elastic moduli. The SPS-2 sections employed both 1.25-in. and 1.5-in. dowel diameters, while only a 1.25-in. dowel diameter was addressed in the construction of the influence surfaces. The slab and base elastic moduli used in developing influence surfaces are 4,000 ksi and 30 ksi, respectively, different from the actual layer elastic moduli. Despite

the fact that the variations in load transfer device and layer elastic moduli were not included in the development of influence surfaces in this study, such variations insignificantly affect the pavement stress magnitudes. As reported in the MDOT study, the variations in load transfer device, while significantly affecting slab deflections adjacent to the transverse joint, were found to be insensitive to the pavement stress magnitudes near the midslab. Figures 45 (a) and (b) suggest that the variations in slab and base elastic moduli within reasonable ranges have an insignificant effect on the pavement stress magnitudes; only 5% change in stress magnitudes is contributed to the increase in slab elastic moduli from 4,000 to 6,000 ksi.

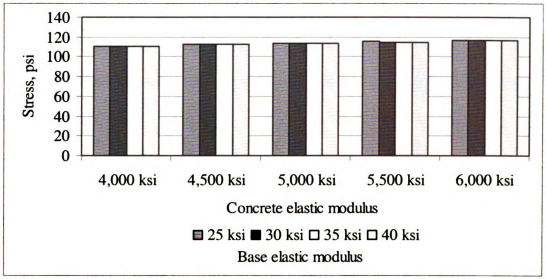

(a) Pavement stress magnitudes

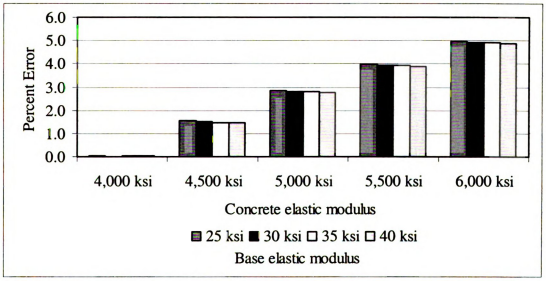

(b) Percent error as compared to those used in developing influence surfaces

Figure 45: Impact of variations in slab and base elastic moduli

(Details: 10-in. slab thickness, 6-in. aggregate base thickness, 100-psi/in. modulus of subgrade reaction, slab dimensions of 12 ft by 15 ft, 9-kips midslab loading)

Extracted from the WIM database at the SPS-2 site, the truck configuration shown in Figure 46 traveled through the WIM station between 8 pm and 9 pm of July 11, 2000 at the speed of 63 mi/hour. This truck was applied to the influence surfaces for this demonstration.

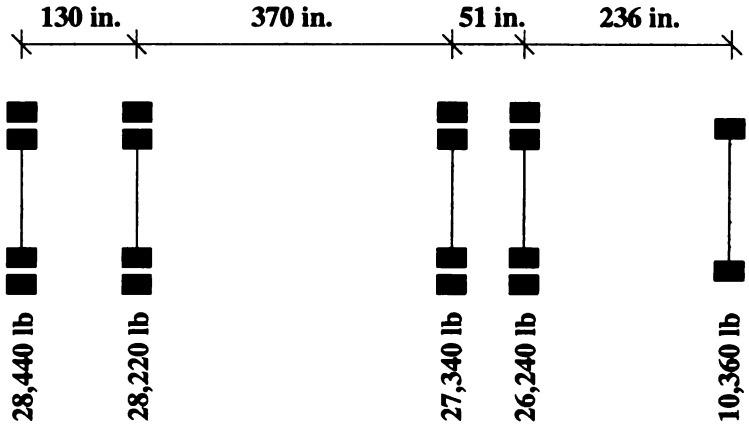

Figure 46: Typical truck configuration extracted from the WIM database

Based on the aforementioned parameters, Figure 47 illustrates the stress history plots, produced through the use of the influence surface technique. To account for the difference in the modulus of rupture between the sections, the pavement stress history plots were modified to the pavement stress ratio history plots as illustrated in Figure 48. Note that sections 26-0213 and 26-0215 have a targeted 550-psi for the 14-day modulus of rupture, while sections 26-0214 and 26-0216 have a targeted 900-psi for the 14-day modulus of rupture. Based on the testing results, the 365-day moduli of rupture were 915 psi for sections 26-0213 and 26-0215 and 1000 psi for section 26-0214, while the testing results were not available for section 26-0216. For the purpose of demonstration, the plots in Figure 48 employed the targeted moduli of rupture.

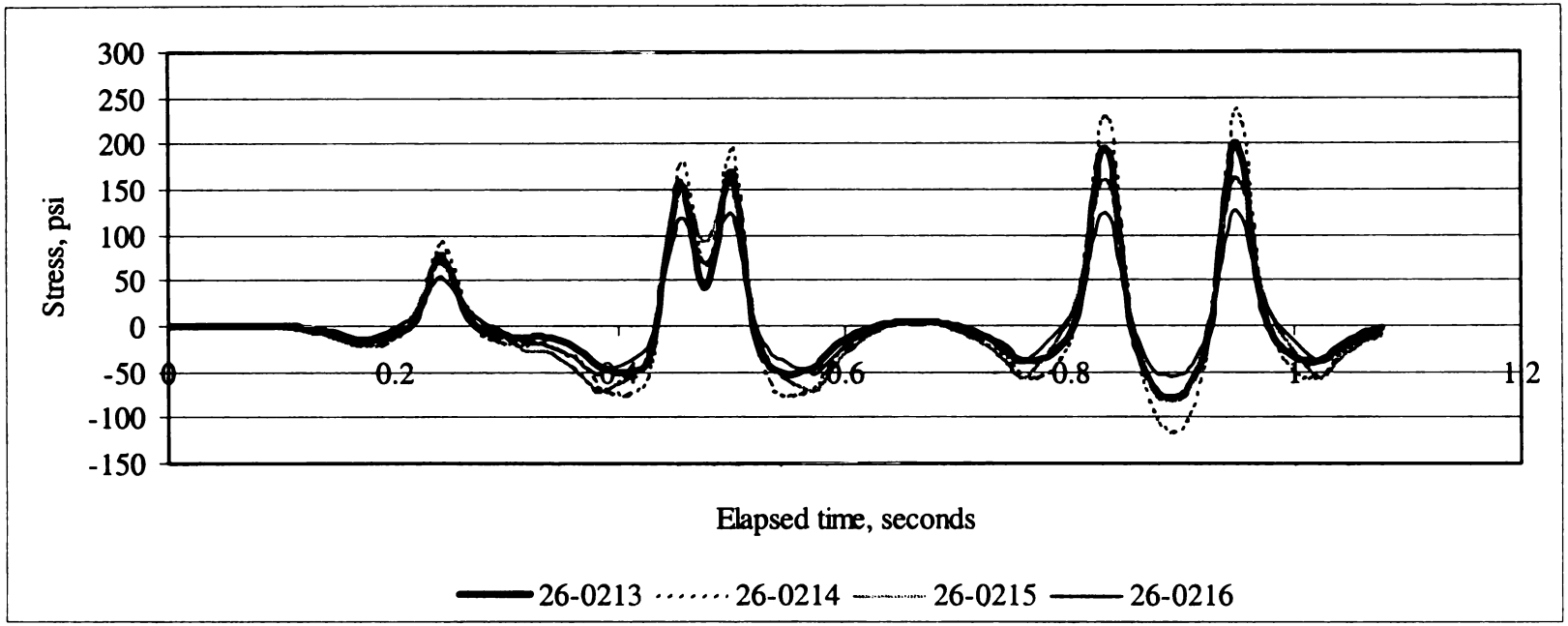

Figure 47: Pavement stress history plots for the DGAB sections

(Details: wheel paths located at 18 and 42 in. away from the longitudinal joint for 12-ft and 14-ft lane, respectively)

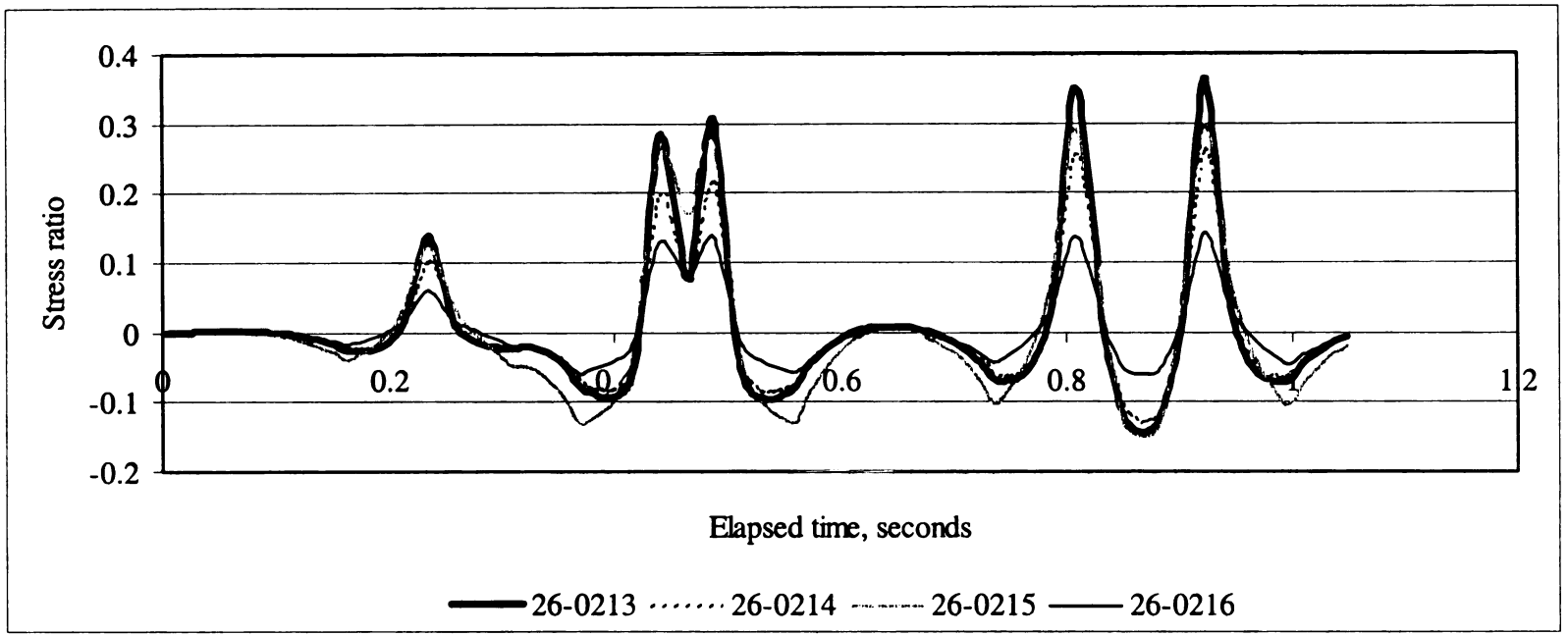

Figure 48: Stress ratio history plots for the DGAB sections

(Details: wheel paths located at 18 and 42 in. away from the longitudinal joint for 12-ft and 14-ft lane, respectively)

To translate the computed stress ratio into transverse cracking, application of the transfer function, such as the fatigue model suggested in NCHRP 1-37 A, was used to calculate fatigue damage due to the passing of this truck configuration as shown in Figure 49. Equation 66 is the fatigue model used in this demonstration (NCHRP, 2004). Note that the fatigue damage is the summation of the reciprocal of the allowable load repetitions (1/N) due to all peak stress ratios caused by the passing of the truck.

$$Log_{10}N = 2 \cdot R^{-1.22} + 0.4371 \quad (66)$$

Where N is the allowable load repetitions

R is the stress ratio

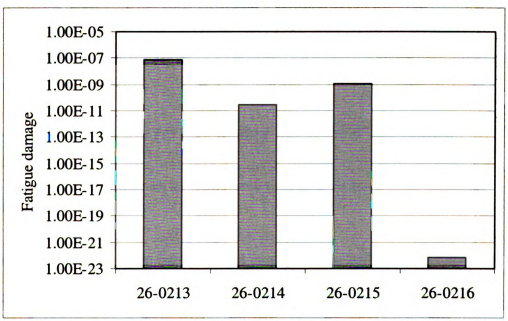

Figure 49: Fatigue damage based on peak stresses from influence surfaces

Figure 50 illustrates the time-series transverse cracking on the four DGAB section based on the LTPP database (Release 17). The 10-year distress data suggested that section 26-0216 remained free of transverse cracking, while section 26-0213 was the first section to exhibit transverse cracking, followed by sections 26-0215 and 26-0214, respectively. The trend of transverse cracking coincides with the trend observed in the calculated fatigue damage in Figure 49.

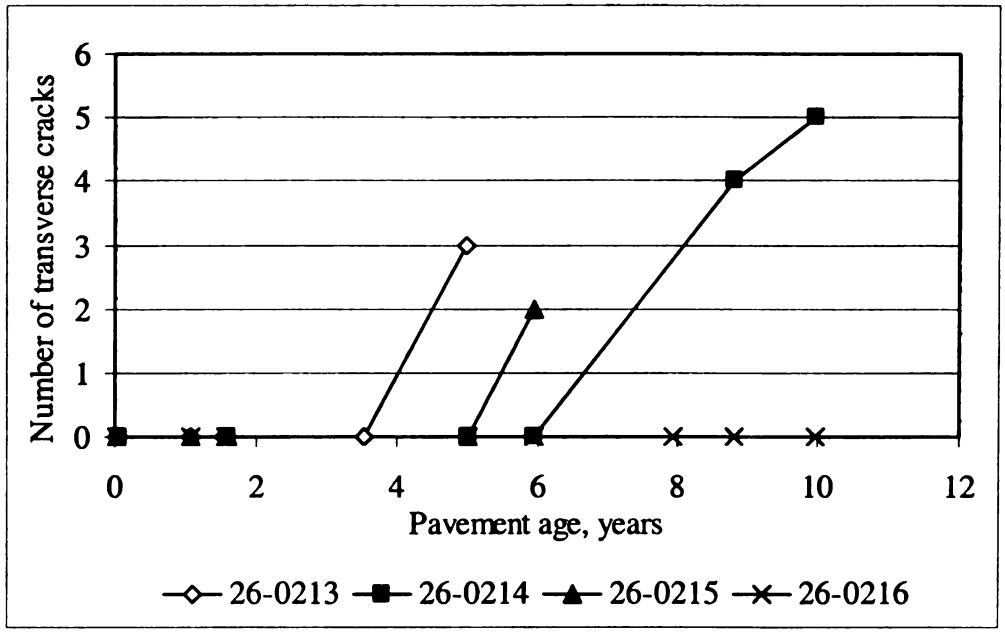

Figure 50: Time-series transverse cracking on the DGAB sections

Investigation of interaction between load configuration and pavement structure

The proposed technique can effectively be used as a tool to address the impact of the interaction between traffic load and pavement structure, such as the interaction between load configuration and slab length – a task requiring a strenuous effort if directly performed using the finite element method. The truck configuration in Figure 51

represents the typical image of a single unit truck, whose spacing between the load-carrying axles may vary substantially. As the axle spacing up to 25 ft has been documented in practice (Michigan Center for Truck Safety, 2001), this sensitivity study is conducted within a valid range.

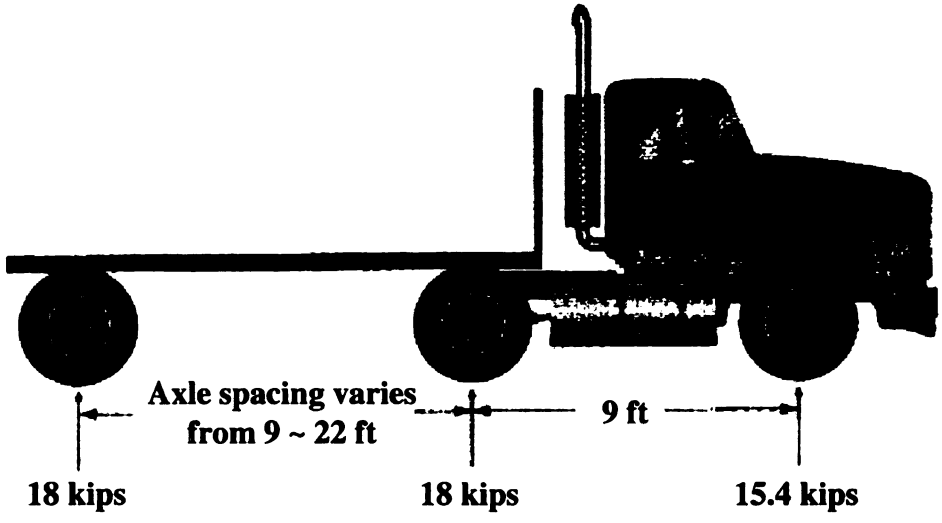

Figure 51: Single unit truck configuration used in the demonstration study

It is important to note that variation in critical load locations is part of the interaction, since the critical load locations are also affected by variations in axle spacing and slab length. In this demonstration, three slab lengths (15, 18, and 20 ft) and various axle spacing lengths ranging from 9 to 22 ft, in increments of 1 ft, are considered. Since the process of determining critical load locations can be accomplished in a short time frame using influence surfaces, repeating this process for all combinations of axle spacing lengths and slab lengths can be accomplished in a reasonable time frame.

The interaction impact between axle spacing and slab length for bottom-up stress at the reference point for the single unit truck configuration shown in Figure 51 is illustrated in Figure 52 (a). The results reveal that bottom-up stresses at the reference

point are intensified by an increase in axle spacing. The increase in axle spacing, after exceeding the slab length, however, appears to have only a marginal effect on the stress magnitude. The observed trend is explicable, when considering influence surface plot along with the corresponding critical load location, as shown in Figure 52 (b). The figure reveals that while one of the load-carrying axles of this particular truck configuration, placed at the reference point, has a positive impact on the bottom-stress, the other load-carrying axle would have a negative impact on the stress. It can be seen that the negative impact of the adjacent axle diminishes as the spacing between the two load-carrying axles begins to exceed the slab length.

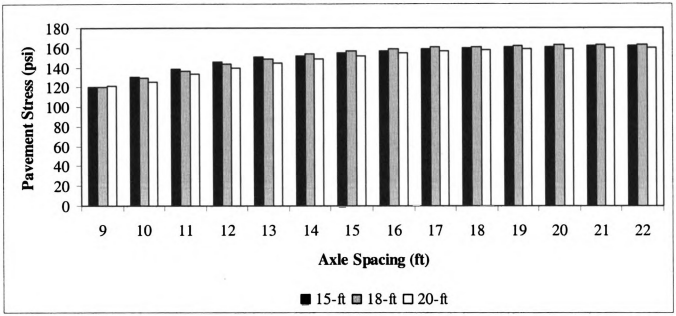

a) Impact of axle spacing and slab length on bottom-up stresses

Figure 52: Interaction between axle spacing and slab length on bottom-up stresses

(Details: longitudinal stress at the bottom of the slab (bottom-up stress), slab width of 12 ft, slab lengths of 15, 18, and 20 ft, slab thickness of 10 in., aggregate base thickness of 4 in., and modulus of subgrade reaction of 100 psi/in., and reference point at 18 in.)

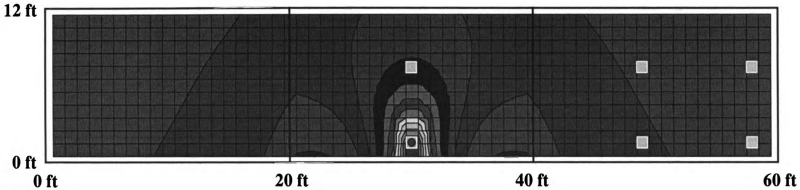

b) Combination of load location and axle spacing to maximize bottom-up stresses

Figure 52: Interaction between axle spacing and slab length on bottom-up stresses (continued)

(Details: longitudinal stress at the bottom of the slab (bottom-up stress), slab width of 12 ft, slab lengths of 15, 18, and 20 ft, slab thickness of 10 in., aggregate base thickness of 4 in., and modulus of subgrade reaction of 100 psi/in., and reference point at 18 in.)

Figure 53 (a) illustrates the impact of the interaction between axle spacing lengths and slab lengths for top-down stresses at the reference point when also considering the truck configuration shown in Figure 51. It can be seen that the top-down stresses reach their peak values when the axle spacing lengths near the corresponding slab lengths. The typical load location for top-down stress illustrated in Figure 53 (b) can be used to explain the observed trend. The figure shows that the critical load location for top-down stress concurs with the load location suggested in NCHRP 1-37-A where the two load-carrying axles are placed at each end of the slab (NCHRP, 2004). At these locations, the influence surface for top-down stress displays its highest values.

This limited-scope study suggests that for this particular truck configuration both bottom-up and top-down stresses reach peak values when axle spacing length is slightly shorter than slab length. While this finding may be useful to a study of the impact of the interaction between load configuration and pavement structure if applicable to all scenarios, it is solely limited to the particular truck configuration and the slab lengths considered in this study. However, more importantly, this study indicates that the use of the proposed technique offers a promising approach towards a detailed study to gain insight into the interaction between load configuration and structural features of rigid pavements.

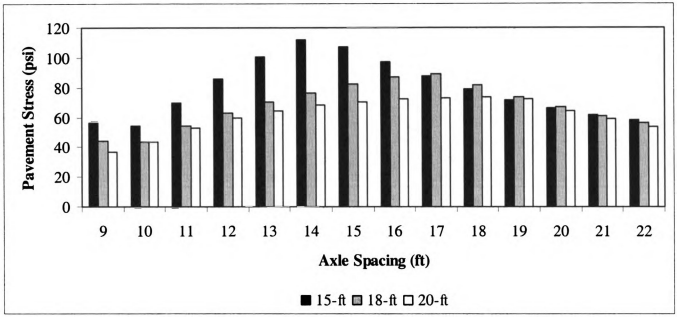

a) Impact of axle spacing and slab length on top-down stress

Figure 53: Interaction between axle spacing and slab length on top-down stresses

(Details: longitudinal stress at the top of the slab (top-down stress), slab width of 12 ft, slab lengths of 15, 18, and 20 ft, slab thickness of 10 in., aggregate base thickness of 4 in., and modulus of subgrade reaction of 100 psi/in., and reference point at 18 in.)

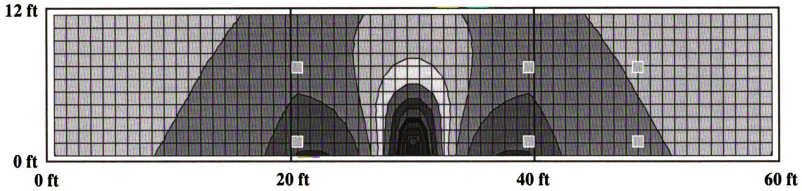

b) Combination of load location and axle spacing to maximize top-down stress

Figure 53: Interaction between axle spacing and slab length on top-down stresses (continued)

(Details: longitudinal stress at the top of the slab (top-down stress), slab width of 12 ft, slab lengths of 15, 18, and 20 ft, slab thickness of 10 in., aggregate base thickness of 4 in., and modulus of subgrade reaction of 100 psi/in., and reference point at 18 in.)

The influence surface technique is not generally used to address the impact of thermal gradient on stresses as temperature commonly affects the entire surface of structures. The impact of the interaction between slab length and axle spacing, shown in Figures 52 and 53, addresses the pavement stresses due to load only; therefore, the results disregard the interaction between slab length and temperature. Figure 54 illustrates the pavement stresses at the reference point due to temperature and the pavement weight for the same cases in this demonstration. It can be seen that the longer slab lengths results in higher thermal stress magnitudes in all cases, while this trend was not observed for the impact of the slab lengths on loading stress magnitudes. Figure 55 shows the combined loading and temperature stress magnitudes for this demonstration. The domination of the thermal gradient impact was observed in the figure. Note that a positive thermal strain gradient was used in the analysis for the bottom-up stresses, while a negative thermal strain gradient was used for the top-down stresses.

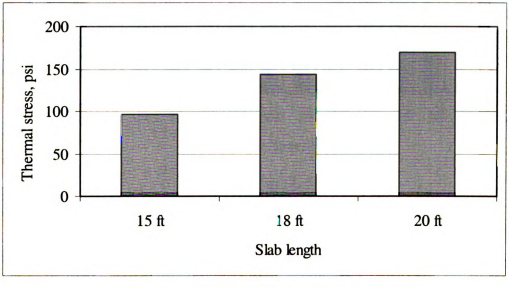

Figure 54: Impact of slab length on thermal stress

(Details: slab width of 12 ft, slab thickness of 10 in., aggregate base thickness of 4 in., and modulus of subgrade reaction of 100 psi/in., reference point at 18 in., thermal strain gradient of $10x10^{-6}$ $in.^{-1}$)

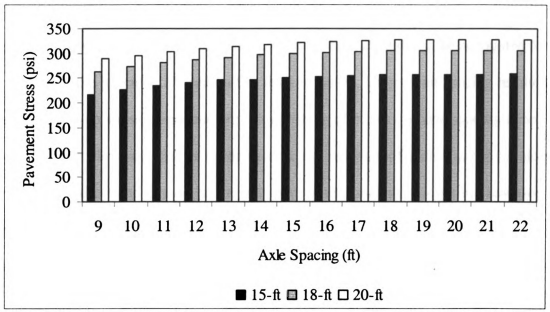

a) Bottom-up stress (thermal strain gradient of $+10x10^{-6}$ in.$^{-1}$)

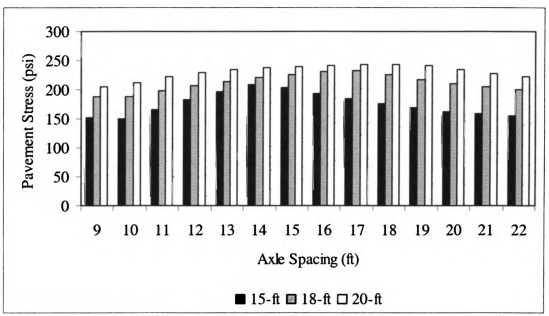

b) Top-down stress (thermal strain gradient of $-10x10^{-6}$ in.$^{-1}$)

Figure 55: Combined loading and thermal stresses

(Details: slab width of 12 ft, slab thickness of 10 in., aggregate base thickness of 4 in., and modulus of subgrade reaction of 100 psi/in., and reference point at 18 in.)

As the results from Figures 52 (a) and 53 (a) suggest that axle spacing has a significant impact on pavement stresses, the axle spacing should also be accounted for in the design of the pavement. Based on this demonstration, longer joint spacing resulted in higher bottom-up stress magnitude with diminishing effect as the axle spacing approach 15-16 ft. From the standpoint of loading stress, the selection of joint spacing should not significantly affect the design to prevent bottom-up cracking. However, selection of appropriate joint spacing should be a crucial part of the design to prevent top-down cracking. This is because the top-down stress magnitudes had their peak values when the length of axle spacing reaches the length of joint spacing. This should further warrant the necessity to synthesize the WIM database as this would also provide a source of axle spacing database to be considered during the selection of appropriate joint spacing.

CHAPTER VI

CONCLUSIONS, RESEARCH SIGNIFICANCE AND RECOMMENDATIONS

6.1 Conclusions

To gain an insight into the impact of various parameters and their interrelationship on mechanistic responses of rigid pavements, this dissertation had four primary objectives: to perform a parametric study on current and anticipated rigid pavements, with considerations of loading, climatic, material, subgrade support, and construction parameters, to establish a protocol for the development of a comprehensive interpolation scheme that addresses the condition changes into mechanistic responses, to develop influence surfaces for rigid pavements to address the impact of complex load configurations on pavement responses and also the impact of lateral wander, and to investigate the impact of the interaction between structural, environmental, and loading factors on mechanistic responses. To systematically accomplish these objectives and to provide a better understanding of each phase of the study, the research plan was divided into three major tasks: performing of a parametric study, development of an interpolation scheme, and application of an influence surface.

1. By conducting a parametric study based on a complete factorial experimental matrix, the impact of the interaction between structural, environmental, and loading factors over mechanistic responses of rigid pavements was thoroughly investigated. The experimental matrix for the parametric study was constructed based on the data collected from three sources: the current-practice designs of rigid pavement structure, field thermal gradients, and actual Michigan multi-axle truck configurations. Based

on the results from a preliminary sensitivity study, several strategies were employed to reduce the size of the experimental matrix to 43,096 finite element runs, a practical number, without sacrificing to the quality of final results. These strategies include (i) combining base and subbase layers into one layer, (ii) merging thermal gradient and coefficient of thermal expansion into a thermal strain gradient, (iii) discarding the unfamiliar truck configurations, and (iv) selecting appropriate intervals for non-discrete variables. Additionally, to conduct a finite element analysis, the parametric study also requires the derivation of the critical load locations of the load configurations, not supplied by the experimental matrix. The critical load location is defined by the load location along the wheel path that results in the most critical mechanistic response. A time-consuming process, the procedure of determining a critical load location was not practical to repeat for all combinations of inputs in the experimental matrix. Hypothesized as non-influential variables to the critical load location, five variables, including slab thickness, base/subbase thickness, modulus of subgrade reaction, lateral support condition, and thermal strain gradient, were tested based on a fractional factorial design of $\frac{1}{3^3} \cdot 3^5 = 9$; these variables were found to have a significant impact on the pavement stress magnitudes but appeared to be inconsequential to the critical load location. The critical load location is influenced only by joint spacing and truck or axle configuration.

2. Based on the parametric study results, it was found that a change in slab thickness from 9 to 12 in. resulted in a reduction in stress by approximately 35% for a flat slab condition. In spite of a constant thermal strain gradient, pavements constructed with different slab thicknesses will not have a constant temperature differential, and

therefore, the impact of slab thickness on pavement responses, in such a case, could not be compared. A change in base/subbase thickness from 4 to 26 in. was found to result in about 5-30% lower stresses for a flat slab condition; as the slab thickness increases, the impact of base/subbase thickness was found to become less significant. Pavements with 27 feet joint spacing resulted in about 33% higher longitudinal stresses as compared to pavements with 15 feet joint spacing for curled slab conditions at a thermal strain gradient value of $+10 \times 10^{-6}$ in.$^{-1}$. The severity depends on the level of thermal curling or thermal strain gradient. For the load located along the wheel path, pavements constructed with tied-concrete shoulders resulted in the lowest stresses among the three lateral support conditions considered in the study. Although the pavements were constructed with the same untied-asphalt shoulder, the magnitudes of longitudinal stresses for pavements with a 12-ft lane (standard lane) were higher than that for pavements with a 14-ft lane (widened lane). As the wheel path shifted 2 ft towards the centerline for pavements with a widened lane, a pseudo-interior loading condition was created, resulting in the reduction of stresses from edge loading. Pavements with an untied-asphalt shoulders (12-ft lane) resulted in about 13% and 9% higher longitudinal stress values than pavements constructed with a tied-concrete shoulder (12-ft lane) and widened lane (14-ft lane with an untied-asphalt shoulder), respectively. Lateral placement of traffic load resulted in about 10% and 30% higher edge stresses as the load moves from the wheel path towards the longitudinal joint (lane/shoulder joint) for a tied-concrete shoulder and an untied-asphalt shoulder, respectively.

3. In this study, an interpolation scheme was used to obtain mechanistic responses for all the combinations of the non-discrete inputs, excluded from the final experimental matrix. Via the least-squares criteria, several interpolation schemes were created with various forms of prediction vectors. With more than 12,000 independent finite element runs (cases not addressed in the experimental matrix), three stages of a validation process suggested that "Scheme 16" was the best performing scheme. This scheme contains the natural logarithm of the modulus of subgrade reaction and the interaction terms with the base/subbase thickness, similar to the terms suggested in the Westergaard's closed form stress equations.

4. When including all axle types, the bias, variance, and MSE were 0.51 psi, 8.63 psi^2, and 8.89 psi^2, respectively, indicating that the interpolation scheme was highly accurate and precise in quantifying pavement responses matching with the direct finite element results. If considering only the three major axle groups (single, tandem, and tridem), the bias, variance, and MSE were found to be 0.02 psi, 3.38 psi^2, and 3.38 psi^2, respectively, an even more promising performance.

5. Due to its swiftness and accuracy in quantifying pavement responses, the use of interpolation scheme offers an attractive alternative for the analysis of rigid pavements. With a limited number of load configurations included in the experimental matrix, the developed interpolation scheme faces a critical issue of the inability to address the variations in axle spacing and axle weight within the load configurations, deviating from the configurations specified in the experimental

matrix. Extension of the interpolation scheme ability to effectively and efficiently address such an issue was achieved in study through the influence surface technique.

6. The last part of the dissertation demonstrated that influence surfaces for rigid pavements can be developed successfully through a numerical process based on a series of finite element analyses and the multi-dimensional interpolation process. While only a limited number of finite element results are required for the combinations of anchor levels of each non-discrete variable in the interpolation process, the influence surfaces can be applied to an unlimited combination of structural features and loading scenarios through the application of multi-dimensional interpolation schemes. The details of each step in the interpolation process are presented in a format that can be implemented with the aid of any mathematical software or spreadsheet program. Confidence in the proposed approach was gained through an extensive verification process. A number of independent cases were analyzed directly by the finite element method and then by the proposed influence surface technique.
7. Based on more than 14,000 independent finite element runs, the verification results suggest that the influence surfaces can precisely and accurately quantify pavement stresses as compared to the results directly obtained from the finite element method. Versatilities of the influence surface technique for rigid pavements include, but are not limited to, rapid pavement stress calculation, determination of critical load location, pavement stress history, and investigation of the interaction between load configuration and structural feature. The use of this technique is clearly more effective and practical than the direct application of the finite element method.

6.2 Research significance

1. Strategies used in this research to reduce the size of the experimental matrix are useful for future researchers.
2. This study introduced of the multi-dimensional interpolation scheme technique to rigid pavement analysis.
3. The extensive trends observed in the parametric study better the understanding of the interaction between structural, environmental, and loading factors on pavement responses.
    a. The increase in base/subbase thickness results in a reduction in stress magnitude with diminishing effect as the slab thickness increases. As the base/subbase layer provides uniformity of support to the slab, an increase in base/subbase thickness reduces the magnitude of loading stress. The results suggest that from the loading stress standpoint the base/subbase thickness should also have a substantial effect on slab cracking for a pavement system with a thin slab, especially thinner than 10 in. However, the results should not suggest that the base/subbase thickness has a less significant impact for a pavement system with a thicker slab, since the base/subbase layer could also affect the drainage characteristic of the pavement system.
    b. AC shoulder results in the highest stress magnitude as compared to PCC shoulder and widened lane. This could imply that from the standpoint of load-related distress a pavement system with PCC shoulder or widened

lane should have a better performance than a pavement system with AC shoulder.

c. Lateral load location directly affects the magnitude of pavement stress for all types of lateral support condition. The results also imply the significance of the location of traffic paint stripe as it would dictate the location of wheel path.

d. While lateral support condition has a significant effect on loading stress magnitude, its effect on thermal stress magnitude appears to be insignificant as shown in the figure. This implies that the variation in lateral support condition should not affect temperature-related performance of the pavement.

e. An increase in the magnitude of modulus of subgrade reaction results in a reduction in stress magnitude with diminishing effect as the slab thickness increases. The results suggest that from the loading stress standpoint the modulus of subgrade reaction should also have a substantial effect on slab cracking for a pavement system with a thin slab, especially thinner than 10 in.

f. An increase in the magnitude of modulus of subgrade reaction results in an increase in the magnitude of thermal stress as the combined stress magnitudes are compared to the loading stress magnitudes. From the mechanistic standpoint, this could imply that a roadbed with higher modulus of subgrade reaction should result in a better load-related performance but not for a temperature-related performance. However, the

mechanistic behavior alone may not sufficiently provide such a conclusion to the actual performance of the pavement, since a roadbed with higher modulus of subgrade reaction usually also has a better erodibility resistance and also a better drainage characteristic.

g. From the loading stress standpoint joint spacing should not have a significant effect on load-related performance of the pavement. As stated by the Portland Cement Association's thickness-design procedure, the presence of joints has no effect on the pavement stress magnitude, since the load is placed adjacent to the midslab away from the joints. However, it should be noted that the results did not account for the interaction between axle spacing and joint spacing.

h. When combined with thermal stress, an interactive effect between thermal strain gradient and joint spacing on combined loading and thermal stress was observed. This implies that an increase in joint spacing should result in a higher level of temperature-related distress.

i. The results suggest that a more complex axle group should result in a lower pavement stress magnitude. However, the results did not account for the interaction between axle spacing and joint spacing.

4. The numerical approach to the influence surface technique was proposed in this study along with the detailed formulations, which can be further studied by future research.

5. The influence surface technique can effectively and efficiently address several aspects of the loading factors, including axle weight, axle spacing, lateral placement, and critical load location.

6. The influence surface technique offers an effective approach to determine critical locations for complex truck configurations.
7. Pavement stress history can be produced using the influence surface technique in a short time frame. The pavement stress history can be used as the inputs to transfer function to predict pavement performance.

6.3 Recommendations for future research

This research study focuses on pavement responses and several factors that affect them. Although pavement response plays a significant role in the mechanistic-empirical design process, it is necessary to integrate the pavement responses with several other components in order for it to become practical. Pavement responses need to be used as inputs to transfer function, which relate responses to performance. However, the transfer function coefficients need to be localized and therefore it is important to ensure the constants reflect the local climatic and loading conditions. The calibration process also needs to take place to ensure the quality in the calculation process. The following research topics are recommended: WIM data synthesis, development and calibration of transfer functions, and cataloging of coefficient of thermal expansion.

An extensive traffic database, e.g. a WIM database, should be synthesized and made available for the pavement network as hourly axle spectra is a key input for damage computations. The hourly axle spectra allow for calculation of pavement responses that account for daily and seasonal conditions of climate, roadbed and material. The axle repetitions from the axle spectra and the corresponding pavement responses are the inputs to the cumulative damage calculation.

Along with the WIM synthesis, the study of the traffic lateral placement should also be conducted. To eliminate the assumption of load only being placed at the wheel path, the study will provide appropriate values of lateral wander or y-coordinate in the analysis of rigid pavements using the influence surface technique.

Development and calibration of transfer functions should be conducted for key rigid pavement distresses that reflect the engineering practice. The process involves statistical correlation of the cumulative damage to the measured distresses to obtain a calibrated model that can be used for current rigid pavement designs.

Lastly, the coefficient of thermal expansion values for concrete mixes and also aggregate (as concrete making material) used in paving need to be determined and cataloged, since coefficient of thermal expansion plays a critical role in the thermal analysis of jointed concrete pavements. The slab movement and joint opening are also influenced by coefficient of thermal expansion of concrete.

BIBLIOGRAPHY

Altoubat, S.A. Early age stresses and creep-shrinkage interaction of restrained concrete, Ph.D. Thesis, University of Illinois at Urbana-Champaign, Champaign, IL, USA, 1999.

American Association of State Highway and Transportation Officials (AASHTO). AASHTO guide for design of pavement structures. Washington, DC, USA, 1993.

American Association of State Highway and Transportation Officials (AASHTO). Supplement to the guide for design of pavement structures. Washington, DC, USA, 1998.

Armaghani, J.M; Larsen, T.J; Smith, L.L. Temperature response of concrete pavements. Transportation Research Record 1121, TRB, National Research Council, Washington, DC, USA, 1987, pp. 23-33.

Bhatti, M.A.; Molinas V.I.; Stoner, J.W., Nonlinear analysis of jointed concrete pavements. Transportation Research Record 1629, TRB, National Research Council, Washington, DC, USA, 1998, pp. 50-57.

Bodocsi, A.; Minkarah, I.A.; Arudi, R.S.; Bhupalam, M.; Kak, A. Effect of pavement variables on average joint deflections in experimental concrete pavement. Transportation Research Record 1449, TRB, National Research Council, Washington, DC, USA, 1994, pp. 182-188.

Boresi, A.P.; Schmidt, R.J. Advanced mechanics of materials 6th Ed. John Wiley & Sons, New York, NY, USA, 2002.

Buch, N.; Vongchusiri, K.; Gilliland, D.; Van Dam, T. A preliminary mechanistic evaluation of PCC cross-sections using ISLAB2000 - A parametric study. Final Report, RC-1441, Michigan Department of Transportation, Lansing, MI, USA, 2004.

Byrum, C.R. Analysis of LTPP JCP slab curvatures using high speed profiles. 79th Annual Meeting of TRB, National Research Council, Washington, DC, USA, 2000.

Byrum, C.R.; Hansen, W., Influence function approach to analysis of jointed portland cement concrete pavement. Transportation Research Record 1449, TRB, National Research Council, Washington, DC, USA, 1994, pp. 148-158.

Ceylan, H.; Tutumluer, E.; Barenberg, E.J., Artificial neural networks for analyzing concrete airfield pavements serving the Boeing B-777 aircraft. Transportation Research Record 1684, TRB, National Research Council, Washington, DC, USA, 1999, pp. 110-117.

Channakeshava, C.; Barzegar, F.; Voyiadjis, G.Z. Nonlinear FE analysis of plain concrete pavements with doweled joints. Journal of Transportation Engineering, v 119, n 5, American Society of Civil Engineers, New York, NY, USA, 1993, pp. 763-781.

Chatti, K. Dynamic analysis of jointed concrete pavements subjected to moving transient loads. Ph.D. Dissertation. University of California, Berkeley, CA, USA, 1992.

Chatti, K.; Lysmer, J.; Monismith, C.L., Dynamic finite-element analysis of jointed concrete pavements. Transportation Research Record 1449, TRB, National Research Council, Washington, DC, USA, 1994, pp. 79-90.

Chou, Y.T. Estimating load transfer from measured joint efficiency in concrete pavements. Transportation Research Record 1482, TRB, National Research Council, Washington, DC, USA, 1995, pp. 19-25.

Chou, Y.T. Subgrade contact pressures under rigid pavements. Journal of Transportation Engineering, v 109, n 3, American Society of Civil Engineers, New York, NY, USA, 1983, pp. 363-379.

Chou, Y.T.; Huang, Y.H. A computer program for slabs with discontinuities on layered elastic solids. Proceedings of the 2nd International Conference on Concrete Pavement Design, Purdue University, West Lafayette, IN, USA, 1981, pp. 78-85.

Cifuentes, A.; Paz, M. Note on the determination of influence lines and surfaces using finite elements. Finite Elements in Analysis and Design, v 7, n 4, Elsevier, New York, NY, USA, 1991, pp. 299-305.

Cook, R.D; Malkus, D.S; Plesha, M.E. Concepts and applications of finite element analysis 3rd Edition. John Wiley & Sons, New York, NY, USA, 1989.

Crovetti, J. A.; Darter, M. I. Void detection for jointed concrete pavements. Transportation Research Record 1041, TRB, National Research Council, Washington, DC, USA, 1985, pp. 59-68.

Crovetti, J.A.; Tirado-Crovetti, M.R. Evaluation of support conditions under jointed concrete pavement slabs. ASTM Special Technical Publication, n 1198, ASTM, Philadelphia, PA, USA, 1994, pp. 455-472.

Darter, M.I; Hall, K.T; Kuo, C. Support under concrete pavements. University of Illinois, Champaign, IL, USA, 1994.

Darter, M; Khazanovich, L; Snyder, M; Rao, S; Hallin, J. Development and calibration of a mechanic design procedure for jointed plain concrete pavements. 7th International Conference on Concrete Pavements, Orlando, FL, USA, 2001.

Davids, W.G. Effect of dowel looseness on response of jointed concrete pavements. Journal of Transportation Engineering, v 126, n 1, American Society of Civil Engineers, New York, NY, USA, 2000, pp. 50-57.

Davids, W.G. Foundation modeling for jointed concrete pavements. 79th Annual Meeting of TRB, National Research Council, Washington, DC, USA, 2000.

Davids, W.G. Modeling of rigid pavements: joint shear transfer mechanisms and finite element solution strategies. Ph.D. Dissertation, University of Washington, Seattle, WA, USA, 1998.

Davids, W.G.; Mahoney, J.P. Experimental verification of rigid pavement joint load transfer modeling with EverFe. Transportation Research Record 1684, TRB, National Research Council, Washington, DC, USA, 1999, pp. 81-89.

Davids, W.G.; Mahoney, J.P. Experimental verification of rigid pavement joint load transfer modeling with EverFE. Transportation Research Record, n. 1684, 1999, pp. 11-19.

Dowling, P.J.; Bawa, A.S. Influence surfaces for orthotropic steel bridge decks. Proceedings of the Institution of Civil Engineers (London). Part 1 – Design & Construction, v. 59, n. 2, 1975, pp. 149-168.

Eisenmann, J; Leykauf, G. Effect of paving temperatures on pavement performance. 2nd International Workshop on the Theoretical Design of Concrete Pavements, Siquenza, Spain, 1990.

Eisenmann, J; Leykauf, G. Simplified calculation method of slab curling caused by surface shrinkage. 2nd International Workshop on the Theoretical Design of Concrete Pavements, Siquenza, Spain, 1990.

Fang, W. Environmental influences on warping and curling of PCC pavement. 7th International Conference on Concrete Pavements, Orlando, FL, USA, 2001.

Faraggi, V.; Jofre, C.; Kraemer, C. Combined effect of traffic loads and thermal gradients on concrete pavement design. Transportation Research Record 1136, TRB, National Research Council, Washington, DC, USA, 1987, pp. 108-118.

Fisher, R.A. Design of experiments. 7th Edition, Hafner Publication, New York, NY, USA, 1960.

Guo, H.; Sherwood, J.A.; Snyder, M.B. Component dowel-bar model for load-transfer systems in PCC pavements. Journal of Transportation Engineering, v 121, n 3, American Society of Civil Engineers, New York, NY, USA, 1995, pp. 289-298.

Hall, K.T; Darter, M.I; Kuo, C. Improved methods for selection of k value for concrete pavement design. Transportation Research Record 1505, TRB, National Research Council, Washington, DC, USA, 1995, pp. 128-136.

Hansen, W.; Smiley, D.L.; Peng, Y.; Jensen, E.A., Validating top-down premature transverse slab cracking in jointed plain concrete pavement. Transportation

Research Record 1809, TRB, National Research Council, Washington, DC, USA, 2002, pp. 52-59.

Heath, A.C.; Roesler, J.R. Top-down cracking of rigid pavements constructed with fast-setting hydraulic cement concrete. Transportation Research Record 1712, TRB, National Research Council, Washington, DC, USA, 2000, pp. 3-12.

Heath, A.C; Roesler, J.R; Harvey, J.T. Quantifying longitudinal, corner and transverse cracking in jointed concrete pavements. 80th Annual Meeting of TRB, National Research Council, Washington, DC, USA, 2001.

Hencky, H. Der spannungszustand in rechteckigen platten. Verlag Oldenburg, München und Berlin, 1913.

Hiller, J.E.; Roesler, J.R. Transverse joint analysis for mechanistic-empirical design of rigid pavements. Transportation Research Record 1809, TRB, National Research Council, Washington, DC, USA, 2002, pp. 42-51.

Hosur, V.; Bhavikatti, S.S. Influence lines for bending moments in beams on elastic foundations. Computers and Structures, v 58, n 6, Pergamon Press, New York, NY, USA, 1996, pp. 1225-1231.

Huang, Y.H. Pavement analysis and design. Prentice-Hall, Englewood, NJ, USA, 1993.

Huang, Y.H.; Wang, S.T. Finite-element analysis of concrete slabs and its implications for rigid pavement design. Highway Research Record, n. 466, Washington, DC, USA, 1973, pp. 55-69.

Imbsen, R.A.; Schamber, R.A. Influence surface approach to determine wheel load distribution factors for rating highway bridges. Canadian Society for Civil Engineering, v. 2, 1982, pp. 273-287.

Ioannides, A.M.; Alexander, D.R.; Hammons, M.I.; Davis, C.M., Application of artificial neural networks to concrete pavement joint evaluation. Transportation Research Record 1540, TRB, National Research Council, Washington, DC, USA, 1996, pp. 56-64.

Ioannides, A.M.; Davis, C.M.; Weber, C.M. Westergaard curling solution reconsidered. Transportation Research Record 1684, TRB, National Research Council, Washington, DC, USA, 1999, pp. 61-70.

Ioannides, A.M.; Hammons, M.I. Westergaard-type solution for edge load transfer problem. Transportation Research Record 1525, TRB, National Research Council, Washington, DC, USA, 1996, pp. 28-34.

Ioannides, A.M.; Korovesis, G.T. Analysis and design of doweled slab-on-grade pavement systems. Journal of Transportation Engineering, v 118, n 6, American Society of Civil Engineers, New York, NY, USA, 1992, pp. 745-768.

Ioannides, A.M.; Salsilli, M., Ricardo A. Temperature curling in rigid pavements. An application of dimensional analysis. Transportation Research Record 1227, TRB, National Research Council, Washington, DC, USA, 1989, pp. 1-11.

Ioannides, A.M.; Thompson, M.R.; Barenberg, E.J. Westergaard solutions reconsidered. Transportation Research Record 1043, TRB, National Research Council, Washington, DC, USA, 1985, pp. 13-23.

Janssen, D.J. Moisture in Portland Cement Concrete. Transportation Research Record 1121, TRB, National Research Council, Washington, DC, USA, 1987, pp. 40-44.

Janssen, D.J.; Snyder, M.B. Temperature-Moment Concept for Evaluating Pavement Temperature Data. Journal of Infrastructure System, v. 6, n. 2, 2000, pp. 81-83.

Jiang, Y.J.; Tayabji, S.D. Mechanistic evaluation of test data from long-term pavement performance jointed plain concrete pavement test sections. Transportation Research Record 1629, TRB, National Research Council, Washington, DC, USA, 1998, pp. 32-40.

Kawama, I.; Horikawa, T.; Sonoda, K. Influence surfaces for reactive forces of bridge-type skew slabs. Journal of Civil Engineering Design, v. 2, n. 2, 1980, pp. 103-120.

Khazanovich, L.; Yu, H.T. Modeling of jointed plain concrete pavement fatigue cracking in PaveSpec 3.0. Transportation Research Record 1778, TRB, National Research Council, Washington, DC, USA, 2001, pp. 33-42.

Khazanovich, L; Ioannides, A.M. Finite element analysis of slabs-on-grade using higher order subgrade soil models. Proceedings of the Conference on Airport Pavement Innovations, Vicksburg, MS, USA, 1993.

Krauthammer, T.; Khanlarzadeh, H. Numerical assessment of pavement test sections. Transportation Research Record 1117, TRB, National Research Council, Washington, DC, USA, 1987, pp. 66-75.

Krauthammer, T.; Western, K.L. Joint shear transfer effects on pavement behavior. Journal of Transportation Engineering, v 114, n 5, American Society of Civil Engineers, New York, NY, USA, 1988, pp. 505-529.

Kuo, C.M.; Hall, K.T.; Darter, M.I. Three-dimensional finite element model for analysis of concrete pavement support. Transportation Research Record 1505, TRB, National Research Council, Washington, DC, USA, 1995, pp. 119-127.

Lansdown, A.M. Use of influence surfaces in assessing moments and stresses in short span bridges subjected to abnormally heavy loads. Engineering Journal, v. 49, n. 6, 1966, pp. 18-21.

Lee, D.Y.; Klaiber, F.W.; Coleman, J.W. Fatigue behavior of air-entrained concrete. Transportation Research Record 671, TRB, National Research Council, Washington, DC, USA, 1978, pp. 20-23.

Lee, Y.H.; Darter, M.I. Mechanistic design models of loading and curling in concrete pavements. Proceedings of the Conference on Airport Pavement Innovations, American Society of Civil Engineers, New York, NY, USA, 1993, pp. 1-5.

Lee, Y.H.; Darter, M.I., Loading and curling stress models for concrete pavement design. Transportation Research Record 1449, TRB, National Research Council, Washington, DC, USA, 1994, pp. 101-113.

Lee, Y.H.; Lee, Y.M. Corner stress analysis of jointed concrete pavements. Transportation Research Record 1525, TRB, National Research Council, Washington, DC, USA, 1996, pp. 44-56.

Lee, Y.H.; Lee, Y.M.; Yen, S.T. Corner loading and curling stress analysis for concrete pavements - an alternative approach. Canadian Journal of Civil Engineering, v 29, n 4, National Research Council of Canada, 2002, pp. 576-588.

MacLeod, D.R.; Monismith, C.L. Comparison of solutions for stresses in plain jointed Portland cement concrete pavements. Transportation Research Record 888, TRB, National Research Council, Washington, DC, USA, 1982, pp. 22-31.

McCullough, B.F; Boedecker, K.J. Use of linear-elastic layered theory for the design of CRCP overlays. Highway Research Record 291, National Research Council, Washington, DC, USA, 1969, pp. 1-13.

Memari, A.M.; West, H.H. Computation of bridge design forces from influence surfaces. Computers and Structures, v. 38, n. 5-6, 1991, pp. 547-556.

Michigan Center for Truck Safety. Truck driver's guidebook, 6th edition. Michigan Center for Truck Safety, Lansing, MI, USA, 2001.

Mirambell, E. Temperature and stress distributions in plain concrete pavements under thermal and mechanical loads. 2nd International Workshop on the Theoretical Design of Concrete Pavements, Siquenza, Spain, 1990.

Nádai, A. Elastische platten. Verlag Springer, Berlin, 1925.

National Cooperative Highway Research Program (NCHRP). Guide for mechanistic-empirical design of new and rehabilitated pavement structures. Final Report, Part 3, Chapter 4, National Cooperative Highway Research Program, TRB, National Research Council, Washington, DC, USA, 2004.

Nayak, G.C.; Khanna, S.K.; Agrawal, S.M. Generalisation of influence surface technique for computations of stresses in pavements for wheel loads, thermal, and shrinkage

effects. Proceedings of the 2nd International Conference on Finite Element Methods in Engineering, University of Adelaide, 1976, pp. 1-14.

Oh, B.H. Cumulative damage theory of concrete under variable-amplitude fatigue loadings. ACI Materials Journal, v 88, n 1, American Concrete Institute, Detroit, MI, USA, 1991, pp. 41-48.

Oh, B.H. Fatigue analysis of plain concrete in flexure. Journal of Structural Engineering, v 112, n 2, American Society of Civil Engineers, New York, NY, USA, 1986, pp. 273-288.

Oran, C.; Lin, S.C. Influence surfaces for mulitbeam bridges. ASCE Journal of the Structural Division, v. 99, n. 7, 1973, pp. 1349-70.

Ozbeki, M.A.; Kilareski, W.P.; Anderson, D.A. Evaluation methodology for jointed concrete pavements. Transportation Research Record, n. 1043, 1985, pp. 1-8.

Poblete, M; Salsilli, R; Valenzuela, R; Bull, A; and Spratz, P. Field evaluation of thermal deformations in undoweled PCC pavement slabs. Transportation Research Record 1207, TRB, National Research Council, Washington, DC, USA, 1988, pp. 217-228.

Rao, C; Barenberg, E.J; Snyder, M.B; Schmidt, S. Effects of temperature and moisture on the response of jointed concrete pavements. 7th International Conference on Concrete Pavements, Orlando, FL, USA, 2001.

Rassias, G.M. The mathematical heritage of C.F. Gauss: a collection of papers in memory of C.F. Gauss. World Scientific, River Edge, NJ, USA, 1991.

Reddy, J.N. An introduction to the finite element method. McGraw-Hill, New York, NY, USA, 1993.

Richardson, J.M; Armaghani, J.M. Stress caused by temperature gradient in Portland cement concrete pavements. Transportation Research Record 1121, TRB, National Research Council, Washington, DC, USA, 1987, pp. 7-13.

Sawan, J.S.; Darter, M.I. Design of slab thickness and joint spacing for jointed plain concrete pavement. Transportation Research Record 930, TRB, National Research Council, Washington, DC, USA, 1983, pp. 60-68.

Sawan, J.S.; Darter, M.I. Structural design of PCC shoulders. Transportation Research Record 725, TRB, National Research Council, Washington, DC, USA, 1979, pp. 80-88.

Shoukry, S.N. Backcalculation of thermally deformed concrete pavements. Transportation Research Record 1716, TRB, National Research Council, Washington, DC, USA, 2000, pp. 64-72.

Tabatabaie, A.M.; Barenberg, E.J. Finite-element analysis of jointed or cracked concrete pavements. Transportation Research Record 671, TRB, National Research Council, Washington, DC, USA, 1978, pp. 11-19.

Tabatabaie, A.M.; Barenberg, E.J., Structural analysis of concrete pavements systems. Journal of Transportation Engineering, v 106, n 5, American Society of Civil Engineers, New York, NY, USA, 1980, pp. 493-506.

Tayabji, S.D.; Colley, B.E. Improved rigid pavement joints. Transportation Research Record 930, TRB, National Research Council, Washington, DC, USA, 1983, pp. 69-78.

Ullidtz, P. Pavement analysis. Elsevier, New York, NY, USA, 1987.

Vongchusiri, K.; Buch, N.; Gilliland, D. Mechanistic analysis of multifactors affecting reponses of concrete slabs through interpolation schemes. International Journal of Pavements, v. 3, n. 2, 2004, pp. 1-13.

Westergaard, H.M. Analysis of stresses in concrete pavement due to variations of temperature. Proceedings, Highway Research Board, v. 6, 1926, pp. 201-215.

Westergaard, H.M. Stresses in concrete pavements computed by theoretical analysis. Public Roads, v. 7, n. 2, 1926, pp. 25-35.

Westergaard, H.M. Computation of stresses in bridge slabs due to wheel loads. Public Roads, v. 11, n. 1, 1930, pp. 1-23.

Williams, R.D.; du Preez, R.J. Improved method for generating influence surfaces for bridge decks. Civil Engineer in South Africa, v. 22, n. 11, 1980, pp. 337-342.

Yu, H.T; Khazanovich, L. Effects of construction curling on concrete pavement behavior. 7th International Conference on Concrete Pavements, Orlando, FL, USA, 2001.

Yu, H.T; Khazanovich, L; Darter, M.I; Ardani, A. Analysis of concrete pavement responses to temperature and wheel loads measured from instrumented slabs. Transportation Research Record 1639, TRB, National Research Council, Washington, DC, USA, 1998, pp. 94-101.

Zaghloul, S.M.; White, T.D.; Kuczek, T. Evaluation of heavy load damage effect on concrete pavements using three-dimensional, nonlinear dynamic analysis. Transportation Research Record 1449, TRB, National Research Council, Washington, DC, USA, 1994, pp. 123-133.

Zaman, M.; Alvappillai, A., Contact-element model for dynamic analysis of jointed concrete pavements. Journal of Transportation Engineering, v 121, n 5, American Society of Civil Engineers, New York, NY, USA, 1995, pp. 425-433.

Zhang, B.; Phillips, D.V.; Wu, K. Further research on fatigue properties of plain concrete. Magazine of Concrete Research, v 49, n 180, Cement and Concrete Association, London, England, UK., 1997, pp. 241-252.

Zienkiewicz, O.C.; Cheung, Y.K. The finite element method in structural and continuum mechanics. McGraw-Hill, New York, NY, USA, 1967.